IN-05
[illegible]

Understanding the Potential of Aeroelastic Couplings to Stabilize Ground and Air Resonance in a Soft-Inplane Tiltrotor

Final Report for GSRP Program

Anna K. T. Howard

Friday, June 4, 1999

The Pennsylvania State University
Department of Aerospace Engineering
Rotorcraft Center of Excellence

Dr. Ed Smith, Faculty Advisor, Associate Professor in Aerospace Engineering
Dr. Mark Nixon, NASA GSRP Advisor, Research Engineer, U.S. Army Research Laboratories

1 Introduction

1.1 The Thesis Question

Can air and ground resonance stability be improved by judicious use of composite couplings in the wing and kinematic couplings in the blades of a soft-inplane hingeless tiltrotor?

1.2 Background and Motivation

The tiltrotor offers the best mix of hovering and cruise flight of any of the current V/STOL configurations. One possible improvement on the tiltrotors of today designs would be using a soft-inplane hingeless hub. The advantages to a soft-inplane hingeless hub range from reduced weight and maintenance to reduced vibration and loads. However, soft-inplane rotor systems are inherently in danger of the aeromechanical instabilities of ground and air resonance. Furthermore tiltrotors can be subject to whirl flutter. At least in part because of the potential for air and ground resonance in a soft-inplane rotor, the Bell XV-15, the Bell-Boeing V-22 Osprey, and the new Bell Augusta 609 have stiff-inplane, gimballed rotors which do not experience these instabilities. In order to design soft-inplane V/STOL aircraft that do not experience ground or air resonance, it is important to be able to predict these instabilities accurately. Much of the research studying the stability of tiltrotors has been focused on the understanding and prediction of whirl flutter. As this instability is increasingly well understood, air and ground resonance for a tiltrotor need to be investigated.

Once we understand the problems of air and ground resonance in a tiltrotor, we must look for solutions to these instabilities. Other researchers have found composite or kinematic couplings in the blades of a helicopter helpful for ground and air resonance stability. Tiltrotor research has shown composite couplings in the wing to be helpful for whirl flutter. Therefore, this project will undertake to model ground and air resonance of a soft-inplane hingeless tiltrotor to understand the mechanisms involved and to evaluate whether aeroelastic couplings in the wing or kinematic couplings in the blades would aid in stabilizing these instabilities in a tiltrotor.

A brief history of tiltrotors and the literature related to this project is given in the next section. The remaining sections provide detail about the current analysis. The modeling techniques used to model the blades, hub, rigid pylon, and elastic wing are described in detail. The validation study used to give confidence to the model is shown with comparisons to a soft-inplane rotor and to a gimballed rotor. Some results from the parametric studies to look at the couplings in the blades are given followed by a discussion of the future research needed and the time line for completing that research.

2 Literature Review

2.1 Tiltrotor History

One of the biggest hurdles facing a tiltrotor designer today results from the relatively few number of tiltrotors that have been built: the knowledge that comes from experience is very limited. It behooves us to spend a little time remembering what has been done before embarking anew.

The first tiltrotor built and flown was the Transcendental Model 1-G as shown in Fig. 1 [16] . The Model 1-G was developed without governmental support of any kind, a rarity today, and was the first demonstration of the capabilities of a tiltrotor configuration. The Model 1-G achieved first free flight on July 6, 1954 at Bellanca Field, New Castle, Delaware, and first conversion to airplane mode in December, 1954. The Model 1-G used three-bladed, fully-articulated rotors (i.e., rotors with flap and lag hinges and pitch bearings–see Fig. 2). After 23 hours of air time over more than 100 flights, the Model 1-G crashed on July 20, 1955 and was not rebuilt [28] . In 1956 the Air Force awarded Transcendental a contract to build another tiltrotor. The result was the Transcendental Model 2-G, basically the same design as the Model 1-G but with more powerful engines. The Model 2-G was never flown [35] .

Bell Helicopters then developed the Bell XV-3, one of two designs chosen from a Air Force / Army "convertiplane" competition in 1951 where 17 companies submitted 19 designs [28] [35] . The XV-3 also had three blades and a fully-articulated hub. First flight for the XV-3, the second tiltrotor to fly successfully, was in 1955. The first XV-3 built crashed, and a second XV-3 was built but this time with two-bladed teetering rotors (i.e., rotors with two blades rigidly attached to one another with the shaft as a pivot point for flapping–see Fig. 3). The XV-3 led researchers to discover and solve many technical challenges of the tiltrotor configuration [16] . In 1968, Bell began to develop the Model 300, now three-bladed but with gimballed rotors (i.e., rotors with three blades rigidly attached to a hub which is free to pivot about the shaft on a universal joint). Dynamic rotor/pylon instability tests were conducted, but the vehicle was never built. The stability margins which had been a problem with the articulated rotors did not seem to be a problem with this gimballed design: the Model 300 was stable well beyond its design dive speed [35] .

NASA and the U.S. Army initiated a proof-of-concept program in April, 1973. The contract was awarded to Bell Helicopter to construct what began life as the Model 301 but became the XV-15 Tiltrotor Research Aircraft shown in Fig. 4. The XV-15 has the best safety record of any tiltrotor built to date. The 6.5 ton aircraft flew up to 346 mph at 16,000 ft. in June, 1980. It has been called the "most successful high speed V/STOL ever built" [16] .

In December 1981, with the XV-15 tests progressing apace, the Deputy Secretary of Defense initiated a development program for a single aircraft which would serve the U.S. Marine Corps, the U.S. Air Force, and the U.S. Army. Budgets were shrinking so a single aircraft, or at least several versions of a single aircraft, had the potential to save the Defense Department significant sums of money. The requirements were stringent: for example, the craft must hover at high altitudes at high temperatures with 8300 lb. payload. It must also be able to self-deploy anywhere in the world without in-flight refueling [27] . Conventional helicopters, compound helicopters, tiltrotors, and lift fan concepts were considered to meet these goals, but the tiltrotor was chosen as the best configuration to meet the various requirements. A contract was awarded to the team of Bell Helicopter Textron and Boeing Helicopters in 1982 with a view to develop and produce the V-22 Osprey (Fig. 5), originally the JVX, eventually to deliver almost 1000 tiltrotors for four branches of the armed forces [27] . The first flight occurred on March 19, 1989. Development of the V-22 is continuing at this time: the second wave of test vehicles has flown approximately 1400 hours to date.

Several other tiltrotors have reached the design or testing stage, including the Bell 266, the Grumman Helicat, and the Boeing 222. Each offered valuable information about the tiltrotor configuration, but none of these aircraft ever flew [22] , [26] .

2.2 Advantages of Tiltrotors

The primary advantage of tiltrotors over helicopters is speed. Because the wing offloads the rotor in forward flight, the rotor can be used to provide forward speed without also providing lift. It is estimated that a tiltrotor can reach a rescue site on average 2-3 times faster than present rescue aircraft [35] . Also, the limitation of edgewise flight which a helicopter faces is avoided by tilting the rotor, in effect placing the rotor into a situation akin to climb in a helicopter [35] . But if the only desire is speed, fixed wing aircraft are much superior. The advantage of tiltrotors over fixed wing is obvious: they can hover, albeit not as efficiently as helicopters. The advantage of tiltrotors over a Harrier or other jet V/STOL is lower disk loadings, or the ratio of thrust to disk area (Fig. 6). This lower disk loading makes the tiltrotor much more efficient in hover (since induced power loss is proportional to thrust multiplied by downwash velocity) and affords a lower downwash velocity and lower tip-speed than other alternatives. As the tip-speed is lowered, the noise level is decreased. As the downwash velocity is lowered, the tiltrotor is less bothersome to people on the ground. The tiltrotor is an ideal choice when both speed and hovering capabilities are important, though clearly it will never replace the helicopter for a truly efficient hovering machine or the fixed wing for long fast flights from prepared runways.

There are other possibilities for the mix between speed and hovering ability, many of which can be considered compound helicopters. But a study performed by the Group for Aeronautical Research and Technology in Europe (GARTEUR) undertaken in the late 1980's compared several compound helicopters with a tiltrotor and concluded that the tiltrotor was more economically feasible for a large range of operations than the compound helicopter [11] .

2.3 Soft-/Stiff-Inplane Hingeless Tiltrotors

Tiltrotors with stiff-inplane, gimballed rotors have shown their potential in the XV-15 which is still flying, the V-22 which is almost through with flight testing, and the Bell Augusta 609 which is available for ordering. Clearly this rotor system is effective. Why then do we want to reconsider the design?

The tiltrotor offers intriguing possibilities for civil transport. For example, the "Civil Tiltrotor Missions and Applications" research study concluded that tiltrotors could capture a major share of the travel in the northeast corridor provided vertiports were available [48] . NASA's Civil Tiltrotor Initiative is dedicated to helping this become a reality if possible. To be economically viable, a civil tiltrotor needs to be as inexpensive and efficient as possible. One possible improvement would be to use a soft-inplane hingeless hub. Soft-inplane rotor systems have an inplane natural frequency lower than the rotor speed. This is the norm for articulated rotors where a typical lag frequency is around .2 or .3/rev. But as hingeless rotors are increasingly chosen for new designs, the V/STOL designer has a choice: the lag frequency shouldn't be too close to 1/rev because of excessive blade loads but it can be either above or below 1/rev. Helicopters have found advantages in using soft-inplane hingeless rotor systems such as reduced vibration and loads and potentially improved handling qualities. There are fewer parts in a hingeless hub resulting in potentially less weight and improved reliability. The Comanche is a prime example of these advantages [38] .

But it remains true that the most successful tiltrotors, the XV-15, the V-22, and the new 609, all have stiff-inplane, gimballed rotors. This is at least in part because a soft-inplane rotor is inherently in danger of the instabilities of ground and air resonance (see [18]). Ground resonance is a catastrophic instability which can destroy aircraft and anything inside them. Air resonance is a less catastrophic instability which causes large vibrations and severely degraded handling qualities. The challenge of building an aircraft which satisfies all the mission requirements and doesn't suffer from air and ground resonance is more complicated for tiltrotors than it is for helicopters since tiltrotors also suffer from whirl flutter [20] .

In order to design soft-inplane V/STOL aircraft that do not experience ground or air resonance, it is important to be able to predict these instabilities accurately. Analytical computer modeling to predict air and ground resonance in soft-inplane helicopters has been available for some time. Much of the research studying the stability of tiltrotors has aimed to understand and predict whirl flutter. As this instability is increasingly well understood, air and ground resonance for a tiltrotor need to be investigated.

Once these instabilities in a tiltrotor are well understood, the question becomes what can be done to ensure stability. Many studies have found composite or kinematic couplings in the blades of a helicopter helpful for ground and air resonance. Tiltrotor research has shown composite couplings in the wing to be helpful for whirl flutter. Therefore, this project will undertake to model ground and air resonance of a soft-inplane hingeless tiltrotor to better understand the mechanisms involved and to evaluate whether aeroelastic couplings in the wing or kinematic couplings in the blades would aid in stabilizing these instabilities in a tiltrotor.

2.4 Instabilities

One of the great challenges in aircraft design is to be very sure that there are no instabilities encountered within the operating regime of the aircraft. The tiltrotor has several possible instabilities which must be avoided. Whirl flutter is a concern for all tiltrotors while air and ground resonance concern only soft-in-plane tiltrotors.

2.4.1 Air and Ground Resonance in a Helicopter

Ground resonance was first observed in the autogiros in the 1930's and early 1940's. This instability was not well understood at that time and was therefore difficult to avoid by design. The American Helicopter Society listed the characterization of air and ground resonance as one of the top twenty advances in vertical flight history [7] . Ground resonance occurs when the low frequency lag mode of the rotor (in the non-rotating frame) coalesces with a fuselage or body frequency. The cyclic lag modes ζ_{1c} and ζ_{1s} produce a wobble of the rotor center of gravity. This shifting fore and aft and laterally of the effective mass of the rotor can couple with the vibration of the fuselage to produce huge displacements. On a helicopter sitting on the ground, the body frequencies are governed primarily by the stiffness of the landing gear–aerodynamic forces play very little role. Ground resonance can destroy an aircraft in seconds (as shown by the Kellet XR-2 shown in Fig. 7).

Air resonance is a similar aeromechanical instability mathematically but occurs in the air, often in a hingeless rotor [18] . Unlike for ground resonance, aerodynamic forces play an important role in air resonance. Air resonance is rarely catastrophic, but since this instability causes very large vibrations (which leads to issues of passenger comfort and material fatigue life) and much poorer handing qualities, regions of instability should be avoided if possible [37] .

The instability of ground resonance was first explained mathematically by Coleman and Wagner independently in 1943 [9] . These early analyses neglected aerodynamics, certainly a good first approximation for ground resonance. Both Coleman and Wagner developed a simple four-degree-of-freedom model which included high and low frequency lag modes (in the non-rotating frame) for the blade and body pitch and roll. The graph shown in Fig. 8 shows the rotor rotation speed on the horizontal axis and the frequencies of the various degrees of freedom on the vertical axis. As the low frequency lag mode coalesces with the body mode an instability occurs. This form of graph has come to be called a Coleman diagram [9] .

The damping associated with this simple model is quite distinctive as shown in Fig. 9. This plot shows the damping ratios from a four-degree-of-freedom system, blade cyclic lag plus body lateral and longitudinal motion. With no aerodynamics present, the damping of all four degrees of freedom is zero except in the regions of instability. In these regions the low frequency lag mode has coalesced with one of the body frequencies: one mode becomes unstable and the other mode becomes even more stable. In a helicopter it is the low frequency lag mode which goes unstable. As aerodynamic forces are added, the damping is no longer zero outside of the unstable regions. When this is the case one of the modes will be more damped than the other. It is typically the less damped mode that becomes unstable. Again, in a helicopter this usually means that the low frequency lag mode becomes unstable while the fuselage mode becomes even more stable since the rotor body modes are usually more damped than the rotor lag modes. Preliminary results with this tiltrotor analysis show that it is typically the wing modes that go unstable.

Coleman's formulation gives rise to a very simple stability criterion shown below: a helicopter would be stable if

$$C_\zeta^* C_y^* > \frac{(1-\nu_\zeta)}{4\nu_\zeta}\left(\frac{\omega_y}{\Omega}\right)^2 \frac{S_\zeta^{*2}}{M_y^*}$$

where is $\frac{S_\zeta^*}{M_y^*}$ is half the ratio of the rotor mass to the support mass, $\frac{\omega_y}{\Omega}$ is the non-dimensional body lateral mode, C_ζ^* is the damping in the lag mode, C_y^* is the damping in the body lateral mode, and ν_ζ is the rotor lag frequency (assuming that the frequency for the body mode is not the same for both lateral and longitudinal motion) [8] . This simple criterion shows that it is necessary to have damping in both the body mode and in the lag mode. Thus landing gear dampers and rotor lag dampers exist on almost all helicopters flying today. The presence of the ratio of the rotor mass to the support mass is instructive: if the rotor mass is large with respect to the body mass, more damping is needed to stabilize the vehicle. Also, this simple stability criterion makes it clear that a stiff-inplane rotor will not suffer ground resonance since $(1 - \nu_\zeta)$ is negative [18] .

Coleman's basic theory was not enough to eliminate the problems with other helicopters, including the Sikorsky XR-4, R-5, and R-6 [7] . Clearly a more exact analysis of this phenomena is desired since avoiding ground resonance is a prime design requirement. Advances in ground resonance prediction have come along steadily since the 1970's with a plethora of studies. In 1970 Lytwyn, Miao, and Woitsch expanded the basic analysis to hingeless rotors where air resonance is more of a problem [25] . Dynamic inflow was shown to be important in the early 1980's starting with Johnson in 1982 and Friedmann and Venkatesan in 1986 [19] , [12] . The importance of an accurate trim model to air resonance stability was shown by Nagabhushanam and Gaonkar and later by others [31] , [30] . Ground and air resonance stability is now incorporated into many comprehensive rotorcraft codes. Some additional contributions will be discussed in the next section.

Comprehensive codes to predict ground and air resonance in tiltrotors have been slower in coming. The lack of reliable methods of ensuring ground resonance for a tiltrotor has certainly contributed to the pervasive use of gimbal technology in the tiltrotors flying today. Going to a stiff-inplane gimballed hub for the XV-15 and the V-22 eliminated these problems.

2.4.2 Whirl Flutter in a Tiltrotor

In 1960, two Lockheed Electra aircraft crashed with loss of life in what is now called propeller/nacelle whirl flutter or simply whirl flutter [20] . Whirl flutter is a dynamic instability where the inplane forces couple with wing motions to become unstable. This possibility was first published by Taylor and Browne in 1938 and later investigated academically by Scanlan in the 1950's [47] , [43] . The cases of whirl flutter in the Electra, occurring as they did in a propeller-driven, fixed-wing aircraft, suggested the possibility that the tiltrotor configuration might also be subject to a similar instability [42] .

In a 1962 wind-tunnel test of the XV-3 in the NASA Ames full-scale tunnel, an instability driven by a coupling between the proprotor and the pylon was discovered [21] . This finding led many researchers to look into whirl flutter in tiltrotors. Kvaternik reviewed the state of the art of whirl flutter research in 1976 and again in 1991 and 1992 [22] , [23] , [24] .

Whereas a typical ground resonance plot is with a rotor speed sweep, a typical whirl flutter plot is versus forward speed as is shown in Fig. 10. The wing modes marked *c*, *b*, and *t* in the plots here (chordwise bending, beamwise bending, and torsion) all go unstable at high enough forward speeds. This instability is very violent and can destroy the aircraft.

2.4.3 Air and Ground Resonance in a Tiltrotor

Twenty-six years ago Boeing conducted two wind tunnel tests for the Model 222 which was designed as soft-inplane hingeless tiltrotor. The first test in 1973 used a 1/4.6 Froude-scaled Model 222 in the Boeing V/STOL wind tunnel. Steady state rotor and aircraft loads, performance data, and stability derivatives from mid-transition to cruise were obtained [29] . The second test was a full-size, semi-span model test in the NASA Ames 40' by 80' wind tunnel. This test identified regions with degraded stability and investigated some active feedback systems to add damping to the lightly damped wing modes. All the tests done in the wind tunnel were in cruise mode; no ground resonance data was gathered [26] . This test was compared to the 1971 Bell Helicopter test of a 25-foot gimballed rotor in the same NASA 40' by 80' wind tunnel [17] . Both of these tests used the same NASA wing and pylon making it easier to compare them.

2.5 Possible Solutions

During the years from 1970 to 1998, advances in computing power developed to allow more exact characterizations of the instabilities of ground resonance, air resonance, and whirl flutter. The obvious mechanisms of ensuring the stability of the V/STOL vehicle were to use either stiff-inplane rotor systems or lag and landing gear dampers. These solutions neglected the advantages of a soft-inplane hub and added weight and complexity. The search was then for other ways to stabilize these instabilities.

One possible solution to the stability problems of air resonance, ground resonance, and whirl flutter, is the use of aeroelastic couplings. Composite tailoring techniques can now introduce couplings into wings or blades. For example, consider a composite beam with two layers, one with fibers running at 45 degrees and one with fibers running down the length of the beam. This kind of unbalanced laminate structure will exhibit bending-torsion coupling. Pushing up on the end of the beam will twist the beam. This is the sort of construction that could be used in the spar of a tiltrotor wing or blade (Fig. 11) or in the flexbeam of a rotor blade (Fig. 12).

Kinematic couplings in the blades could be created in several ways other than with composite tailoring. Skewed hinges in an articulated blade can create pitch-lag or pitch-flap couplings (Fig. 13). The order of the hinges when they aren't coincident create couplings from the steady coning or lag angles. Feedback systems can couple pitch and blade motion. Also, a pitch-link outboard of a flexure as in this example causes pitch-flap couplings (Fig. 14).

2.5.1 Blade Couplings For Helicopter Air and Ground Resonance

Using kinematic couplings in the blades to stabilize air and ground resonance for a helicopter is not an uncommon concept in the literature. Burkam and Miao started this research in 1972 [6] . In 1977 Ormiston published a landmark paper investigating many different contributing factors. He discovered that combinations of pitch-flap and pitch-lag couplings with structural flap-lag coupling were most helpful for stabilizing air and ground resonance. Ormiston also showed that ground resonance was very different from air resonance and that the factors which improved air resonance stability margins (for example pitch-lag coupling, $\delta_4 < 0$, where the blade pitches nose-down as it lags back) destabilized ground resonance [36] .

Bousman worked with these couplings experimentally in 1981; this research showed that pitch-lag coupling ($\delta_4 < 0$) improved stability away from the critical regions of air resonance instability but was less helpful immediately around the instability [5] . In 1993 Smith and Chopra investigated composite tailoring of the blades to postpone or eliminate ground and air resonance instabilities for a helicopter [45] . Composite tailored blades with pitch-lag coupling improved air resonance stability and pitch-flap couplings reduced the air resonance stability margins though this effect was less powerful than the pitch-lag couplings. Gandhi and Hathaway published an optimization study that showed that pitch-lag with $\delta_4 < 0$, pitch-flap coupling where the blade pitches nose-down as it flaps up ($\delta_3 > 0$), and a lag-pitch-flap hinge sequence formed a good combination to stabilize ground resonance [14] .

2.5.2 Blade Couplings For Tiltrotor Whirl Flutter

Gaffey published a study in 1969 which considered pitch-flap coupling for whirl flutter in a tiltrotor. Gaffey found that pitch-flap coupling with $\delta_3 < 0$ had a stabilizing trend on whirl flutter and that $\delta_3 > 0$ destabilized whirl flutter [13] . More than twenty years later, Nixon showed that elastic extension-twist coupling of the rotor blade can improve tiltrotor aerodynamic performance but that this coupling degrades the stability for whirl flutter [35] . Nixon's research also investigated composite couplings in the blades to stabilize whirl flutter. This study found that elastic bending-twist coupling in the blades has potential to increase whirl flutter stability and that the amount of coupling required is feasible for performance and blade loads. Fig. 15 shows an increase in whirl flutter stability based on flatwise bending-twist couplings in the blade taken from Ref. [35] . Here $\lambda = \frac{K_{34}}{EI_f+GJ}$ is a measure of the off-diagonal coupling between the flatwise-bending and twist of the blade. λ is sensitive to the forward velocity unlike kinematic pitch-lag coupling because as V increases the blade has more collective pitch so that more of the flatwise bending in the lag direction. As V increases from 100 to 400 knots, a λ value of .1

increases from a δ_4 value of 0.4 to 0.7.

2.5.3 Composite Tailoring of the Wing for Whirl Flutter

In 1995 a group of researchers from Bell published an analysis showing that tailoring the wing with composites could allow the V-22 to use an 18% thickness-to-chord ratio wing instead of a 23% ratio without degrading the whirl flutter stability margin [39] . Using comparable thicknesses, a 24 knot increase in flutter speed was predicted. In 1997 a wind tunnel test at NASA Langley showed a 30 knot delay in whirl flutter onset (Fig. 16) [10] . The 18% thick wing used wing beamwise bending/torsion coupling in the skin to decrease the natural coupling between bending and torsion due to the offset of the pylon and rotor masses from the pylon attachment point. This improved the stability of the wing bending mode but degraded the stability of the wing chord mode. Tailoring the wing spar caps alleviated the loss of stability for the wing chord mode.

Barkai and Rand showed that chordwise bending-twist in the wing was beneficial for whirl flutter stability in gimballed, stiff-inplane tiltrotors [1] . Fig. 17 shows the increase in whirl flutter stability she calculated using wing chordwise-bending-twist coupling. In this figure $\frac{C_{16}}{\bar{C}_{16}} = \frac{2N_\theta - N}{N}$ where N_θ is the number of plies oriented at an angle θ and N is the total number of plies; C_{16} is the off-diagonal coupling modulus for bending-twist coupling in the composite layup [41] . Though this study and the Bell study discussed above were for gimballed, stiff-inplane tiltrotors, their importance lies in a stability increase for a tiltrotor using aeroelastic couplings in the wing.

2.6 Modeling

Aerospace engineering has come a long way from the days when the an aircraft could be built and flown in a year. Stringent requirements are placed on new aircraft today for performance, efficiency, and safety. Nor are funds so free-flowing that we can afford to tread far down the road for one design only to find it untenable. Comprehensive modeling codes are used to test as much as possible for each potential design as inexpensively as possible. Accurate modeling of the tiltrotor is essential to predicting its stability. Since the XV-3, the XV-15, and the V-22 are all stiff-inplane gimballed rotors, the vast majority of studies conducted for tiltrotor stability have focused on whirl flutter analysis.

Aeroelastic analysis began in the 1960's and expanded significantly in the 1970's. In 1974 Johnson compared the Bell and Boeing rotors discussed above using an analysis that included hover, conversion, and forward flight and later expanded this model to a comprehensive aeroelastic model which became CAMRAD [17] . In 1984 and 1985 Kvaternik developed the Proprotor Aeroelastic Stability Analysis (PASTA) code at NASA Langley [24] . By the third version of PASTA eleven degrees of freedom were modeled including rigid flapping and lead-lag motion of the blade, gimbal motion, and a rigid control system. This code as many others of that era included only cruise mode. Also, a comprehensive aeroelastic analysis called DYN4 (for rigid blades or DYN5 for elastic blades) has been developed by Bell Helicopters [46] .

In 1993 the University of Maryland Advanced Rotorcraft Code (UMARC) was expanded to allow whirl flutter research. This analysis, which included hover, transition, and forward flight modes, consisted of a gimballed hub with blades and wing modeled using the finite element method [35] , [3] .

Srinivas expanded the UMARC code in 1995 to include the entire tiltrotor including the whole wing span and both rotors using the finite element method (Fig. 18) [46] .One of Srinivas' conclusions was that for whirl flutter the symmetric modes modeled using a wind tunnel, semi-span model were the modes that became unstable first and hence set the flutter speed. This indicates that a good first step in modeling a tiltrotor would be to use a semi-span model.

In 1995, a group of researchers from the Technion Institute in Israel presented a new analysis based upon a numerical technique to preserve the symbolic exactness of the equations of motion. This method retained the partial derivatives for the stability analysis and allowed them to discuss some of the causes for whirl flutter in tiltrotors [40] , [41] .

2.7 Conclusions

Understanding of the tiltrotor configuration has grown significantly but more remains to be done. One of the venues where additional research is needed is soft-inplane hingeless tiltrotors. An analysis tool is needed to accurately predict the instabilities of ground and air resonance. Once this analysis is in place, numerous studies need to be conducted to examine the effects of various parameters on these instabilities. One possible source for a solution comes from aeroelastic couplings: composite couplings in the wing and kinematic couplings in the blades. There is a clear place for this research to add to the body of knowledge.

3 Tiltrotor Modeling

3.1 Approach Overview

A semi-span tiltrotor is modeled using the right wing, pylon, and rotor assembly. The root of the wing is assumed to be fixed in space as for a wind tunnel model. The wing is modeled as an elastic finite element beam. Three displacements in the x, y, and z directions are modeled between the pylon center of gravity and the hub and three additional displacements are allowed between the pylon center of gravity and the wing attachment point. The pylon is rigid and attached to the wing with a downstop spring. The blades are assumed to be rigid with flap and lag degrees of freedom. Any desired twist can be used. The model is pictured in Fig. 1. Response calculations are performed to obtain the steady coning and inflow as well as one of c_T and θ_{75} the other of which is assumed to be known. An eigenvalue analysis provides stability information.

The model itself is formulated using Hamilton's principle to derive the equations of the motion for the entire model.

$$\delta\Pi = \int_{t_1}^{t_2} (\delta U - \delta T - \delta W)\, dt = 0 \tag{1}$$

Since energies are additive, the wing, pylon, and blades can be treated separately. The kinetic, strain, and work energies of the blades with arbitrary hub motion are derived initially. The motion of elastic blades with hub motion is modeled following the method described in the UMARC manual [3] . The hub can be gimballed, hingeless, or articulated. A rigid blade simplification is made: the kinetic energy and work energy terms can then be integrated out the length of the blade. A simple strain energy formulation is used including springs for the flap and lag degrees of freedom as well as the gimbal. The wing is modeled using the finite element method as a simple beam with five degrees of freedom at each node—extension in the wing is constrained to zero. The rigid pylon serves to connect the hub motion with the wing-tip motion. The contributions to the kinetic, strain, and work energies from the blades are then added to the contributions from the pylon and wing. Hamilton's principle is applied to produce global equations of motion.

3.2 Blade and Hub

The blade is modeled originally as an elastic beam. Any displacement and rotation is allowed, each a function of position on the blade. The degrees of freedom used are given in the vector

$$\lfloor \; u_e \quad v \quad w \quad \phi \quad x_F \quad y_F \quad z_F \quad \phi_s \quad \alpha_s \quad \psi_s \; \rfloor \tag{2}$$

where x_F, y_F, and z_F are hub displacements, ϕ_s, α_s, and ψ_s are hub rotations, and u_e, v, and w are displacements in the cross-sectional frame as shown in Fig. 2. Hamilton's principle is used to derive the equations of motion for the blade with six degrees of freedom for the hub motion.

Note that throughout the derivation whenever allowable, an ordering scheme was applied. The orders of the various variables as given in Appendix 8.3 were adapted from the work of Smith and Nixon [44] , [35] . The resulting equations of motion for the blade with hub motion were of order ε; that is, the largest terms in each of the equations were of order ε. It was decided to retain all terms of orders ε, $\varepsilon^{\frac{3}{2}}$, ε^2, and $\varepsilon^{\frac{5}{2}}$ and only linear terms of order ε^3. This convention is applied throughout the derivation of the blade and hub matrices.

3.2.1 Kinetic Energy

The variation of kinetic energy is given by

$$\delta T = \int_0^R \iint_A \rho \vec{V} \cdot \delta \vec{V} d\eta d\zeta \, dx \tag{3}$$

To find the velocity $\vec{V}$, the position vector is determined and differentiated with respect to time. This position vector is expressed as the displacement from a fixed point in space to any point on the undeformed elastic axis as expressed in the inertial coordinate system. This vector $\vec{r}$ is given by the following equation.

$$\vec{r} = \left\{ \begin{array}{c} x_F \\ y_F \\ z_F \end{array} \right\} + [T_{wi}]^T [T_{hw}]^T [T_{rh}]^T [T_{ur}]^T \left\{ \begin{array}{c} x \\ 0 \\ 0 \end{array} \right\}$$
$$+ [T_{wi}]^T [T_{hw}]^T [T_{rh}]^T [T_{ur}]^T [T_{cu}]^T \left(\left\{ \begin{array}{c} u \\ v\cos\theta_0 + w\sin\theta_0 \\ -v\sin\theta_0 + w\cos\theta_0 \end{array} \right\} + [T_{dc}]^T \left\{ \begin{array}{c} 0 \\ \eta \\ \zeta \end{array} \right\} \right) \quad (4)$$

The transformation matrices used in this formula are given explicitly in Appendix 8.4. In general $[T_{wi}]$ accounts for the rotation of the hub given by ϕ_s, α_s, and ψ_s. $[T_{hw}]$ accounts for the pylon rotation α_p. $[T_{rh}]$ accounts for the azimuthal rotation ψ. $[T_{ur}]$ accounts for precone and gimbal angle as discussed below. $[T_{cu}]$ accounts for the collective pitch setting and $[T_{dc}]$ expresses the displacement due to the elastic bending of the blade. η and ζ are cross-sectional coordinates and x is the distance along the blade. Foreshortening effects are included so that the degree of freedom u is the expressed as the difference between the elastic axial deflection u_e and the kinematic axial deflection u_F.

$$u = u_e - u_F = u_e - \int_0^x \left(v'\delta v' + w'\delta w'\right) dx \quad (5)$$

Because this position vector is expressed in the inertial frame, the velocity $\vec{V}$ can be calculated without recourse to differentiating unit vectors for the frame of reference.

The variation of velocity is then calculated. Since the velocity includes time derivatives of the degrees of freedom, the variation of velocity $\delta\vec{V}$ includes terms such as $\delta\dot{v}_c$. Integration by parts is used to eliminate such terms.

$$\int_{t_1}^{t_2} \int_0^1 \iint_A \rho \left(T_{v_c}\, \delta v_c + T_{\dot{v}_c}\, \delta\dot{v}_c\right) dA\, dx\, dt = \int_{t_1}^{t_2} \int_0^1 \iint_A \rho \left(T_{v_c} - \frac{\partial}{\partial t} T_{\dot{v}_c}\right) \delta v_c\, dA\, dx\, dt \quad (6)$$

This integration by parts allows the kinetic energy to be expressed as

$$\int_{t_1}^{t_2} \delta T\, dt = \int_{t_1}^{t_2} \int_0^1 m \left(T_F + \sum T_{q_i} \delta q_i\right) dx\, dt \quad (7)$$

where q_i ranges over all the degrees of freedom and their derivatives with respect to blade position x and T_F are the foreshortening terms.

3.2.2 Aerodynamics

The virtual work δW needed for Hamilton's principle comes from the aerodynamic forcing on the blades assumed here to be quasi-steady. Uniform inflow is also assumed. The aerodynamic forces at an arbitrary blade station can be expressed as lift, drag, and pitching moment.

$$\begin{aligned} L &= \frac{1}{2}\rho V^2 c C_l \\ D &= \frac{1}{2}\rho V^2 c C_d \\ M &= \frac{1}{2}\rho V^2 c^2 C_m \end{aligned} \tag{8}$$

L_w, L_v, and L_u are the external loads acting along the deformed axis. M_ϕ is the moment about the deformed elastic axis. These loads are shown in Fig. 3. Assume forms for the aerodynamic coefficients as

$$\begin{aligned} C_l &= c_0 + a\alpha \\ C_d &= c_d + d_2\alpha^2 \\ C_m &= C_{mac} + f_1\alpha \end{aligned} \tag{9}$$

The first order polynomial term $d_1\,|\alpha|$ in the expression for the coefficient for drag is not included. An attached flow assumption is made along with a small angle approximation for α so that

$$\begin{aligned} \sin\alpha &= \alpha \\ \cos\alpha &= 1 \\ \bar{V} &= U_T \\ \sin\Lambda &= \frac{U_R}{U_T} \\ \alpha &= -\frac{U_P}{U_T} \end{aligned} \tag{10}$$

These substitutions along with non-dimensionalization give the following forms for the aerodynamic forces:

$$\begin{aligned}
L_u &= \frac{1}{6}\frac{\gamma I_b}{a}\left(-c_d U_T U_R\right) \qquad (11)\\
L_v &= \frac{1}{6}\gamma I_b U_P^2 + \frac{1}{6}\frac{\gamma I_b}{a}\left(-c_d U_T^2 - d_2 U_P^2 - c_0 U_T U_P\right)\\
L_w &= -\frac{1}{6}\gamma I_b U_T U_P + \frac{1}{6}\frac{\gamma I_b}{a}\left(c_0 U_T^2 - c_d U_T U_P\right)\\
M_\phi &= \frac{1}{6}\gamma I_b e_d U_T U_P + \frac{1}{6}\frac{\gamma I_b}{a}\left(c C_{mac} U_T^2 - e_d c_0 U_T^2 - c f_1 U_T U_P + e_d c_d U_T U_P\right)
\end{aligned}$$

The incident velocity comes from two major sources: the wind velocity and the blade velocity. The position on the blade with respect to the hub can be calculated as in the previous section. This position is differentiated with respect to time to give the blade velocities.

$$\left\{\begin{array}{c}\dot{x}_1\\ \dot{y}_1\\ \dot{z}_1\end{array}\right\} = \left\{\begin{array}{l}\dot{u} - \left(\dot{v}' + w'\dot{\phi}\right)\left(\eta\cos\theta_1 - \zeta\sin\theta_1\right)\\ \qquad - \left(\dot{w}' - v'\dot{\phi}\right)\left(\eta\sin\theta_1 + \zeta\cos\theta_1\right)\\ \dot{v} - \dot{\phi}\left(\eta\sin\theta_1 + \zeta\cos\theta_1\right)\\ \dot{w} + \dot{\phi}\left(\eta\cos\theta_1 - \zeta\sin\theta_1\right)\end{array}\right\} \qquad (12)$$

where θ_1 is the sum of the elastic twist and the pitch setting at this blade position, $\theta_1 = \theta_0 + \phi$. The velocity of the wind comes from two sources: inflow and forward velocity. The inflow term λ is vertical in the hub plane. The forward velocity component is horizontal in the inertial frame. Note that this equates to a different definition of μ than is used in the helicopter community: $\mu = \frac{V\cos\alpha_s}{\Omega R}$ for helicopters where α_s is the tilt of the shaft, but $\mu = \frac{V}{\Omega R}$ for tiltrotors. V_w as shown below has been transformed into the undeformed frame.

$$V_w = [T_{ur}]\,[T_{rh}]\left([T_{hw}]\,[T_{wi}]\left\{\begin{array}{c}\mu\\0\\0\end{array}\right\} + \left\{\begin{array}{c}0\\0\\-\lambda\end{array}\right\}\right) \qquad (13)$$

The blade velocities in the undeformed frame are found from

$$\begin{aligned}
V_{bh} &= \left\{\begin{array}{c}\dot{x}_1\\ \dot{y}_1\\ \dot{z}_1\end{array}\right\} + [T_{ur}]\left\{\begin{array}{c}0\\0\\ \Omega\end{array}\right\} \times \left\{\begin{array}{c}x_1\\ y_1\\ z_1\end{array}\right\} + [T_{ur}]\,[T_{rh}]\,[T_{hw}]\,[T_{wi}]\left\{\begin{array}{c}\dot{x}_F\\ \dot{y}_F\\ \dot{z}_F\end{array}\right\}\\
&+ \left[[T_{ur}]\,[T_{rh}]\,[T_{hw}]\,[T_{wi}]\left\{\begin{array}{c}-\dot{\phi}_s\\ -\dot{\alpha}_s\\ -\dot{\psi}_s\end{array}\right\}\right] \times \left[\left\{\begin{array}{c}x+u\\ v\\ w\end{array}\right\} + [T_{cu}]^T\,[T_{dc}]^T\left\{\begin{array}{c}0\\ \eta_r\\ 0\end{array}\right\}\right] \qquad (14)
\end{aligned}$$

where Ω is the rotor rotational speed. These aerodynamic loads are calculated using blade section "strip" analysis based on the angle of attack at the section three-quarter chord location; η_r is the chordwise offset between the elastic axis and the 3/4 chord position. U_P, U_T, and U_R are found by totaling the velocities above and transforming them to the deformed frame.

$$\left\{ \begin{array}{c} U_R \\ U_T \\ U_P \end{array} \right\} = [T_{dc}]\,[T_{cu}] \left\{ \begin{array}{c} U_x \\ U_y \\ U_z \end{array} \right\} = [T_{dc}]\,[T_{cu}]\,(V_{bh} - V_w) \tag{15}$$

Once these velocities are expressed in the deformed frame, they can be substituted into the forms for the aerodynamic forces as given above to give the virtual work terms.

3.2.3 Gimbal Modeling

To give some degree of confidence that this tiltrotor model is realistic, it was necessary to model a gimballed hub. The vast majority of wind tunnel data and other analyses for tiltrotors are based on gimballed hubs since the tiltrotors flying today are use gimballed rotors. The gimbal is modeled throughout following the method described in [35] . The gimbal is treated as two additional degrees of freedom of hub motion where

$$\beta_G = \beta_{GC} \cos\psi + \beta_{GS} \sin\psi \tag{16}$$

This β_G is added into the transformation matrices with precone so that the transformation matrix between rotating and undeformed coordinate systems takes the following form.

$$[T_{ur}] = \begin{bmatrix} \cos\beta_p + \sin\beta_p\,(\beta_{GC}\cos\psi + \beta_{GS}\sin\psi) & 0 & -\cos\beta_p\,(\beta_{GC}\cos\psi + \beta_{GS}\sin\psi) + \sin\beta_p \\ 0 & 1 & 0 \\ \cos\beta_p\,(\beta_{GC}\cos\psi + \beta_{GS}\sin\psi) - \sin\beta_p & 0 & \cos\beta_p + \sin\beta_p\,(\beta_{GC}\cos\psi + \beta_{GS}\sin\psi) \end{bmatrix} \tag{17}$$

The effect of the gimbal motion is shown in Fig. 4.

3.2.4 Rigid, Twisted Blade

The resulting kinetic energy terms and work energy terms are simplified to rigid blade coordinates. Many studies have shown that rigid blades can provide a good approximation for stability analyses. This simplification allows comparison with other rigid blade analyses and with equations of motion derived by hand. Also, since the present version of this analysis does not include modal analysis, using a rigid blade keeps the number of degrees of freedom to a minimum.

The primary elastic blade degrees of freedom are simplified to rigid flap and lag degrees of freedom. Extension and elastic twist are not modeled in the rigid blade code.

$$\begin{aligned} u_e &= \phi = 0 \\ v_b &= -\sin\zeta\,(x - e_l) \\ w_b &= \sin\beta\,(x - e_f) \end{aligned} \tag{18}$$

All of the elastic blade terms are simplified in a similar manner; the substitutions are explicitly given in Appendix 8.5. The resulting degrees of freedom for the blade / hub system in the rotating frame are

$$\lfloor\ \beta \quad \zeta \quad x_F \quad y_F \quad z_F \quad \alpha_s \quad \phi_s \quad \psi_s \quad \beta_{GC} \quad \beta_{GS}\ \rfloor \tag{19}$$

The chordwise offset between the blade center of gravity and the elastic axis and the flapwise and chordwise mass moments of inertia per unit length along the blade are preserved. The effects of the foreshortening of the blade are also retained. The rigid blade assumption also allows the integrals associated with this foreshortening to be evaluated. For example,

$$\iint_A v' v'\ d\eta\, d\zeta = x \sin^2 \zeta \tag{20}$$

The results of the other integrals associated with foreshortening are given in Appendix 8.5.

Since the blade is assumed to be rigid, it is then possible to integrate the work and kinetic energy terms out the length of the blade. In both cases the terms are explicit in x; the implicit variation with x comes with blade twist. Both the kinetic energy terms and the work terms are functions of θ_0, the pitch at station x out the length of the blade. Since the blade can be twisted, $\theta_0 = \theta_0\,(x)$. One choice would be to assume a polynomial expansion or similar known form for $\theta_0\,(x)$. However, in this case no assumption is made about θ_0. The blade twist θ_0 is set equal to θ_c at the blade root plus an arbitrary function of x $\theta_{tw}\,(x)$. Since θ_0 is not assumed to be a small angle, θ_0 appears throughout as $\cos\theta_0 = \cos\left(\theta_c + \theta_{tw}\right)$ and $\sin\theta_0 = \sin\left(\theta_c + \theta_{tw}\right)$. For an untwisted blade approximation it is trivial to set θ_{tw} to zero throughout. Each individual term is expressed as $c \int mx^{n1} \cos^{n2}\theta_{tw} \sin^{n3}\theta_{tw} dx$ where c is not a function of x and the constants $n1$, $n2$, and $n3$ vary between 0 and 2. These integrals are left unevaluated until a twist function is specified with the other rotor parameters. This method actually results in fewer terms than assuming a linear twist and integrating into a closed form solution; the need to integrate numerically out the blade is also removed.

3.2.5 Strain Energy

Since a rigid blade assumption has been made, the strain energy for the blade is limited to the springs at the root of the blade.

$$\begin{aligned}
\delta U &= k_\beta \left(\beta - \beta_p\right) \delta\beta + k_\zeta\, \zeta\, \delta\zeta \\
&\quad + k_{\beta_G}\, \beta_{GC}\, \delta\beta_{GC} \cos^2\psi \\
&\quad + \left(k_{\beta_G}\, \beta_{GC}\, \delta\beta_{GS} + k_{\beta_G}\, \beta_{GS}\, \delta\beta_{GC}\right) \cos\psi \sin\psi \\
&\quad + k_{\beta_G}\, \beta_{GS}\, \delta\beta_{GS} \sin^2\psi
\end{aligned} \tag{21}$$

3.2.6 Structural Coupling

Structural coupling between the blade flap and lag is modeled as shown in Fig. 5. This allows a better approximation of a hingeless blade as R is allowed to vary between 0 and 1. The structural coupling terms appear only in the stiffness matrix in the flap and lag equations [2] .

3.2.7 Linearization

These strain, kinetic, and work energies are linearized by assuming that each of the degrees of freedom is equal to a steady value plus a perturbation: for example, $\beta = \bar{\beta} + \delta\beta$. This substitution is exact–no simplification is assumed here. The next step, however, is to assume that products of perturbations are small: $\delta\beta \cdot \delta\zeta = 0$, for example. As long as the response routine is of sufficient accuracy, this assumption is reasonable. The resulting steady equations become a response routine. If the hub were assumed fixed in space, Hamilton's principle could be applied at this point to produce equations of motion. With pylon and wing motion, the kinetic, strain, and work energies from the blade and hub must be added into the kinetic, strain, and work energies for the pylon and wing before Hamilton's principle can be applied. However, it is convenient to express the linearized perturbation values for the blade/hub kinetic, strain, and work energies in the form of preliminary $[M_{blade}]$, $[C_{blade}]$, and $[K_{blade}]$ matrices. A Fourier coordinate transformation is applied to transform the rotating system coordinates for each blade into fixed-frame coordinates. The resulting fixed-frame matrices are assembled with the resulting wing and pylon kinetic, strain, and work energies to give equations of motion for the entire model as described below.

$$[M]\{\ddot{q}\} + [C]\{\dot{q}\} + [K]\{q\} = \{F\} \tag{22}$$

3.3 Pylon and Wing Attachment

The pylon is modeled as a rigid connection between the hub and the wing. The kinetic energy associated with the motion of the pylon mass and inertia is added to the kinetic energy associated with the wing-tip motion and the hub motion resulting in additional terms in the total mass matrix.

$$[M_{pylon}]\left\{\begin{array}{c} \ddot{x}_P \\ \ddot{y}_P \\ \ddot{z}_P \\ \ddot{\phi}_P \\ \ddot{\alpha}_P \\ \ddot{\psi}_P \end{array}\right\} = \begin{bmatrix} m_{Fx} & 0 & 0 & 0 & 0 & 0 \\ 0 & m_{Fy} & 0 & 0 & 0 & 0 \\ 0 & 0 & m_{Fz} & 0 & 0 & 0 \\ 0 & 0 & 0 & I_{\phi_s} & 0 & 0 \\ 0 & 0 & 0 & 0 & I_{\alpha_s} & 0 \\ 0 & 0 & 0 & 0 & 0 & I_{\psi_s} \end{bmatrix}\left\{\begin{array}{c} \ddot{x}_P \\ \ddot{y}_P \\ \ddot{z}_P \\ \ddot{\phi}_P \\ \ddot{\alpha}_P \\ \ddot{\psi}_P \end{array}\right\} \tag{23}$$

where the degrees of freedom x_P to ψ_P are related to the wing-tip degrees of freedom as described below. To accurately predict the coupling between the wing torsion and vertical bending, three displacements in the x, y, and z directions are allowed between the pylon center of gravity and the hub (x_{CG}, y_{CG}, h) and three additional displacements between the pylon center of gravity and the wing attachment point $(x_{pcg}, y_{pcg}, z_{pcg})$(see Fig. 1 above). The offsets in the z direction h and z_{pcg} are important because the rotor and pylon mass offset from the wing couples wing bending and torsion. These offsets are taken into account in the assembly process.

The pylon is attached to the wing with a downstop spring, a torsional spring between the wing-tip and the pylon in the direction of the pylon rotation. As the pylon is rotated forward into forward flight mode on current tiltrotors, the pylon is locked into position with the wing. This spring and locking mechanism are modeled by allowing motion between the pylon pitch and the wing-tip pitch thus creating an additional degree of freedom for the total system. The locking mechanism is modeled by allowing the spring to be very large in forward flight. The hub motion is calculated in terms of the pylon pitch ϕ_{N+2} while the wing motion is calculated in terms of the wing-tip pitch ϕ_{N+1}. These two degrees of freedom are related by the strain energy associated with the downstop spring. This strain energy adds into the strain energy for the blades and the wing providing additional terms in the total stiffness matrix.

$$[K_{downstop}] \left\{ \begin{array}{c} \phi_{N+1} \\ \phi_{N+2} \end{array} \right\} = k_{spring} \left[\begin{array}{cc} 1 & -1 \\ -1 & 1 \end{array} \right] \left\{ \begin{array}{c} \phi_{N+1} \\ \phi_{N+2} \end{array} \right\} \tag{24}$$

3.4 Elastic Wing

The wing is assumed to be an elastic beam and modelled using the finite element method as shown in Fig. 6. Each node has 5 degrees of freedom: extension in the wing is constrained to zero. At each node the degrees of freedom are

$$\{q_{node}\} = \lfloor \; v \quad v' \quad w \quad w' \quad \phi \; \rfloor \tag{25}$$

in the directions shown above.

3.4.1 Kinetic Energy

The kinetic energy for the beam element is, by definition,

$$\delta T_{el} = \int_V \rho \, \delta \hat{u}^T \, \hat{\ddot{u}} \, dV \tag{26}$$

For a beam with an offset y_{CM} between the center of gravity and the elastic axis, the displacement vector is given as

$$\hat{u} = \left\{ \begin{array}{c} u \\ v \\ w + y_{CM}\phi \end{array} \right\} \tag{27}$$

The shape functions used to model the wing are as follows:

$$\begin{aligned}
u(x,t) &= \left[\begin{array}{cc} \left(1 - \frac{x}{L}\right) & \frac{x}{L} \end{array} \right] \left\{ \begin{array}{c} u_A \\ u_B \end{array} \right\} \\
\phi(x,t) &= \left[\begin{array}{cc} \left(1 - \frac{x}{L}\right) & \frac{x}{L} \end{array} \right] \left\{ \begin{array}{c} \phi_A \\ \phi_B \end{array} \right\} \\
v(x,t) &= \left\{ \begin{array}{c} 1 - 3\left(\frac{x}{L}\right)^2 + 2\left(\frac{x}{L}\right)^3 \\ L\left(\left(\frac{x}{L}\right) - 2\left(\frac{x}{L}\right)^2 + \left(\frac{x}{L}\right)^3\right) \\ 3\left(\frac{x}{L}\right)^2 - 2\left(\frac{x}{L}\right)^3 \\ L\left(-\left(\frac{x}{L}\right)^2 + \left(\frac{x}{L}\right)^3\right) \end{array} \right\}^T \left\{ \begin{array}{c} v_A \\ v'_A \\ v_B \\ v'_B \end{array} \right\} \\
w(x,t) &= \left\{ \begin{array}{c} 1 - 3\left(\frac{x}{L}\right)^2 + 2\left(\frac{x}{L}\right)^3 \\ L\left(\left(\frac{x}{L}\right) - 2\left(\frac{x}{L}\right)^2 + \left(\frac{x}{L}\right)^3\right) \\ 3\left(\frac{x}{L}\right)^2 - 2\left(\frac{x}{L}\right)^3 \\ L\left(-\left(\frac{x}{L}\right)^2 + \left(\frac{x}{L}\right)^3\right) \end{array} \right\}^T \left\{ \begin{array}{c} w_A \\ w'_A \\ w_B \\ w'_B \end{array} \right\}
\end{aligned} \tag{28}$$

Making these substitutions and carrying out the math gives an element mass matrix. The complete wing matrices are given in Appendix 8.6. Note that the wing vertical bending and torsion are coupled due to the chordwise offset between the wing center of gravity and the elastic axis. It is assumed that any offset between the center of gravity and the elastic axis in the z direction (perpendicular to the chord) is small enough to be neglected.

$$\begin{aligned}
\delta T_{el} &= \left\{ \begin{array}{c} \delta u_A \\ \delta v_A \\ \delta v'_A \\ \delta w_A \\ \delta w'_A \\ \delta \phi_A \\ \delta u_B \\ \delta v_B \\ \delta v'_B \\ \delta w_B \\ \delta w'_B \\ \delta \phi_B \end{array} \right\} \left[M^S\right] \left\{ \begin{array}{c} \ddot{u}_A \\ \ddot{v}_A \\ \ddot{v}'_A \\ \ddot{w}_A \\ \ddot{w}'_A \\ \ddot{\phi}_A \\ \ddot{u}_B \\ \ddot{v}_B \\ \ddot{v}'_B \\ \ddot{w}_B \\ \ddot{w}'_B \\ \ddot{\phi}_B \end{array} \right\} \\
&= \delta \hat{U}^T \left[M^S\right] \hat{\ddot{U}}
\end{aligned} \tag{29}$$

Though the extension degree of freedom u is shown in the degree of freedom vector here, the extension in the wing is later constrained to be zero.

3.4.2 Strain Energy

The definition of strain energy can be applied with the shape functions given above to calculate an element stiffness matrix.

$$\begin{aligned} U_{el} &= \frac{1}{2}\int_0^L EA\left(\frac{\partial u(x,t)}{\partial x}\right)^2 dx + \frac{1}{2}\int_0^L GJ\left(\frac{\partial \phi(x,t)}{\partial x}\right)^2 dx \\ &+\frac{1}{2}\int_0^L EI_z\left(\frac{\partial^2 v(x,t)}{\partial x^2}\right)^2 dx + \frac{1}{2}\int_0^L EI_y\left(\frac{\partial^2 w(x,t)}{\partial x^2}\right)^2 dx \end{aligned} \tag{30}$$

$$\delta U_{el} = \hat{U}^T\left[K^S\right]\hat{U} \tag{31}$$

This form of the strain energy for the wing is modified with the inclusion of the aeroelastic couplings as described below.

3.4.3 Work Energy

The angle of attack of the wing is given by

$$\alpha = \alpha_0 + \phi\cos\Lambda - \frac{\dot{w}}{V} - w'\sin\Lambda \tag{32}$$

Note that wing sweep Λ is included which is important because Nixon found wing sweep to be destabilizing [34] .

The forces are given by

$$\hat{P} = \begin{Bmatrix} L_u \\ L_v \\ M_z \\ L_w \\ M_y \\ M_\phi \end{Bmatrix} = \begin{Bmatrix} 0 \\ 0 \\ 0 \\ \frac{1}{2}\rho V^2 c c_{l_\alpha}\left(\alpha_0 + \phi\cos\Lambda - \frac{\dot{w}}{V} - w'\sin\Lambda\right) \\ 0 \\ \frac{1}{2}\rho V^2 c c_{l_\alpha} e\left(\alpha_0 + \phi\cos\Lambda - \frac{\dot{w}}{V} - w'\sin\Lambda\right) \end{Bmatrix} \tag{33}$$

where e is the chordwise distance of the elastic axis behind the aerodynamic center.

The virtual work for the element is given by definition as

$$\delta W_{el} = \int_0^L \hat{P}\,\delta\hat{U}\,dx \tag{34}$$

Substituting in the same shape functions as above gives aerodynamic stiffness and damping matrices for the wing element. These matrices are given explicitly in Appendix 8.6.

$$\delta W_{el} = \delta \hat{U} \left(\left\{ F^A \right\} + \left[K^A \right] \hat{U} + \left[C^A \right] \widehat{\dot{U}} \right) \tag{35}$$

3.5 Assembly

Once the kinetic, strain, and work energies are calculated from the blade, hub, pylon, and wing, Hamilton's principle can be applied to assemble all of these energies into total system equations of motion. The $[M_{blade}]$, $[C_{blade}]$, and $[K_{blade}]$ from the rotor are combined into total system $[M]$, $[C]$, and $[K]$ by equating the wing-tip degrees of freedom to the hub motion degrees of freedom. Since the pylon is rigid, this is just a one-to-one correspondence that can be expressed as a transformation matrix. The single exception is due to the addition of the downstop spring which is modeled as an extra torsion degree of freedom in the total degree of freedom vector.

Since the hub degrees of freedom x_F, y_F, z_F, α_s, ϕ_s, and ψ_s from the hub and blade equations are defined in the inertial frame, the hub degrees of freedom can be equated to the wing tip degrees of freedom in a one-to-one fashion.

$$\left\{ \begin{array}{c} x_h \\ y_h \\ z_h \\ -\alpha_h \\ -\phi_h \\ \psi_h \end{array} \right\} = \begin{bmatrix} 0 & 1 & 0 & 0 & 0 & 0 \\ 1 & 0 & 0 & 0 & 0 & 0 \\ 0 & 0 & 0 & 1 & 0 & 0 \\ 0 & 0 & 0 & 0 & 0 & 1 \\ 0 & 0 & 0 & 0 & 1 & 0 \\ 0 & 0 & -1 & 0 & 0 & 0 \end{bmatrix} \left\{ \begin{array}{c} u \\ v \\ v' \\ w \\ w' \\ \phi \end{array} \right\} \equiv [EE] \left\{ \begin{array}{c} u \\ v \\ v' \\ w \\ w' \\ \phi \end{array} \right\} \tag{36}$$

This transformation becomes complicated by the six offsets. A rotation of the wing tip produces displacements at the hub because of the offsets x_{CG}, y_{CG}, and h between the pylon center of gravity and the hub and because of the offsets x_{pcg}, y_{pcg}, and z_{pcg} between the pylon center of gravity and the wing tip. The exact transformations are given in Appendix 8.7.

A numerical Fourier Coordinate Transformation is applied to the assembled mass, stiffness, and damping matrices to transform the rotating frame flap and lag into fixed frame coordinates [8] . The resulting total degree of freedom vector consists of the five degrees of freedom at each wing finite element node, the blade flap and lag terms, and the gimbal terms. Note the presence of

ϕ_{N+2} in the last blade element which is the extra ϕ degree of freedom due to the presence of the downstop spring.

$$\begin{aligned}
\{q_{tot}\} &= \lfloor\, El_1 \;\; \ldots \;\; El_N \;\; blade \;\; El_{N+1} \;\; gimbal \,\rfloor^T \qquad (37)\\
\lfloor\, El_1 \,\rfloor &= \lfloor\, v_1 \;\; v_1' \;\; w_1 \;\; w_1' \;\; \phi \,\rfloor \\
\lfloor\, El_N \,\rfloor &= \lfloor\, v_N \;\; v_N' \;\; w_N \;\; w_N' \;\; \phi_N \,\rfloor \\
\lfloor\, El_{N+1} \,\rfloor &= \lfloor\, v_{N+1} \;\; v_{N+1}' \;\; w_{N+1} \;\; w_{N+1}' \;\; \phi_{N+1} \;\; \phi_{N+2} \,\rfloor \\
\lfloor blade \rfloor &= \lfloor\, \beta_0 \;\; \beta_{1c} \;\; \beta_{1s} \;\; \cdots \;\; \zeta_0 \;\; \zeta_{1c} \;\; \zeta_{1s} \;\; \cdots \,\rfloor \\
\lfloor\, gimbal \,\rfloor &= \lfloor\, \beta_{GC} \;\; \beta_{GS} \,\rfloor
\end{aligned}$$

3.6 Response

Once the total system matrices are assembled, the response is needed, in this case the coning and pitch setting. The steady values of the blade and hub degrees of freedom are assumed to be zero in all cases except coning. A value for θ_{75} or c_T must be given. The inflow equation comes from momentum theory while the coning and thrust equations are found from the steady terms in the equations of motion as described above. The coupled response routine uses a Newton-Raphson iteration to calculate the coning β_0, the resulting inflow λ, and the unknown of θ_{75} or c_T.

3.7 Stability Analysis

The mass, damping, and stiffness matrices for the entire system can now be calculated. The forcing vector is set to zero for the stability calculation and the resulting matrices are transformed to state space form.

$$[M]\{\ddot{u}\} + [C]\{\dot{u}\} + [K]\{u\} = \{0\} \rightrightarrows \begin{bmatrix} [0] & [M] \\ [M] & [C] \end{bmatrix} \{\dot{y}\} + \begin{bmatrix} -[M] & [0] \\ [0] & [K] \end{bmatrix} \{y\} = \{0\} \quad (38)$$

The stability of the degrees of freedom is calculated from the eigenvalues. Currently stability analyses can be conducted by varying either the rotor rotational speed, Ω, or the forward speed of the tiltrotor, V.

3.8 Modeling of Couplings

The sections above describe the modeling and analysis approach for a baseline model. This section describes how the couplings in the wing and blade are implemented.

The composite couplings in the wing modify the wing strain energy as shown below

$$U_{el} = \frac{1}{2}\int_0^L \left[EA\left(u'\right)^2 + GJ\left(\phi'\right)^2 + EI_z\left(v''\right)^2 + EI_y\left(w''\right)^2 + 2\left(K_{46}v'' + K_{45}w''\right)\phi'\right] dx \tag{39}$$

Thus K_{45} couples wing vertical bending and twist while K_{46} couples wing chordwise bending and twist. The sign convention used here is that positive wing vertical bending-twist coupling is when the blade bends up and the nose of the airfoil pitches up ($K_{45} > 0$). Wing chord bending-twist coupling is defined as positive when the blade bends forward and the nose pitches up ($K_{46} > 0$).

The kinematic couplings in the blades are included as changes in the effective twist.

$$\begin{aligned} \theta_0 &= \theta_0 - \beta\tan\delta_3 - \zeta\tan\delta_4 + \tan\delta_{3G}\left(\beta_{GC}\cos\psi + \beta_{GS}\sin\psi\right) \\ &= \theta_0 - \beta k_{p_\beta} - \zeta k_{p_\zeta} + k_{p\beta G}\left(\beta_{GC}\cos\psi + \beta_{GS}\sin\psi\right) \end{aligned} \tag{40}$$

These coupling terms appear everywhere that the pitch does. For example, the transformation matrix between the cross-section frame of reference and the undeformed frame is given by

$$[T_{cu}] = \begin{bmatrix} 1 & 0 & 0 \\ 0 & \cos\theta_0 & \sin\theta_0 \\ 0 & -\sin\theta_0 & \cos\theta_0 \end{bmatrix} \tag{41}$$

With the blade couplings and gimbal degrees of freedom included, the $[T_{cu}]$ matrix becomes

$$T_{cu} = \begin{bmatrix} 1 & 0 & 0 \\ 0 & \left(1+T^1_{cu}\right)\cos\theta_0 + T^2_{cu}\sin\theta_0 & -T^2_{cu}\cos\theta_0 + \left(1+T^1_{cu}\right)\sin\theta_0 \\ 0 & T^2_{cu}\cos\theta_0 - \left(1+T^1_{cu}\right)\sin\theta_0 & \left(1+T^1_{cu}\right)\cos\theta_0 + T^2_{cu}\sin\theta_0 \end{bmatrix} \tag{42}$$

where

$$\begin{aligned} T^1_{cu} &= -k_{p\beta}\,\beta\,k_{p\zeta}\,\zeta + \left(k_{p\beta}\,\beta + k_{p\zeta}\,\zeta\right)\left(k_{p\beta G}\,\beta_{GC}\,\cos\psi + k_{p\beta G}\,\beta_{GS}\,\sin\psi\right) \\ T^2_{cu} &= k_{p\beta}\,\beta + k_{p\zeta}\,\zeta - k_{p\beta G}\,\beta_{GC}\,\cos\psi - k_{p\beta G}\,\beta_{GS}\,\sin\psi \\ &\quad + k_{p\beta}\,\beta\,k_{p\zeta}\,\zeta\left(k_{p\beta G}\,\beta_{GC}\,\cos\psi + k_{p\beta G}\,\beta_{GS}\,\sin\psi\right) \end{aligned} \tag{43}$$

The transformation matrix between the deformed frame and the cross-section frame is also altered by the inclusion of the blade couplings. This matrix is given explicitly in Appendix 8.4. The δ_3 terms couple blade flap and pitch while δ_4 couples blade lag and pitch. Positive pitch-flap coupling is defined to be when the blade flaps up and the nose pitches down ($\delta_3 > 0$). Positive pitch-lag coupling is when the blade lags back and the nose pitches down ($\delta_4 < 0$). The blade couplings are included in the response calculations as well as in the stability calculations.

4 Validation

This section details the validation study which was conducted to give confidence in the present analysis. Comparisons were made for both a Boeing model which was hingeless and soft-inplane and for a Bell model which was gimballed and stiff-inplane. Several abbreviations are used in labeling the modes: WV=wing vertical bending, WC=wing chord bending, WT=wing torsion, LFL=low frequency rotor lag, HFL=high frequency rotor lag, CL=collective lag, LFF=low frequency rotor flap, HFF=high frequency rotor flap, CF=collective rotor flap, LFG=low frequency gimbal flapping motion, and HFG=high frequency gimbal flapping motion.

4.1 Comparison with Hingeless Rotor for Air Resonance

In 1973 Boeing conducted two wind-tunnel tests of the Model 222 rotor in the NASA Ames 40' by 80' wind tunnel [26] . This was a full-scale, semi-span model with a 25-foot-diameter rotor (Fig. 7). The main purpose of this tunnel entry was to gather performance and aeroelastic data about the Model 222 to validate Boeing's analysis of that rotor. Regions of degraded stability in forward flight were observed. Testing was done only in forward flight mode; no ground resonance data was accumulated.

Four different wind tunnel speeds were used: 50 knots, 100 knots, 140 knots, and 192 knots. Damping for the wing modes and frequencies for the wing vertical bending were gathered. The data from these wind tunnel tests along with the Boeing analysis of that time are the primary sources of validation for the current analysis. More data was accumulated for the 100 knot run so that will be the focus of the validation and preliminary studies.

4.1.1 Fifty Knots

Fig. 8 shows the damping for the wing modes for the Boeing damping as measured at 50 knots. The frequencies are not reported for 50 knots. The circles indicate data gathered at 50 knots while the triangles show data gathered at 60 knots in the wind tunnel. Both analyses shown are for 50 knots wind tunnel speed. The wing vertical bending damping shown by the current analysis matches Boeing's analysis and the wind tunnel data well. The wing chord damping analyses differ by approximately 2% critical damping offset. The wing torsion mode is also predicted to be less damped by the current analysis. The high frequency lag mode is also shown here for the current analysis because of the high degree of coupling between this mode and the torsion mode around 280 RPM.

4.1.2 One-Hundred Knots

Shown in Fig. 9 and 10 are the frequencies and damping as given for the wind tunnel test, the Boeing analysis, and the current analysis at 100 knots [26] . The circles are the wind tunnel data that was generated. Boeing's analysis is shown in dotted lines while the current analysis is solid. The frequencies predicted by Boeing's analysis and the current analysis match well. In general the wing frequencies predicted by the current analysis are higher than the wing frequencies predicted by Boeing's analysis. One possible source of error here comes from the lack of data given in the report [26] : the wing frequencies (blades off) are reported as 2.5 Hz for wing vertical bending, 4.5 Hz for wing chord bending, and 11.3 Hz for wing torsion. Values for the stiffnesses EI_y, EI_z, and GJ are not explicitly given. These parameters were estimated based on the weight of the wing and pylon. It is assumed that Boeing's analysis is based on the actual stiffnesses of the wing design.

One discrepancy is in the wing torsion mode. Boeing's wing torsion mode is shown to vary from 4 Hz at 100 RPM to more than 10 Hz at 600 RPM. A body frequency varying by that magnitude with change in a rotor rotational speed is considered unlikely. However, this mode is matched well by the current analysis' high frequency lag mode for lower RPM and is matched less well at high RPM by the current analysis' wing torsion mode. The vertical lines at 260 RPM and 380 RPM shown in the current analysis are regions where the wing torsion mode couples very strongly with high frequency flap around 260 RPM and with high frequency lag around 380 RPM. The high frequency flap and lag mode frequencies clearly increase with rotor RPM. In the regions indicated, choosing one frequency for high frequency flap and the other frequency for wing torsion is inaccurate. Barkai and Rand label both frequencies in these regions with both modes, e.g., high frequency flap/wing torsion mode, which is one way of indicating these strongly coupled modes [1].

The damping results show more discrepancies with the Boeing analysis than do the frequency results. As in the 50 knot case, the high frequency lag mode is also shown for the current analysis. Since this stability data is shown as a critical damping value, the discrepancy discussed for the wing torsion mode frequency above will affect the wing torsion damping shown here. The wing vertical damping predicted matches the wind tunnel data fairly well and certainly shows a region of air resonance as seen in the wind tunnel. The shift of the instability to higher RPM is probably due to the higher frequency predicted for the wing vertical bending mode. The wing chord mode damping as predicted by the current analysis is similar in tendency to Boeing's analysis but differs in magnitude by approximately 2%. The wing torsion mode is similarly affected. This shift in damping is currently not understood.

4.1.3 One-Hundred Forty Knots

Fig. 11 and 12 show the frequency and damping for the wind tunnel test at 140 knots along with the Boeing analysis and the current analysis. The circles indicate wind tunnel data gathered at 140 knots. This shows that the wing vertical bending damping correlates well with the wind tunnel data for various forward speeds. Again the frequency data is excellent. The wing chord damping analyses differ by the same 2% critical damping offset at high RPM. The wing torsion mode is also predicted to be less damped by the current analysis. The high frequency lag mode is also shown here for the current analysis because of the high degree of coupling between this mode and the torsion mode around 280 RPM.

4.1.4 Discussion

The calculation of the steady coning, inflow, and pitch or thrust requires that one of the pitch and thrust be given over the rotor rotational speeds to be tested. The Boeing report included the pitch settings for the wind tunnel testing but not the pitch settings used in the accompanying analysis. Data for the θ_{75} setting was only available for 7 test points between 320 and 412 knots for the 50 knot test, for 24 test points between 104 and 470 knots for the 100 knot test, for 11 test points between 384 and 491 knots for the 140 knot case, and for 7 test points between 315 and 386 knots for the 192 knot test. Linear interpolation was used to estimate θ_{75} values outside of these ranges. Because of the additional data available for the 100 knot case, all of the results shown in forward flight mode in the next section were run at 100 knots. This data is shown graphically in Fig. 13 where the crosses mark values given and the line shows data used for this analysis.

Choices of which modes to model also affect the results. For example, Fig 14. shows how including the collective lag mode in the stability analysis changes the behavior of the wing chord damping. The dotted lines are the wing chord bending and rotor collective lag modes as predicted by the current analysis for frequencies and damping. The solid lines are taken from the current analysis results having excluded the collective lag mode. This change in behavior calls into question exactly what modeling assumptions were made for the Boeing analysis, specifically whether or not the high frequency rotor flap and lag were included. This change in behavior of the wing chord mode is not expected from helicopter theory: the collective lag mode does not couple with the body modes to create an air resonance situation as is seen here. Only the low frequency lag mode is crucial for determining the stability of a helicopter from air and ground resonance.

The airfoil data is not available. Nor are the blade effective hinge offsets or blade non-rotating natural frequencies. These parameters have been approximated for use in the current analysis. The damping is quite sensitive to some of the approximated parameters. Lack of data such as this could account for some of the discrepancies between the Boeing analysis and the current analysis.

4.2 Comparison with Gimballed Rotor for Whirl Flutter Analysis

Confidence with a model's accuracy comes when the model predicts the same behavior as seen in wind tunnel results and other analyses. Since the majority of research conducted with tiltrotors concerns whirl flutter, it is important that the current analysis predict whirl flutter accurately even though this is not the primary emphasis of this research. The current model includes the gimballed hub specifically for this reason. The gimballed hub modeled here is a Bell Helicopter hub on the same NASA wing as used above. The first comparison is made with the response predictions from Nixon's elastic blade code in UMARC as in Fig. 15 [35] , [3] . The c_T values are given and the pitch settings are calculated. This result gives confidence that the response calculation is consistent with that of other analyses.

The results to be compared next are from Nixon's rigid blade model [35] . Fig. 16 shows the frequencies for the whirl flutter analysis which is plotted with increasing velocity rather than increasing rotor rotational speed as for ground resonance. The solid lines are the current analysis while the dotted lines represent Nixon's analysis. The collective lag motion is not shown. The agreement between the prediction of the frequencies is excellent. The corresponding damping values are given in Fig. 17. Again, the current analysis is shown with solid lines while Nixon's analysis is shown using dotted lines. The agreement in the damping is not good. The wing mode damping is smaller for the current analysis prediction as was true for the soft-inplane validation study. In addition, this analysis predicts more lag damping and less flap damping than does Nixon's analysis.

4.3 Summary of Validation

The air resonance trends shown by the Boeing wind tunnel test from 1973 are well predicted. The wind tunnel data that was obtained is matched well. The differences in modeling coupled with the lack of data could easily account for the differences seen in the Boeing analysis and the current analysis. The response routine matches very well with results from Johnson and Nixon [17] , [35] . The whirl flutter frequencies are also in very good agreement with Nixon's analysis. The damping values for whirl flutter remain suspect and require additional attention. These validation studies, though not totally completed, give enough confidence in the prediction of tiltrotor air resonance to justify a first parametric study to examine the use of couplings to stabilize the air resonance instabilities shown.

5 Preliminary Results and Discussion

The preliminary results presented here can be divided into four parts based on the couplings discussed: wing vertical bending-twist coupling, wing chordwise bending-twist coupling, blade pitch-flap coupling, and blade pitch-lag coupling. For each coupling the situations of air resonance in forward flight mode, air resonance in hover mode, and ground resonance in a non-thrusting case must be considered. Unlike in a helicopter where the zero-thrust case also entails adding the landing gear stiffness and damping if present, the ground contact case for the present model tiltrotor does not change the stiffness or damping matrices. The hover case is for a nominal value of $\frac{c_T}{\sigma} = 0.2$ for all RPMs. This gives values of θ_{75} of around 15 degrees.

The baseline frequency and damping for the 100 knots case is given above in the validation section. The baseline frequencies and damping for the hover case are given in Fig. 19 and 20. In the forward flight mode the wing vertical bending is very lightly damped. However, in the hover mode, the wing vertical bending couples with the vertical plunge motion of the rotor which is very heavily damped. This increase in damping in the wing vertical mode eliminates the air resonance seen in forward flight mode. Note also that the nominal RPM for the hover configuration changes to 551 RPM from the forward flight nominal RPM of 386. This hover case assumes that the wind tunnel velocity is zero since the analysis currently assumes constant-coefficient matrices.

The baseline frequencies and damping for the zero-thrust case are given in Fig. 21 and 22. The zero-thrust case is also in helicopter mode so again the nominal RPM is 551 RPM. Note that the cyclic lag mode is included in these figures.

For each type of coupling, the first question examined was whether the positive and negative coupling of that type stabilized, destabilized, or had no effect on air resonance. Couplings which destabilized air resonance were no longer considered. If a positive or negative coupling was shown to stabilize air resonance (or to have only little effect), the effect of that coupling was examined on hover and zero-thrust conditions. If hopeful conditions were found for a given coupling for forward flight, hover, and zero thrust, then whirl flutter was considered.

5.1 Wing Vertical Bending-Twist Coupling

Wing vertical bending-twist coupling was defined as positive with bending up coupled to nose-up twist, i.e., $K_{45} > 0$. Negative beamwise bending-twist coupling ($K_{45} < 0$) destabilizes air resonance. Positive beamwise bending-twist coupling ($K_{45} > 0$) tends to stabilize air resonance (Fig. 23). This destabilizes the zero-thrust and hover conditions slightly but since this tiltrotor is extremely stable in these conditions the destabilizing trend is unimportant (Fig. 24 and 25).

5.2 Wing Chordwise Bending-Twist Coupling

Recall that the wing chordwise bending-twist coupling was defined as positive when the wing bends forward and twists nose up, or $K_{46} > 0$. The effects of chordwise bending-twist coupling on air resonance, hover, and zero-thrust conditions was quite small. This coupling did not stabilize the existing air resonance in the Boeing baseline model. If this coupling was required for some other purpose, it is good to know that this coupling does not significantly harm air or ground resonance but neither does it stabilize these conditions.

5.3 Blade Pitch-Flap Coupling

Blade pitch-flap coupling is defined above to be positive when blade flapping up couples with blade twist nose-down, $\delta_3 > 0$. Both the positive and negative pitch-flap couplings destabilized the air resonance in the baseline case, though the effect was not very strong.

5.4 Blade Pitch-Lag Coupling

Let pitch-lag be positive when the blade lags back and pitches nose-down, $\delta_4 < 0$. The negative pitch-lag coupling destabilized the air resonance. However, the positive pitch-lag coupling stabilized the air resonance in the baseline rotor (Fig. 26). These graphs show the blade low frequency lag and the wing vertical bending. The solid line on these graphs is the baseline case, the dot-dashed line indicates -5 degrees and the dotted line shows -10 degrees. The pitch-lag coupling on this tiltrotor's air resonance instability is found to be effective. This result is in line with what helicopter studies have found [36] . However, this positive pitch-lag coupling in helicopters destabilizes the ground resonance instability.

Fig. 27 and 28 show the hover and zero-thrust damping values for the Boeing model. The addition of positive pitch-lag coupling does not destabilize the hover or ground condition. This is unlike a the results for a helicopter. One possible cause for this comes from the difference in stiffness and damping due to the landing gear on a helicopter which become ineffective in forward flight. The wing vertical bending mode modeled here does not show that loss in stiffness or damping on take-off.

5.5 Discussion

The aeroelastic couplings discussed here impact the stability of the tiltrotor in air resonance. The two couplings which show promise for stabilizing air resonance without destabilizing hover or ground resonance are positive wing beamwise bending-twist coupling ($K_{45} > 0$ where the wing bends up and pitches nose-up) and positive blade pitch-lag coupling ($\delta_4 < 0$ where the blade lags back and pitches nose-down). Before incorporating these couplings into tiltrotors, it must be shown that these couplings do not destabilize the tiltrotor in transition or forward flight in hover mode nor significantly decrease whirl flutter stability margins.

Published whirl flutter coupling results show that chordwise bending forward-pitch nose down coupling within the wing can add significant stability to the system for whirl flutter ($K_{46} < 0$). Barkai and Rand showed that wing vertical bending up-pitch nose-up coupling also adds to the system stability ($K_{45} > 0$) [1] . Popelka et al. showed that tailoring the wing so that as the wing bends up the pylon pitches nose down could increase the whirl flutter stability ($K_{45} < 0$) [39] . These effects seem to be altered by the inclusion of blade elasticity which was included for Barkai and Rand but not for Popelka et al.

Nixon showed that flatwise bending-twist coupling in the blades could also increase the whirl flutter stability margin when flatwise-bending up coupled with nose-down twist; this coupling tends to offset the precone induced pitch-lag coupling which is destabilizing for whirl flutter [35] . Tiltrotor blades are highly twisted and use large collective pitches. The chord line angle with the rotor plane of rotation is very large. The flatwise bending is defined as bending perpendicular to the plane of rotation. Thus, Nixon's study on flatwise-bending twist coupled blades indicates that positive pitch-lag coupled blades could detrimentally affect the stability in whirl flutter. More research is clearly needed here to assess the effects of these couplings on whirl flutter.

6 Further Research

The preliminary results described above indicate a potential for these couplings which merits further study. Several refinements are needed and extensive parametric studies should be conducted to expand the understanding of if and how these couplings can stabilize air and ground resonance for a soft-inplane tiltrotor. The first step is to understand exactly why the gimballed rotor damping does not match with Nixon's predictions. As soon as that is completed, refinements can be made to the model itself.

The first additional feature to be added is the free flight degrees of freedom for the fuselage. The model above assumes from the outset that the root of the wing is fixed in space: the rigid body motion of the entire tiltrotor is not modeled. These free-flight degrees of freedom could also experience air or ground resonance. The study conducted by Srinivas in 1995 included these body modes as well as the second rotor and wing. The antisymmetric modes of vibration for the wing were therefore modeled as well as the symmetric modes which are modeled here. Srinivas showed that for the baseline case he tested, the whirl flutter stability was governed by the symmetric modes [46] . It is not clear how the antisymmetric modes will affect ground and air resonance of a tiltrotor. These modes need to be addressed and studied. This modification will also include horizontal tail effects and free-flight vehicle trim.

The flexibility in the pylon should also be included. The rigid pylon assumption is not unreasonable, but since flexibility in the pylon could change the dynamics of the coupling between the rotor and the wing, it is important to model whatever flexibility exists. This is especially important for whirl flutter results where the flexibility in the pylon can certainly affect the results.

One of the serious limitations in the model as it stands now is the need to be either in hover or in airplane mode since the mass, damping, and stiffness matrices are assumed to have constant coefficients. This limitation eliminates forward flight in helicopter mode and transition. Floquet theory will be implemented to allow non-constant matrices for the stability analysis. The finite element method in time will be implemented to calculate the response. Note that the arbitrary pylon tilt is already modeled. Other possible improvements would be the use of unsteady aerodynamics.

The earliest models of ground resonance show that damping must be added in both the fixed frame and in the rotating frame to stabilize air and ground resonance. In the case of a helicopter this usually entails lag dampers on the blade and dampers on the landing gear. In the case of a tiltrotor, damping in the rotating frame could still be provided by lag dampers on the blades, but damping in the fixed frame for a tiltrotor could pose more problems since adding damping to the lightly damped wing modes is less straightforward. The couplings discussed above could certainly help the stability. However if these couplings prove to be inadequate to stabilize a soft-inplane tiltrotor, another suggestions is to use other damping in the wing to increase the fixed-frame damping. Parametric studies need to be conducted to establish how much damping is needed in the fixed frame and how much is already accounted for from aerodynamics.

7 Proposed Time Line, Publications, and Presentations

Validation studies will be completed by the fall semester. The difference in the damping values for the wing chord and wing torsion modes must be accounted for before an abstract can be submitted. The first abstract deadline of interest would be for the AIAA SDM conference on August 1, 1999. The abstract deadline for the AHS Forum 2000 is September 1, 1999.

With a completely validated model, the fuselage rigid body motion will be added. The preliminary studies of the blade couplings δ_3 and δ_4 and the wing couplings K_{45} and K_{46} must be completed. These studies will have accomplished the tasks of exploring the possibility of air and ground resonance in a tiltrotor and evaluating the potential for composite couplings to stabilize these instabilities. If the validation and parametric studies are completed, an abstract will be submitted for the AHS Forum 2000.

Once these studies are completed, the additional model refinements will need to be implemented. Flexibility in the pylon, Floquet theory in stability and response codes, unsteady aerodynamics, and dynamic inflow must all be implemented. The goal is to have these in place by summer, 2000. At this point extensive parametric studies must be completed to completely understand the phenomena of air and ground resonance in a tiltrotor and to determine whether the couplings can stabilize a soft-inplane hingeless tiltrotor. Work will completed on these tasks by the end of August, 2000. The dissertation will written and defended in Fall, 2000.

8 Appendices

8.1 Figures

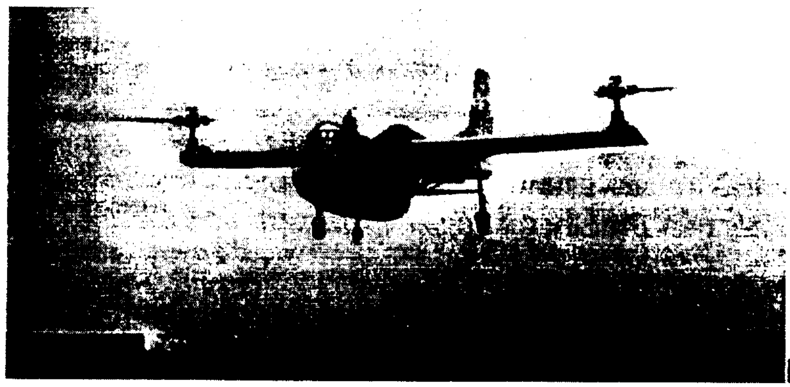

[16]

Fig. 1. Trancendental Model 1-G

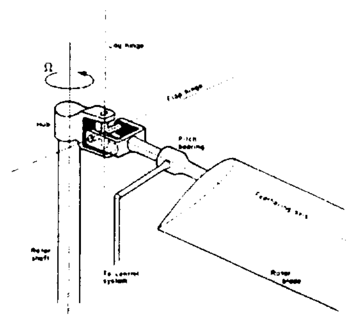

[18]

Fig. 2. Articulated Hub

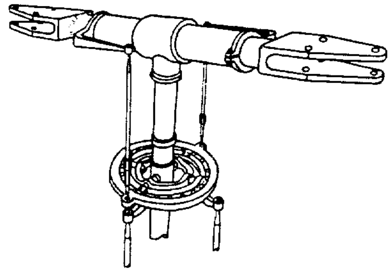

[15]

Fig. 3. Teetering Hub

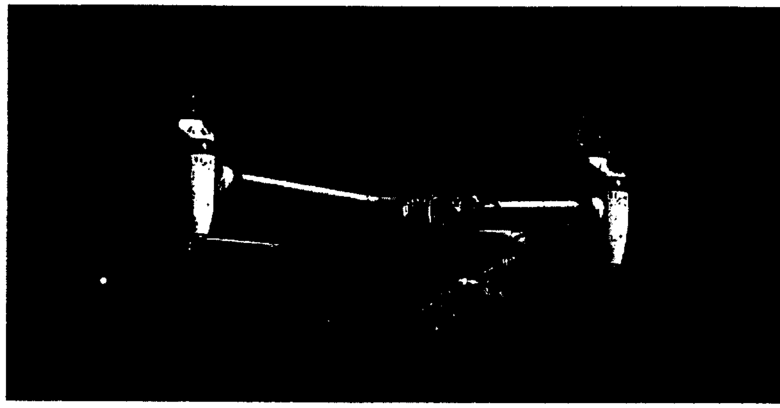

[32]

Fig. 4. XV-15 at NASA Dryden Research Center

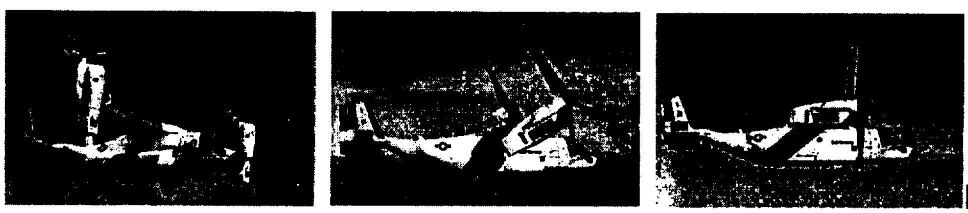

[4]

Fig. 5. V-22 in hover, conversion, and forward flight

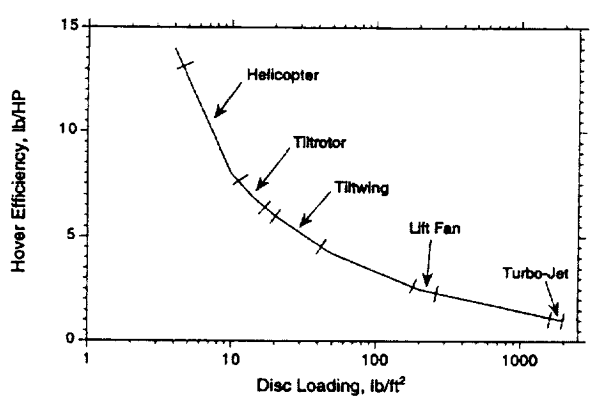

[46]

Fig. 6. Disk loading of V/STOL aircraft

[7]

Fig. 7. Kellet XR-2

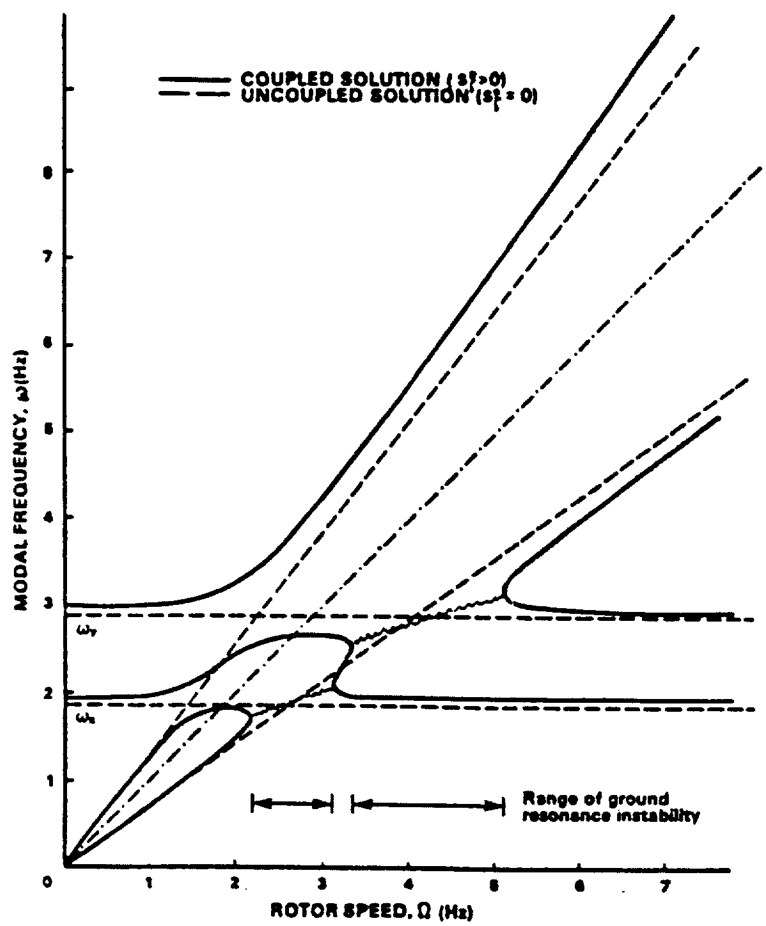

[8]

Fig. 8. Frequencies for ground resonance

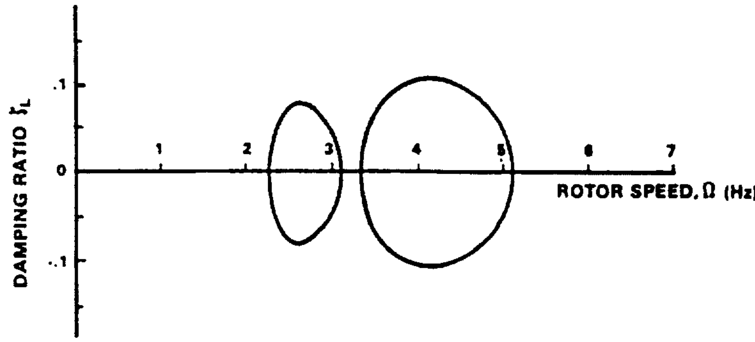

[8]

Fig. 9. Damping for ground resonance

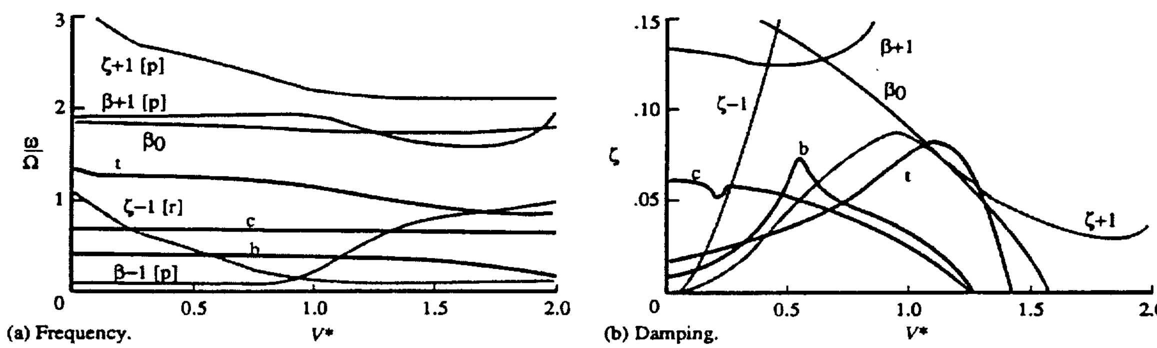

[35]

Fig. 10. Frequency and damping for whirl flutter stability

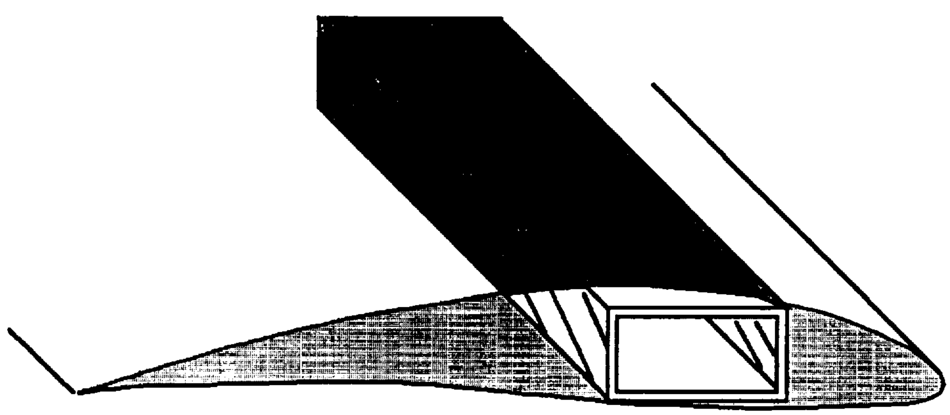

Fig. 11. Tailored wing or blade with box-beam spar

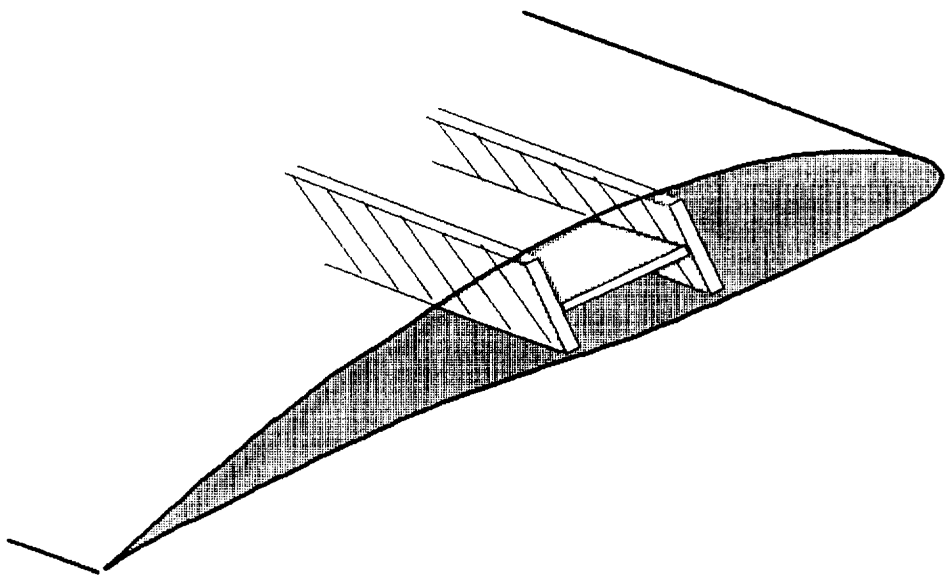

Fig. 12. Tailored flex-beam

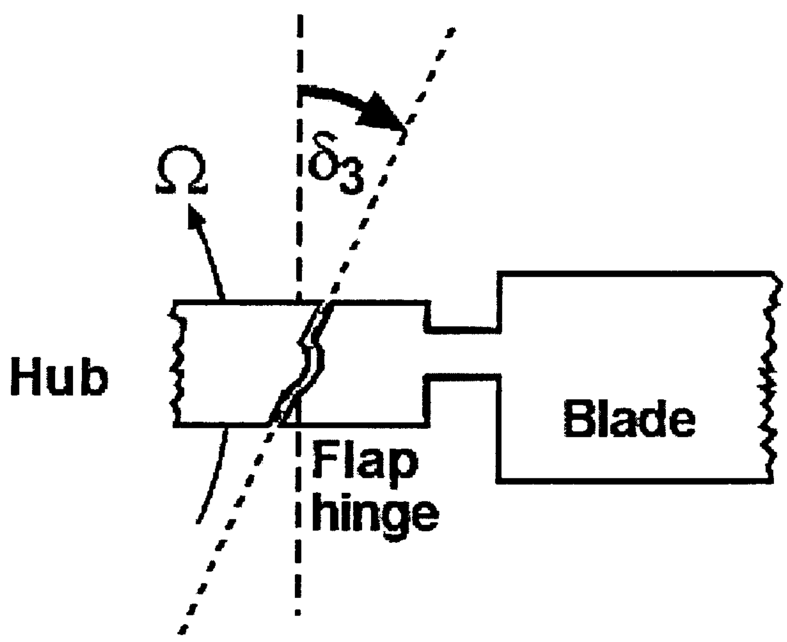

Fig. 13. Skewed flap hinge

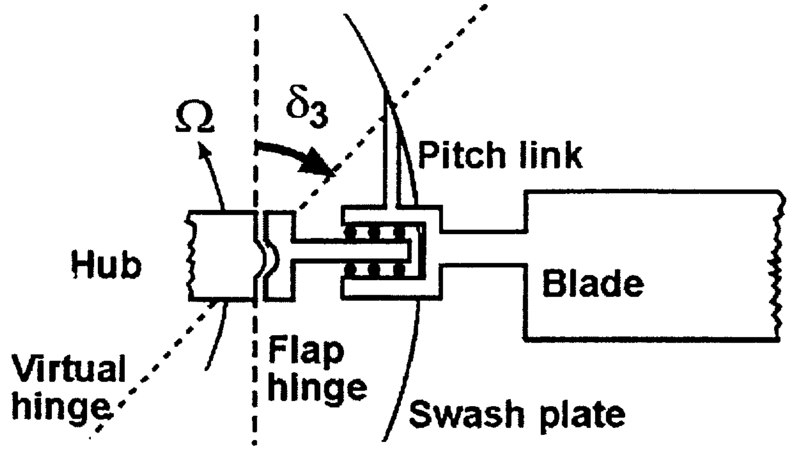

Fig. 14. δ_3 effect from outboard pitch-link

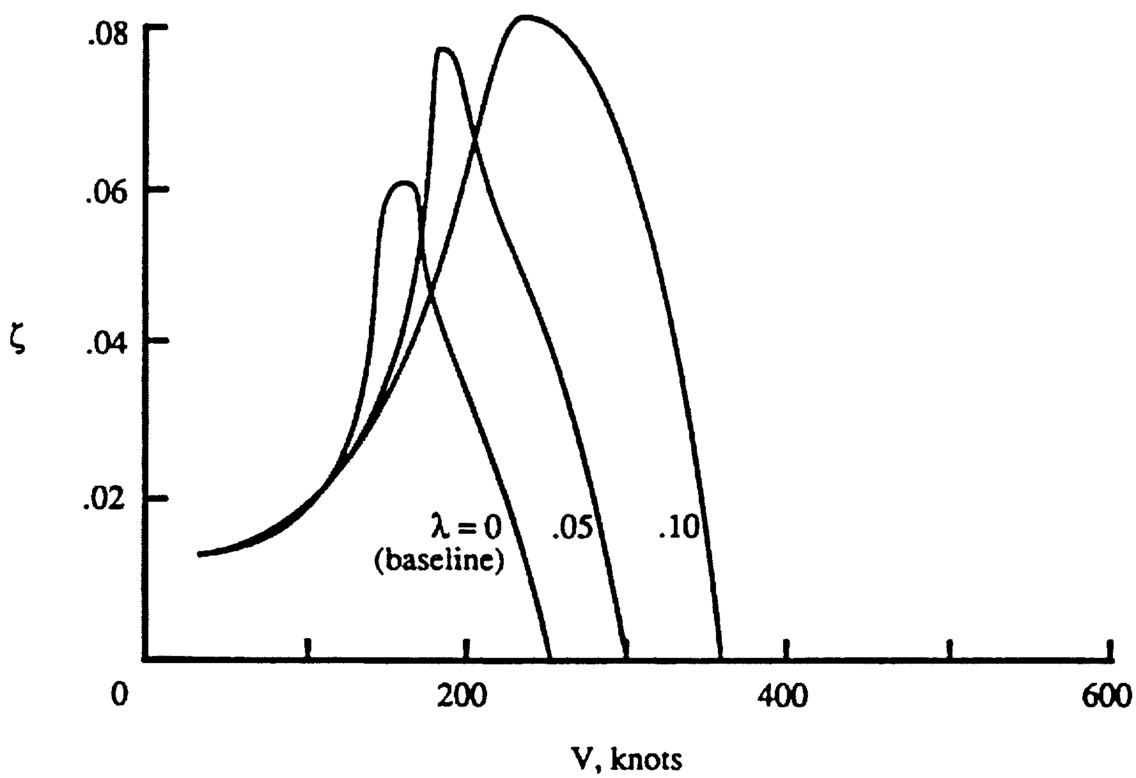

Fig. 15. Extension-twist coupling increases whirl flutter stability boundary

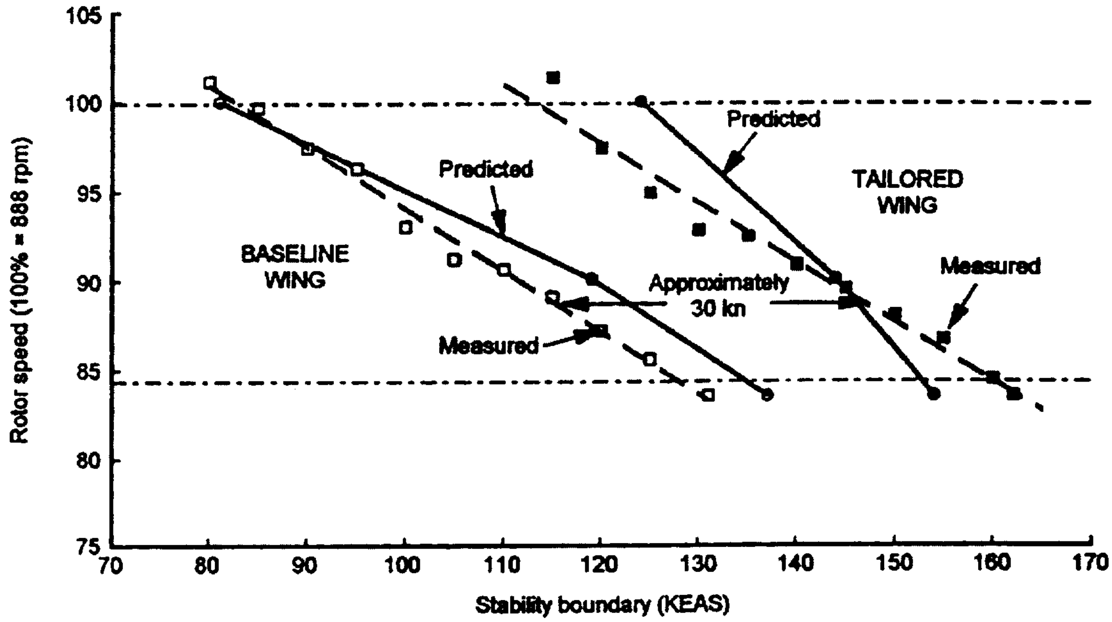

[10]

Fig. 16. Bending-twist coupled wing increases whirl flutter stability boundary

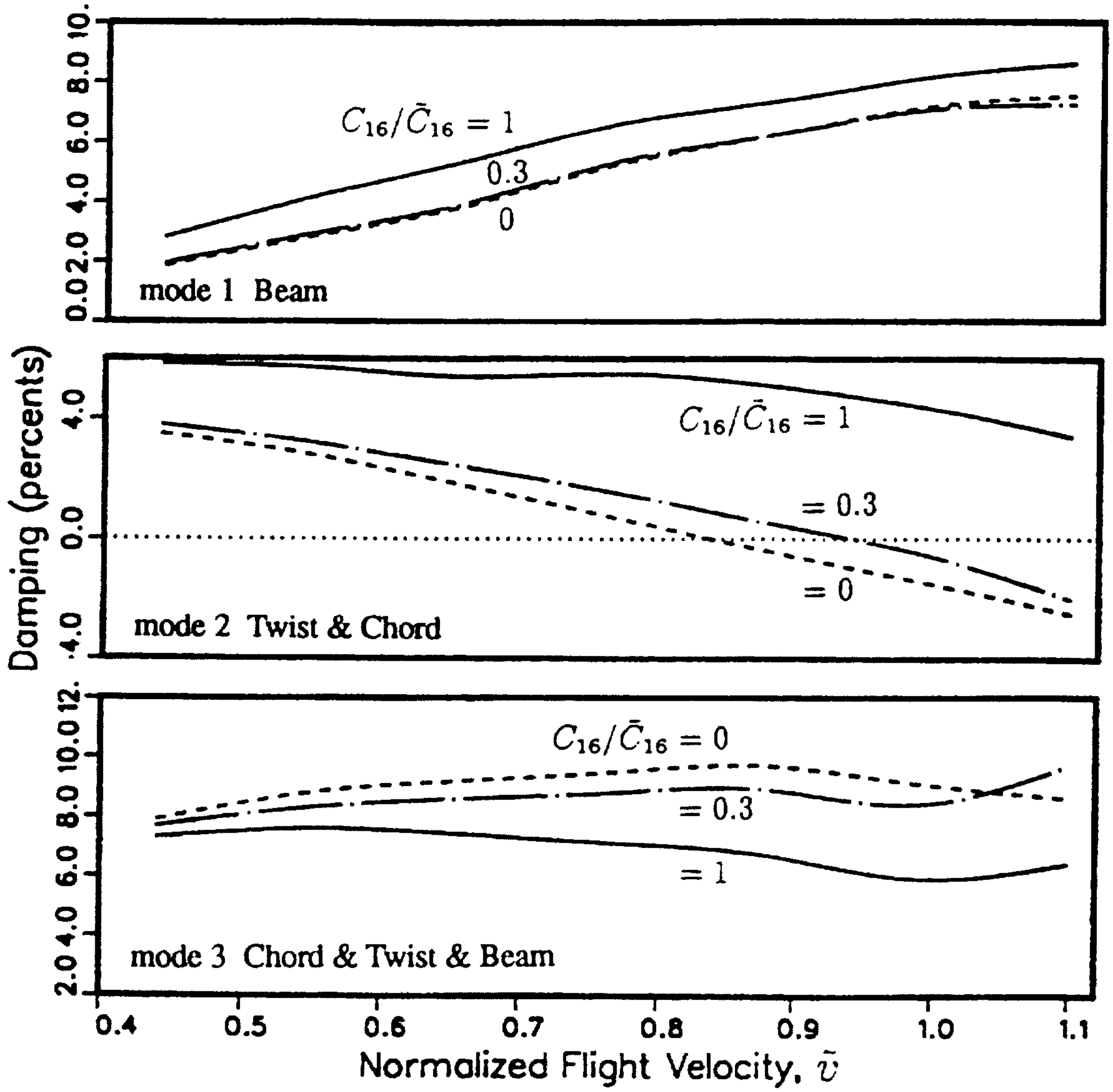

[1]

Fig. 17. Bending-twist coupled wing increases whirl flutter stability boundary

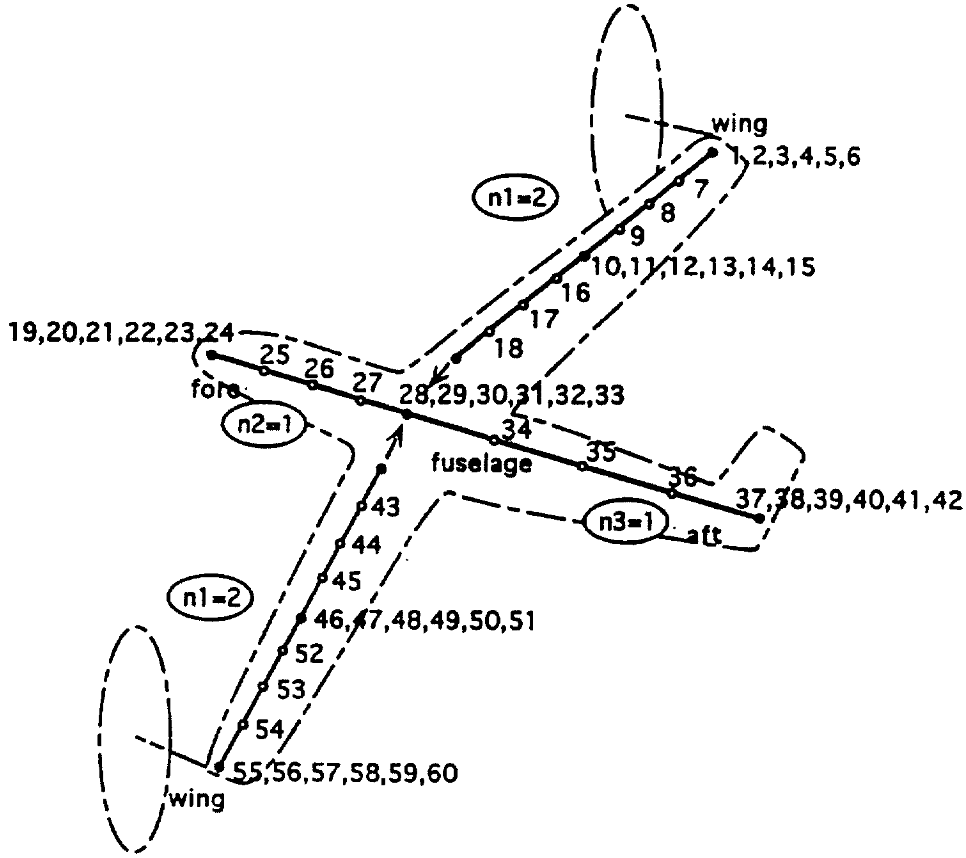

[46]

Fig. 18. Finite element method model for full-span tiltrotor

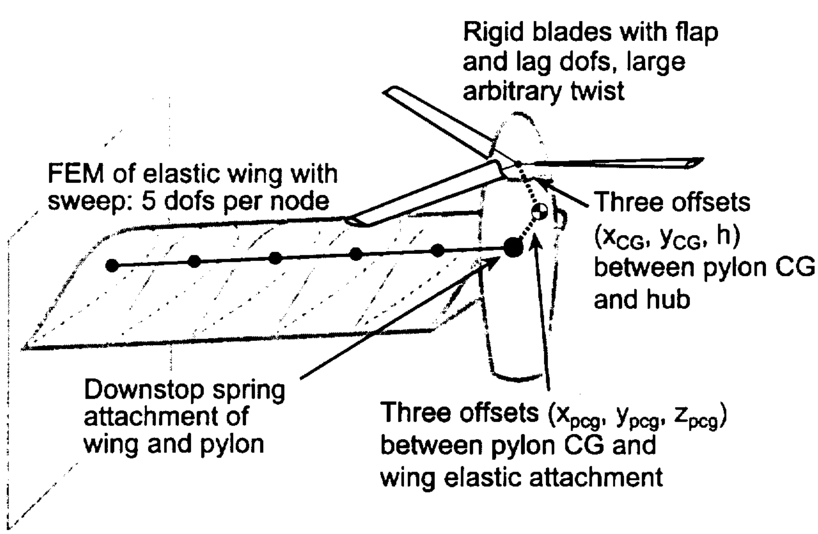

Fig. 19. Model Description

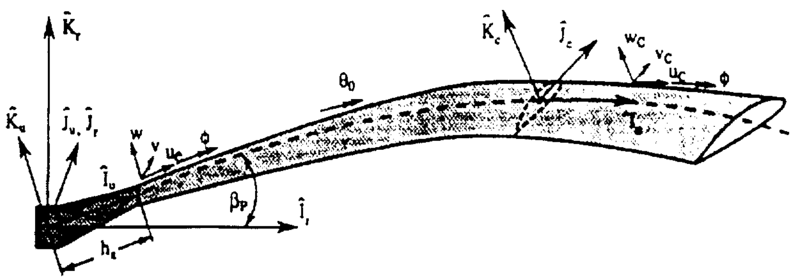

[35]

Fig. 20. Elastic Blade

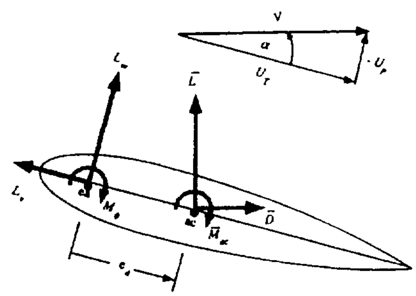

[44]

Fig. 21. Aerodynamic Forces in the Deformed Frame

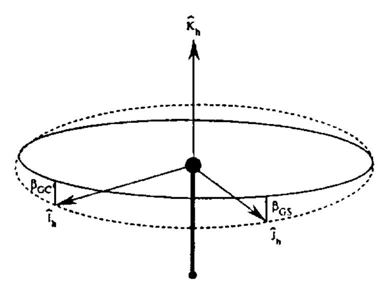

[35]

Fig.22. Gimbal Degrees of Freedom

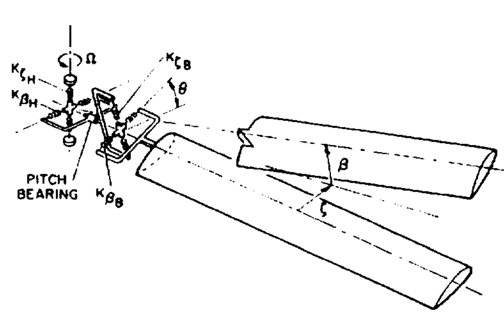

[2]

Fig. 23. Blade Structural Coupling Model

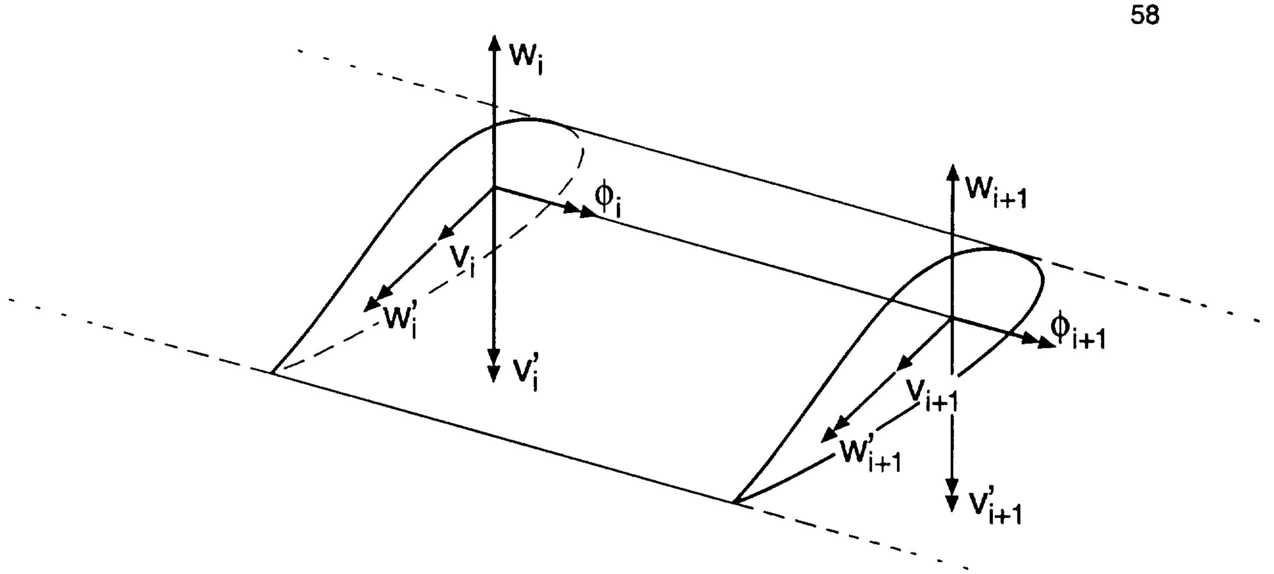

Fig. 24. Blade Finite Element

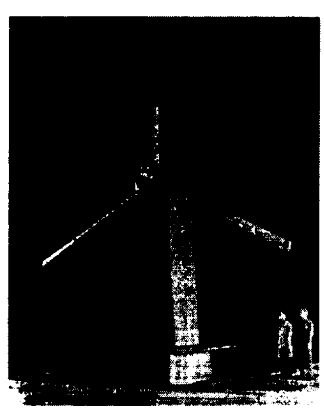
[22]

Fig. 25. Boeing Model 222 Wind Tunnel Model

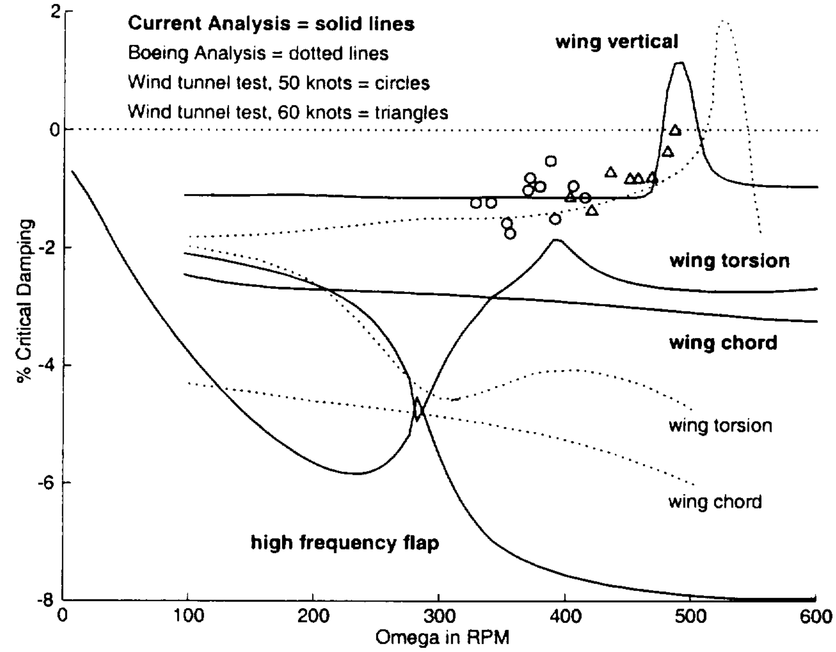

Fig. 26. Wing Damping, Boeing Model, 50 knots

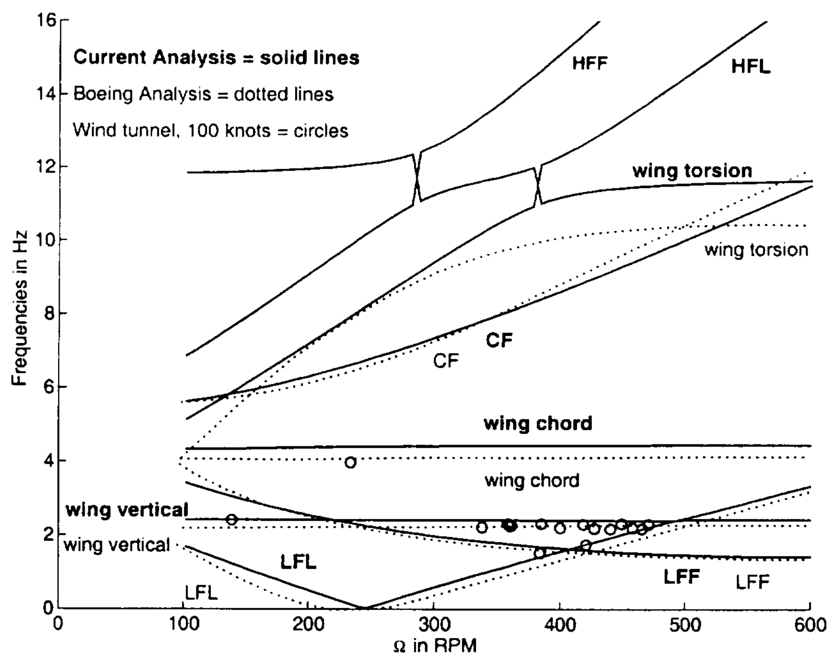

Fig. 27. Frequencies for Boeing Model, 100 knots

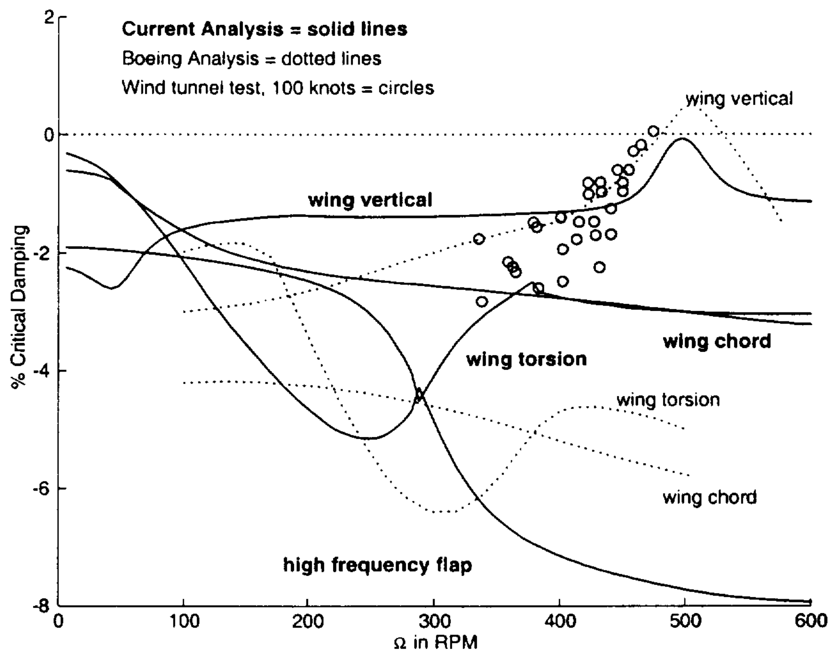

Fig. 28. Damping for Boeing Model, 100 knots

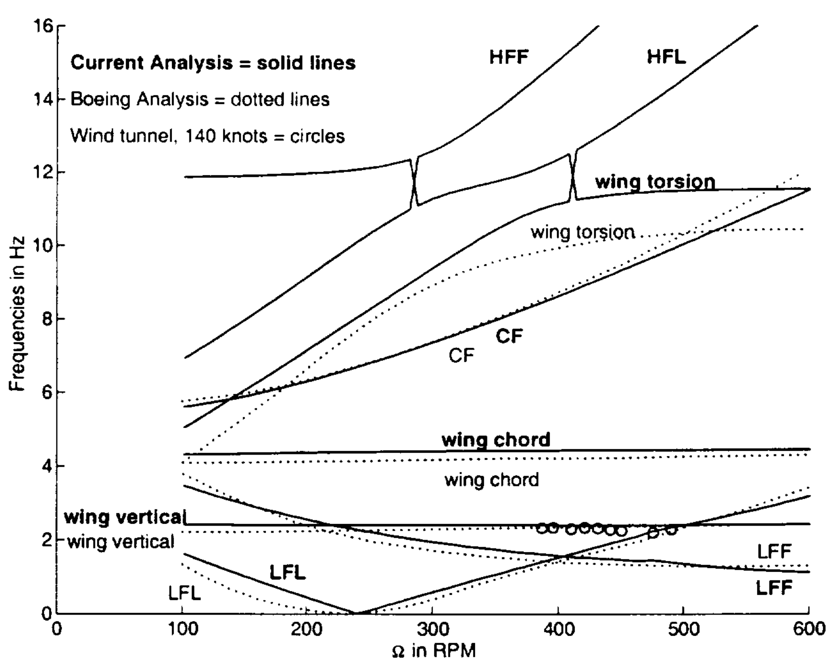

Fig. 29. Frequencies for Boeing Model, 100 knots

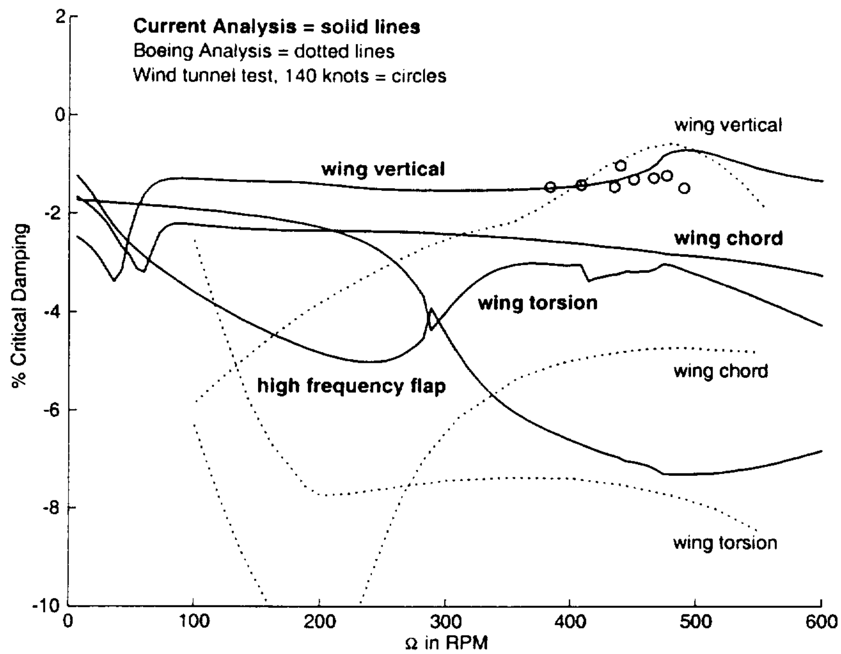

Fig. 30. Damping for Boeing Model, 100 knots

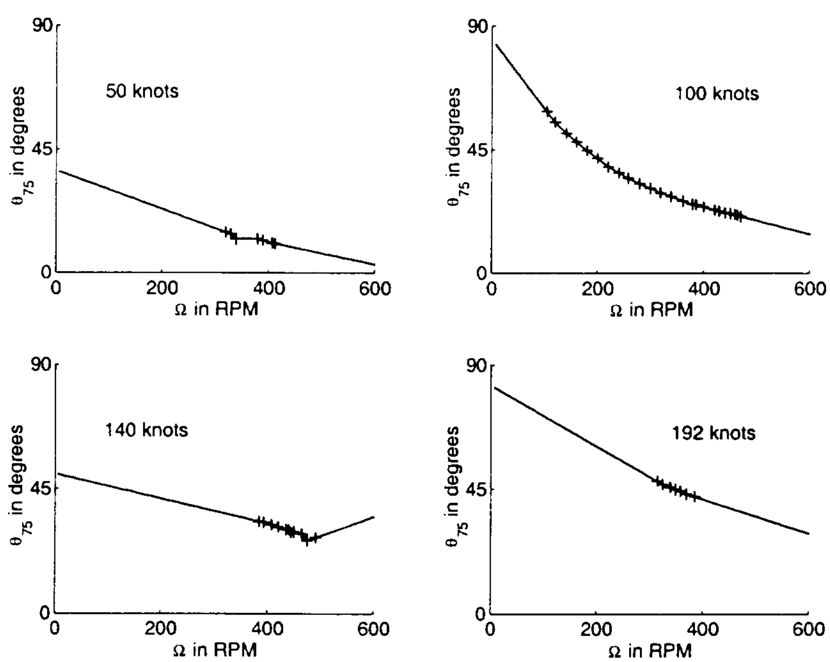

Fig. 31. Wind tunnel model pitch settings and interpolated values

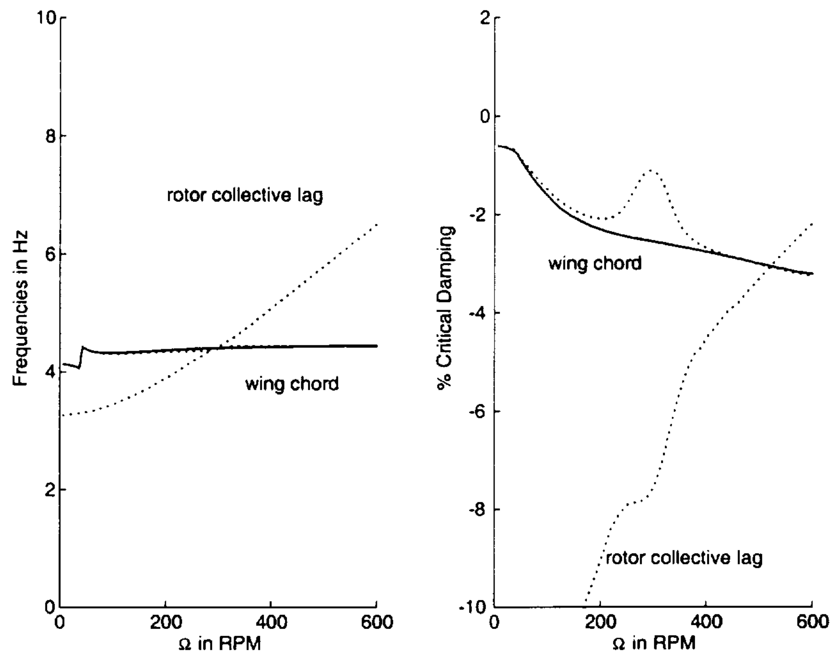

Fig. 32. Wing chord bending frequencies and damping with and without rotor collective lag

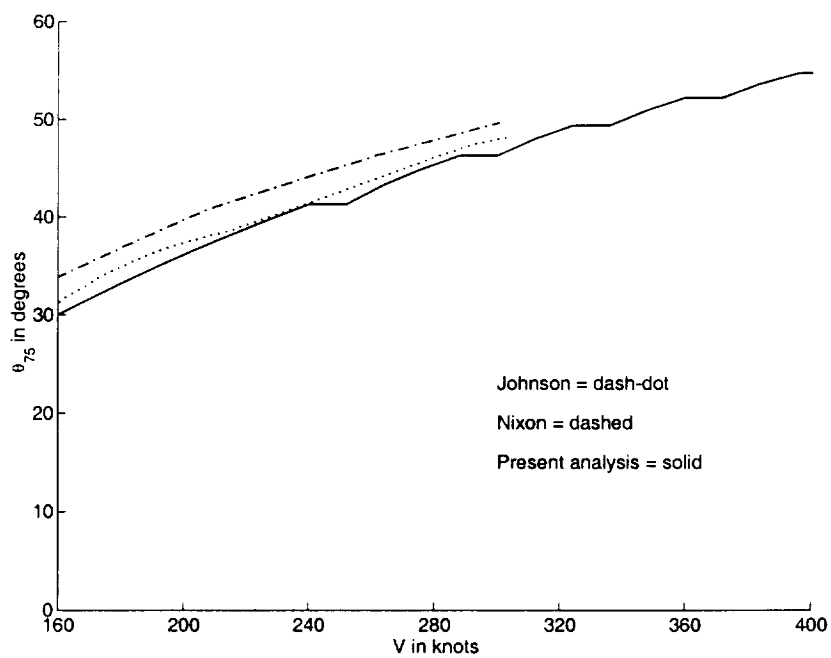

Fig. 33. θ_{75} as calculated by Johnson, Nixon, and the present analysis

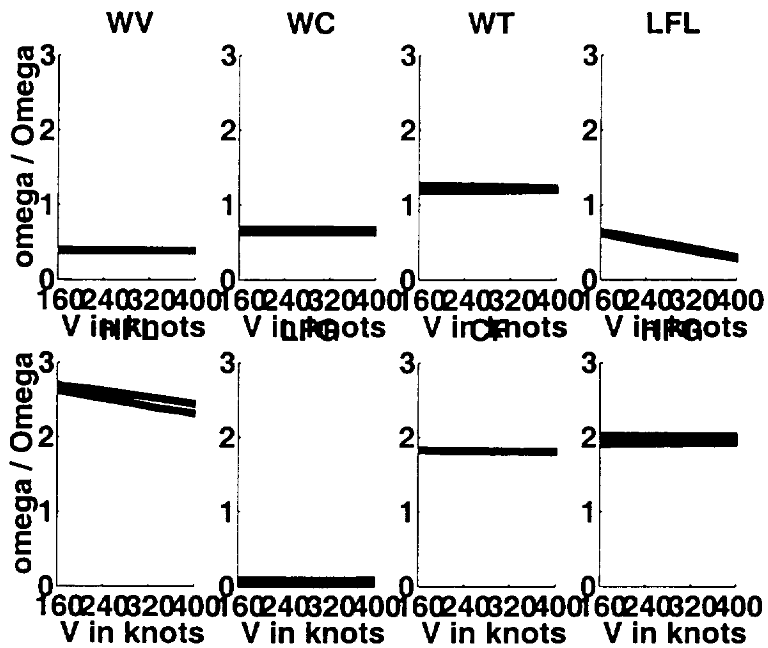

Fig. 34. Frequencies for whirl flutter from Nixon and current analysis

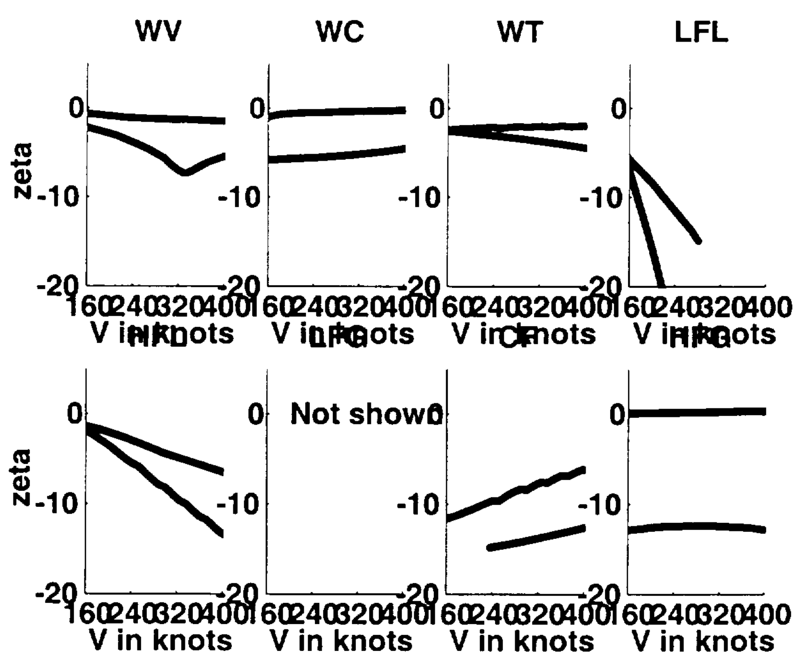

Fig. 35. Damping results for whirl flutter from Nixon and current analysis

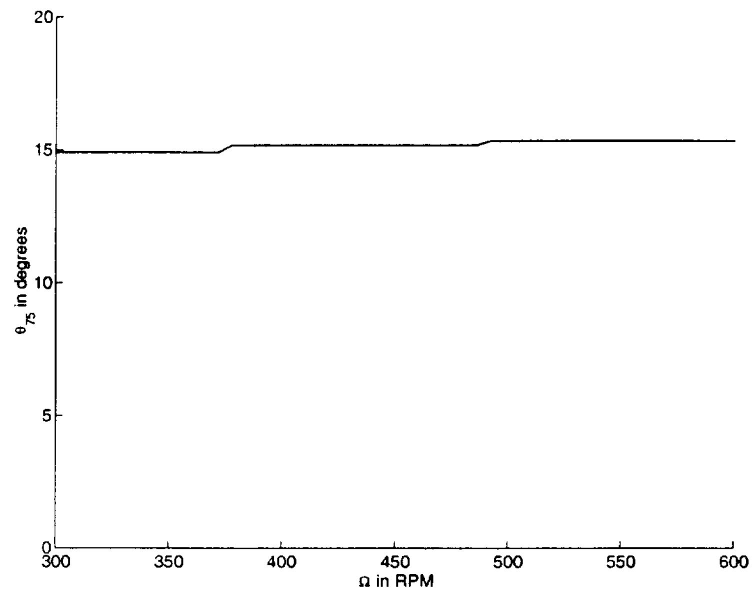

Fig. 36. θ_{75} for RPM sweep of Boeing Model 222 in hover, no couplings

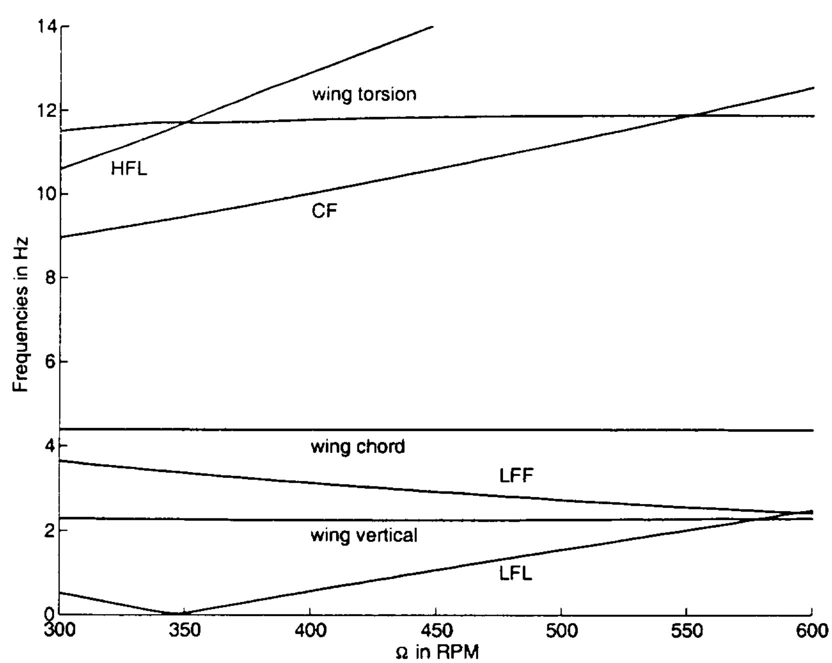

Fig. 37. Hover frequencies, Boeing model, no couplings

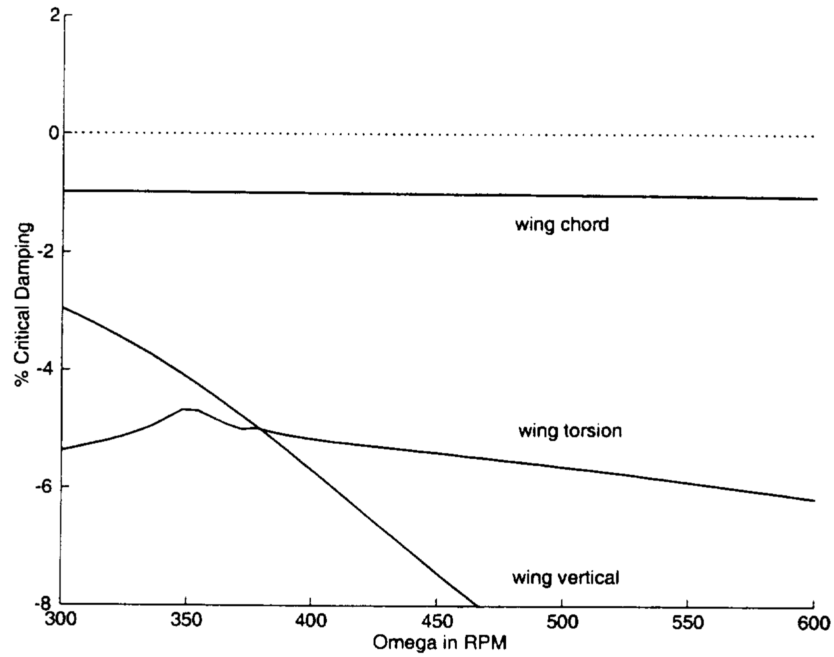

Fig. 38. Hover damping ratios, Boeing model, no couplings

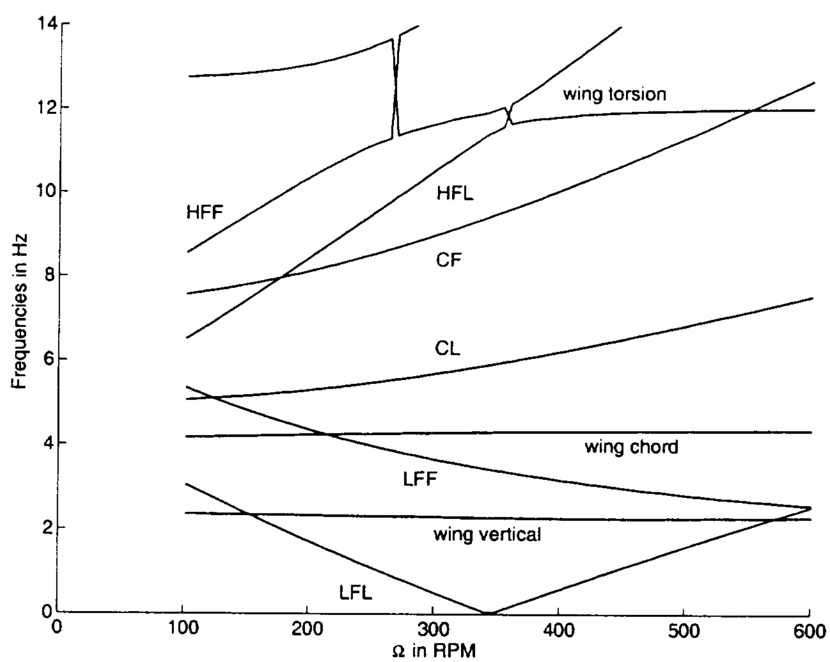

Fig. 39. Zero-thrust frequencies, Boeing model, no couplings

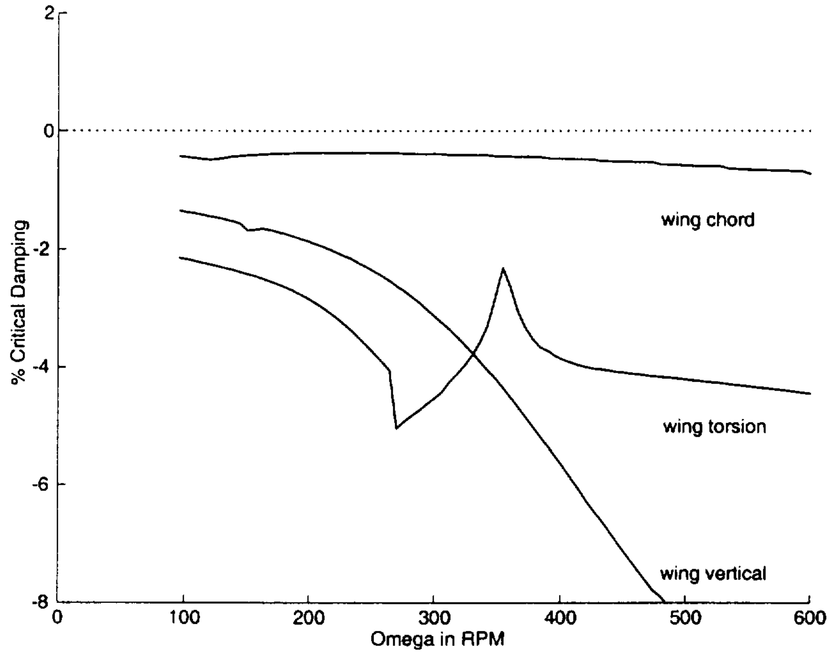

Fig. 40. Zero-thrust damping ratios, Boeing model, no couplings

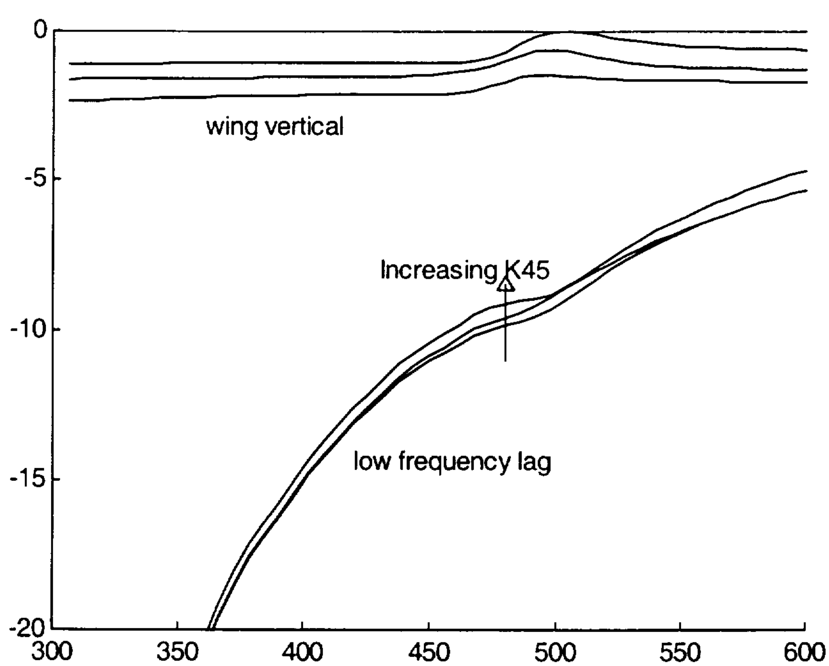

Fig. 41. Positive K_{45} coupling, 100 knots

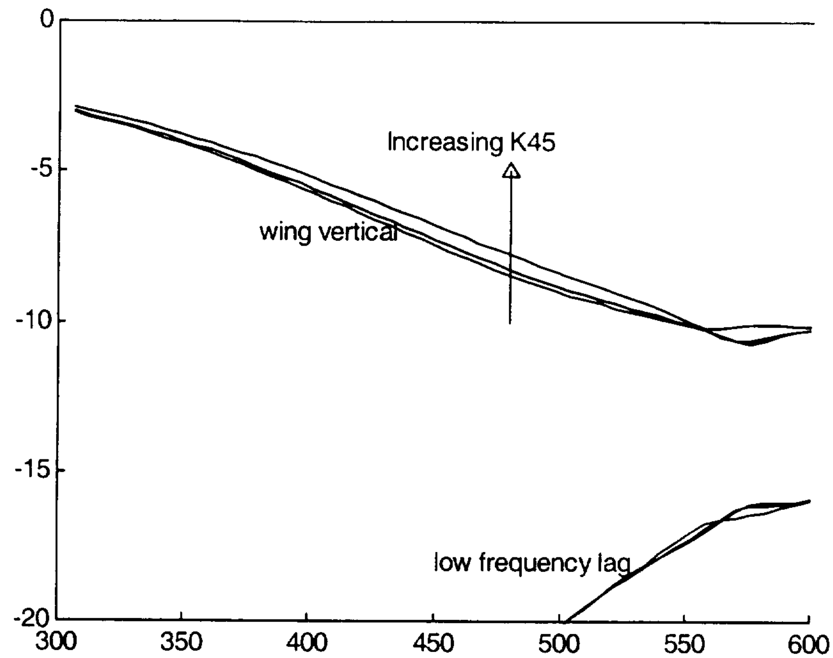

Fig. 42. Positive K_{45} coupling in hover

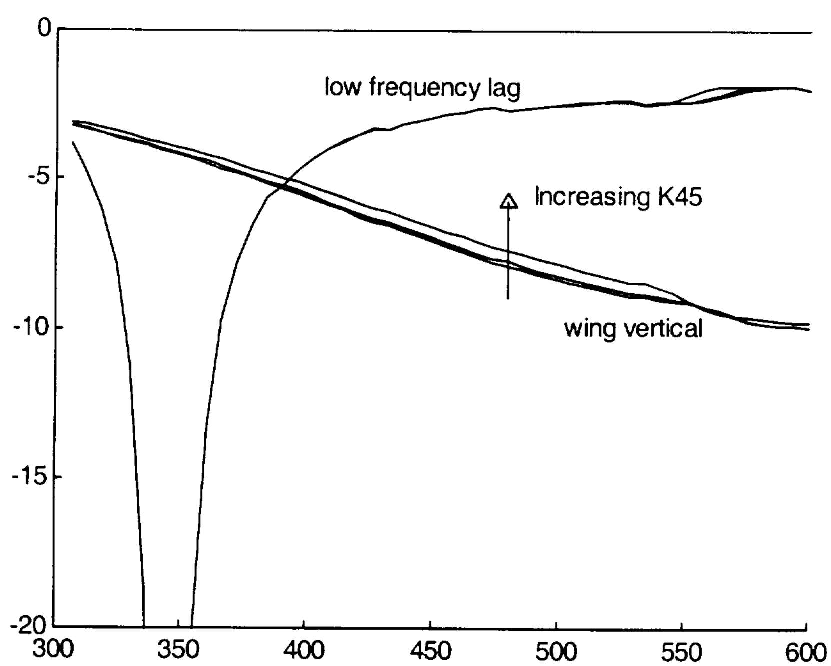

Fig. 43. Positive K_{45} coupling for zero thrust

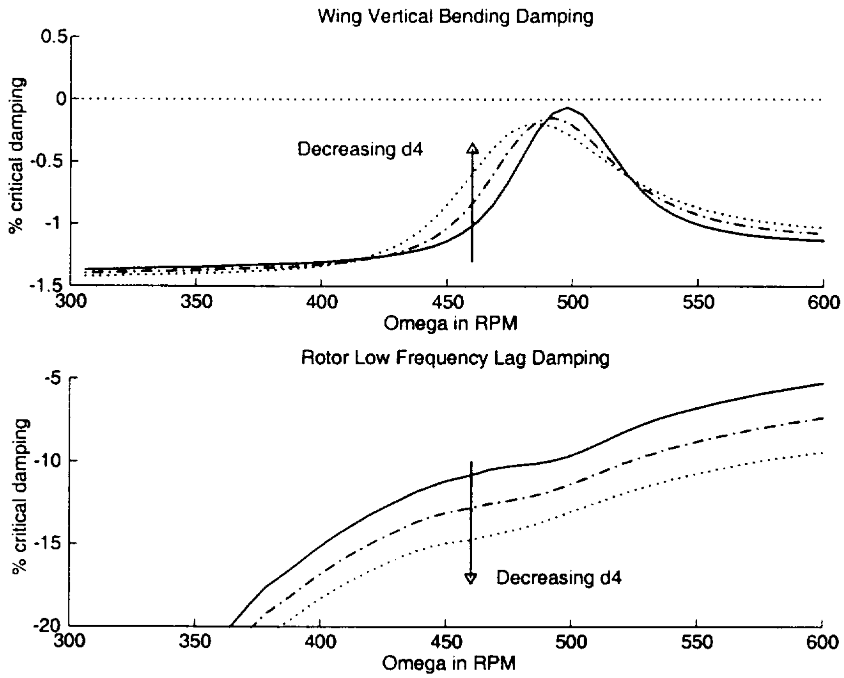

Fig. 44. Positive δ_4 coupling at 100 knots, baseline, $\delta_4 = -5$ degrees, and $\delta_4 = -10$ degrees

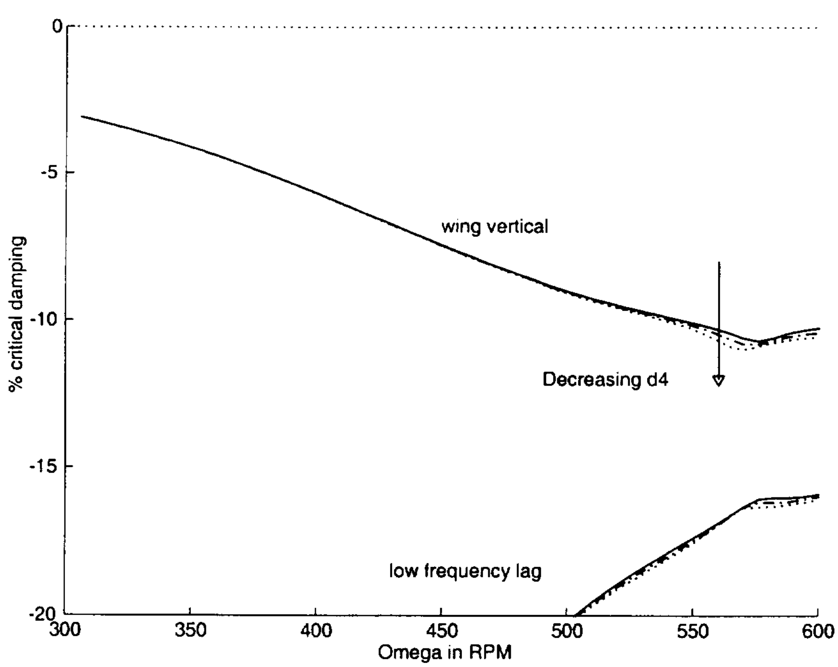

Fig. 45. Positive δ_4 coupling in hover, baseline, $\delta_4 = -5$ degrees, and $\delta_4 = -10$ degrees

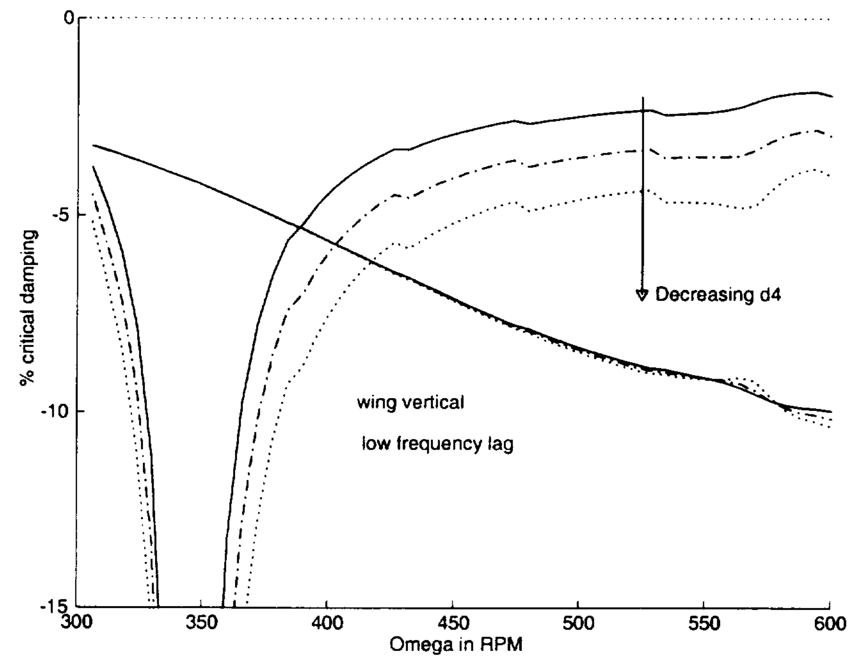

Fig. 46. Positive δ_4 coupling for zero thrust, baseline, $\delta_4 = -5$ degrees, and $\delta_4 = -10$ degrees

8.2 References

[1] Barkai, S.M. and O. Rand, *The Influence of Composite Induced Couplings on the Stability of Wing/Rotor Systems*. Journal of the American Helicopter Society, 1998. 43(2): p. 133-145.
[2] Bielawa, R.L., *Rotary Wing Structural Dynamics and Aeroelasticity*. AIAA Education Series, ed. J.S. Przemieniecki. 1992, Washington, DC: American Institute of Aeronautics and Astronautics, Inc. 562.
[3] Bir, G., et al., *UMARC Theory Manual*. 1993, University of Maryland: College Park, Maryland.
[4] Boeing Company, *V-22 Osprey*. 1995: Seattle, Washington.
[5] Bousman, W.G., *An Experimental Investigation of the Effects of Aeroelastic Couplings on Aeromechanical Stability of a Hingeless Rotor Helicopter*. Journal of the American Helicopter Society, 1981: p. 46-53.
[6] Burkam, J.E. and W.L. Miao, *Exploration of Aeroelastic Stability Boundaries with a Soft-in-Plane Hingeless-Rotor Model*. Journal of the American Helicopter Society, 1972. 17(4).
[7] Carlson, R.M., *Ground Resonance Characterization and Control*, in *From da Vinci to Today and Beyond: The Top Technology Achievements in Vertical Flight History*, M.E.R. Flater, Editor. 1994, The American Helicopter Society: Washington, DC. p. 15-16.
[8] Chopra, I., *Rotorcraft Dynamics Course Notes*. 1990.
[9] Coleman, R.P. and A.M. Feingold, *Theory of Self-Excited Mechanical Oscillations of Helicopter Rotors with Hinged Blades*. 1958, National Advisory Committee for Aeronautics (NACA): Washington, DC.
[10] Corso, L.M., D.A. Popelka, and M.W. Nixon. *Design, Analysis, and Test of a Composite Tailored Tiltrotor Wing*. in *The 53rd Annual National Forum of the American Helicopter Society*. 1997. Virginia Beach, Virginia.
[11] Esculier, J., et al. *Preliminary Comparisons of Tilt Rotor and Compound Helicopter for Civil Applications*. in *The 46th Annual National Forum and Technology Display of the American Helicopter Society*. 1989. Boston, Massachusetts.
[12] Friedmann, P.P. and C. Venkatesan, *Influence of Unsteady Aerodynamic Models on Aeromechanical Stability in Ground Resonance*. Journal of the American Helicopter Society, 1986: p. 65-74.
[13] Gaffey, T.M., *The Effect of Positive Pitch-flap Coupling (Negative δ-3) on Rotor Blade Motion Stability and Flapping*. Journal of the American Helicopter Society, 1969: p. 49-67.
[14] Gandhi, F. and E. Hathaway, *Optimized Aeroelastic Couplings for Alleviation of Helicopter Ground Resonance*. Journal of Aircraft, 1998. 35(4): p. 582-590.
[15] Gessow, A. and J. Garry C. Myers, *Aerodynamics of the Helicopter*. 1952, College Park, MD: College Park Press. 343.
[16] Harris, F.D., *High Speed V/STOL's*, in *From da Vinci to Today and Beyond: The Top Technology Achievements in Vertical Flight History*, M.E.R. Flater, Editor. 1994, The American Helicopter Society: Washington, DC. p. 34-35.
[17] Johnson, W., *Analytical Model for Tilting Proprotor Aircraft Dynamics, Including Blade Torsion and Coupled Bending Modes, and Conversion Mode Operation*. 1974, NASA Ames Research Center: Moffett Field, California. p. 1-160.
[18] Johnson, W., *Helicopter Theory*. 1980, New York, NY: Dover Publications, Inc. 1089.
[19] Johnson, W., *Influence of Unsteady Aerodynamics on Hingeless Rotor Ground Resonance*. Journal of Aircraft, 1982. 19(8).
[20] Kvaternik, R.G., *Studies in Tilt-Rotor VTOL Aircraft Aeroelasticity*, in *Solid Mechanics, Structures, and Mechanical Design*. 1973, Case Western Reserve University. p. 659.
[21] Kvaternik, R.G. *Experimental and Analytical Studies in Tilt-Rotor Aeroelasticity*. in

AHS/NASA Ames Specialists' Meeting on Rotorcraft Dynamics. 1974.
[22] Kvaternik, R.G., *A Review of Some Tilt-Rotor Aeroelastic Research at NASA-Langley*. Journal of Aircraft, 1976. 13(5): p. 357-363.
[23] Kvaternik, R.G. *A Historical Perspective of Proprotor Aeroelastic Research at Langley Research Center*. in *Fourth Workshop on Dynamics and Aeroelastic Stability Modeling of Rotorcraft Systems*. 1991. College Park, Maryland.
[24] Kvaternik, R.G., *A Historical Overview of the Tiltrotor Aeroelastic Research at Langley Research Center*. 1992, NASA Langley Research Center: Hampton, Virginia.
[25] Lytwyn, R.T., W. Miao, and W. Woitsch. *Airborne and Ground Resonance of Hingeless Rotors*. in *The 26th Annual National Forum of the American Helicopter Society*. 1970. Washington, D.C.
[26] Magee, J.P., et al., *Wind Tunnel Tests of a Full Scale Hingeless Prop/Rotor Designed for the Boeing Model 222 Tilt Rotor Aircraft*. 1973, the Boeing Company, Vertol Division: Philadelphia, PA.
[27] Martin, S., Jr., A.H. Schoen, and R. Vehorn, Cdr, USN. *V-22 Development*. in *The 43rd Annual National Forum of the American Helicopter Society*. 1987. St. Louis, Missouri.
[28] McCormick, B.W., *Aerodynamics, Aeronautics, and Flight Mechanics*. 2nd ed. 1995, New York: John Wiley & Sons, Inc.
[29] McHugh, F.J., et al., *Performance and Stability Test of a 1/4.622 Froude Scaled Boeing Vertol Model 222 Tilt Rotor Aircraft*. 1973, the Boeing Company: Philadelphia.
[30] Milgram, J.H. and I. Chopra, *Air Resonance of Hingeless Rotor Helicopters in Trimmed Forward Flight*. Journal of the American Helicopter Society, 1994. 39(4): p. 46-58.
[31] Nagabhushanam, J. and G.H. Gaonkar, *Rotorcraft Air Resonance in Forward Flight with Various Dynamic Inflow Models and Aeroelastic Couplings*. Vertica, 1984. 8(4).
[32] NASA Dryden Research Center, Dryden Research Aircraft: Photo Server. 1980: Edwards, California.
[33] Nixon, M.W. *Extension-Twist Coupling of Composite Circular Tubes with Application to Tilt Rotor Blade Design*. in *The 28th Structures, Structural Dynamics, and Materials Conference*. 1987. Monterey, California.
[34] Nixon, M.W., *Parametric Studies for Tiltrotor Aeroelastic Stability in High-speed Flight*. Journal of the American Helicopter Society, 1993. 38(4): p. 71-79.
[35] Nixon, M.W., *Aeroelastic Response and Stability of Tiltrotors with Elastically-Coupled Composite Rotor Blades*, in *Aerospace Engineering*. 1993, University of Maryland: College Park, Maryland. p. 424.
[36] Ormiston, R.A. *Aeromechanical Stability of Soft Inplane Hingeless Rotor Helicopters*. in *Third European Rotorcraft and Powered Lift Aircraft Forum*. 1977. Aix-en-Provence, France.
[37] Ormiston, R.A., *Rotor-Fuselage Dynamics of Helicopter Air and Ground Resonance*. Journal of the American Helicopter Society, 1991: p. 3-20.
[38] Panda, B. and E. Mychalowycz. *Aeroelastic Stability Wind Tunnel Testing with Analytical Correlation of the Comanche Bearingless Main Rotor*. in *The 52nd Annual National Forum and Technology Display of the American Helicopter Society*. 1996. Washington, DC.
[39] Popelka, D., et al. *Results of an Aeroelastic Tailoring Study for a Composite Tiltrotor Wing*. in *The 51st Annual National Forum of the American Helicopter Society*. 1995. Forth Worth, Texas.
[40] Rand, O., et al. *Modeling and Analysis of Tilt-Rotor Aeromechanical Phenomena*. in *The American Helicopter Society Aeromechanics Specialists Conference*. 1995. Fairfield County, Connecticut.

[41] Rand, O. and S. Barkai. *Analytic Insight into the Structural Couplings and Nonlinear Formulation of Solid and Thin-Walled Composite Blades*. in *The 52nd Annual National Forum and Technology Display of the American Helicopter Society*. 1996. Washington, DC.

[42] Reed, W.H., III, *Propeller-Rotor Whirl Flutter: A State-of-the-art Review*. Journal of Sound and Vibration, 1966. 4(3): p. 526-544.

[43] Scanlan, R.H. and J.C. Truman, *The Gyroscopic Effect of a Rigid Rotating Propeller on Engine and Wing Vibration Modes*. Journal of the Aeronautical Sciences, 1950. 17(October, 1950): p. 653-659, 666.

[44] Smith, E.C., *Aeroelastic Response and Aeromechanical Stability of Helicopters with Elastically Coupled Composite Rotor Blades*, in *Aerospace Engineering*. 1992, University of Maryland: College Park, Maryland. p. 414.

[45] Smith, E.C. and I. Chopra, *Air and Ground Resonance of Helicopters with Elastically Tailored Composite Rotor Blades*. Journal of the American Helicopter Society, 1993. 38(4): p. 50-61.

[46] Srinivas, V., *Aeroelastic Analysis of Advanced Tiltrotor Aircraft*, in *Aerospace Engineering*. 1995, University of Maryland: College Park, Maryland. p. 411.

[47] Taylor, E.S. and K.A. Browne, *Vibration Isolation of Aircraft Power Plants*. Journal of the Aeronautical Sciences, 1938. 6(December 1938): p. 43-49.

[48] Wilkerson, J.B. and R.S. Taylor. *Civil Tiltrotor Aircraft: A Comparison of Five Candidate Designs*. in *The 44th Annual National Forum of the American Helicopter Society*. 1988. Washington, D.C.

8.3 Ordering Scheme

Throughout the formulation of the equations of motion as described above, an ordering scheme was applied to reduce the number of terms in the equations. The orders of the various variables are as shown here. The largest terms in the equations of motion were of order ε. It was decided to retain all terms of orders ε, $\varepsilon^{\frac{3}{2}}$, ε^2, and $\varepsilon^{\frac{5}{2}}$ and only linear terms of order ε^3. This convention is applied throughout the derivation of the blade and hub matrices. Note that terms such as $\delta\beta$ refer to the perturbational quantities rather than the variational quantities.

Order 1	$a,\ \cos\psi,\ \cos\theta_0,\ \gamma,\ h,\ I_b,\ I_\beta,\ I_\zeta,\ k_{\alpha_s}, k_\beta, k_{\phi_s}, k_x, k_y, k_z, k_\zeta,$ $\lambda, \mu, \nu_\beta, \nu_\zeta, S_\beta, \sin\psi, \sin\theta_0, S_x, S_\zeta, \dot\theta_0, \ddot\theta_0, x, x_1$ $\tan\delta_3, \tan\delta_4, \tan\delta_5$ $\beta, \dot\beta, \ddot\beta, \delta\beta, \delta\dot\beta, \delta\ddot\beta, \zeta, \dot\zeta, \ddot\zeta, \delta\zeta, \delta\dot\zeta, \delta\ddot\zeta, \delta x_F, \delta y_F, \delta z_F,$ $\phi_s, \delta\phi_s, \alpha_s, \delta\alpha_s, \psi_s, \delta\psi_s, \beta_{GC}, \beta_{GS},$
Order ε	$\sin\phi, \cos\phi, \phi, \dot\phi, \ddot\phi, \phi', \dot\phi', \ddot\phi',$ $v_b, \dot v_b, \ddot v_b, v_b', \dot v_b', \ddot v_b', w_b, \dot w_b, \ddot w_b, w_b', \dot w_b', \ddot w_b',$ $y_1, \dot y_1, z_1, \dot z_1$ $\beta_p, \frac{c_0}{a}, \frac{d_2}{a}, c, \eta_r, \eta_{cs}, \zeta_{cs}, k_{m_1}, k_{m_2}$ $\dot\phi_s, \ddot\phi_s, \delta\dot\phi_s, \delta\ddot\phi_s, \dot\alpha_s, \ddot\alpha_s, \delta\dot\alpha_s, \delta\ddot\alpha_s, \dot\psi_s, \ddot\psi_s, \delta\dot\psi_s, \delta\ddot\psi_s,$
Order $\varepsilon^{\frac{3}{2}}$	$\dot x_F, \ddot x_F, \delta\dot x_F, \delta\ddot x_F, \dot y_F, \ddot y_F, \delta\dot y_F, \delta\ddot y_F, \dot z_F, \ddot z_F, \delta\dot z_F, \delta\ddot z_F,$ e_g $\frac{c_d}{a}, u, \dot u, \ddot u, u_e, \dot u_e, \ddot u_e, \dot x_1,$
Order ε^2	$\iint_A v_b' v_b'\, d\eta\, d\zeta, \iint_A v_b' \dot v_b'\, d\eta\, d\zeta, \iint_A \dot v_b' \dot v_b'\, d\eta\, d\zeta, \iint_A v_b' \ddot v_b'\, d\eta\, d\zeta,$ $\iint_A w_b' w_b'\, d\eta\, d\zeta, \iint_A w_b' \dot w_b'\, d\eta\, d\zeta, \iint_A \dot w_b' \dot w_b'\, d\eta\, d\zeta, \iint_A w_b' \ddot w_b'\, d\eta\, d\zeta$

8.4 Coordinate Systems

Inertial	$\left\{\begin{array}{c}\hat{I}_i\\ \hat{J}_i\\ \hat{K}_i\end{array}\right\}$	centered at wing ea (undef)	$=\left\{\begin{array}{c}\hat{I}_I^{Ground}\\ \hat{J}_I^{Ground}\\ \hat{K}_I^{Ground}\end{array}\right\}$	translation by steady vehicle motion	rotation by $(0,0,0)$
Body	$\left\{\begin{array}{c}\hat{I}_b\\ \hat{J}_b\\ \hat{K}_b\end{array}\right\}$	centered at wing ea (undef)	$=[T_\Lambda]\left\{\begin{array}{c}\hat{I}_i\\ \hat{J}_i\\ \hat{K}_i\end{array}\right\}$	translation by $(0,0,0)$	rotation by $(0,0,\Lambda)$
Wing	$\left\{\begin{array}{c}\hat{I}_w\\ \hat{J}_w\\ \hat{K}_w\end{array}\right\}$	centered at wing ea (deformed)	$=[T_{wi}]\left\{\begin{array}{c}\hat{I}_i\\ \hat{J}_i\\ \hat{K}_i\end{array}\right\}$	translation by (x_h,y_h,z_h)	rotation by $(-\phi_s,-\alpha_s,\psi_s)$
Pylon	$\left\{\begin{array}{c}\hat{I}_P\\ \hat{J}_P\\ \hat{K}_P\end{array}\right\}$	centered at pylon CG	$=[T_{hw}]\left\{\begin{array}{c}\hat{I}_w\\ \hat{J}_w\\ \hat{K}_w\end{array}\right\}$	offset by $(x_{pcg},y_{pcg},z_{pcg})$	rotation by $(0,\alpha_p,0)$
Hub	$\left\{\begin{array}{c}\hat{I}_h\\ \hat{J}_h\\ \hat{K}_h\end{array}\right\}$	centered at hub	$=\left\{\begin{array}{c}\hat{I}_P\\ \hat{J}_P\\ \hat{K}_P\end{array}\right\}$	offset by (x_{CG},y_{CG},h)	rotation by $(0,0,0)$
Rotating	$\left\{\begin{array}{c}\hat{I}_r\\ \hat{J}_r\\ \hat{K}_r\end{array}\right\}$	centered at hub	$=[T_{rh}]\left\{\begin{array}{c}\hat{I}_h\\ \hat{J}_h\\ \hat{K}_h\end{array}\right\}$	translation by $(0,0,0)$	rotation by $(0,0,\psi)$
Undeformed	$\left\{\begin{array}{c}\hat{I}_u\\ \hat{J}_u\\ \hat{K}_u\end{array}\right\}$	centered at hub	$=[T_{ur}]\left\{\begin{array}{c}\hat{I}_r\\ \hat{J}_r\\ \hat{K}_r\end{array}\right\}$	translation by $(0,0,0)$	rotation by $(0,-\beta_p+\beta_G,0)$
Cross-section	$\left\{\begin{array}{c}\hat{I}_c\\ \hat{J}_c\\ \hat{K}_c\end{array}\right\}$	centered at x along blade	$=[T_{cu}]\left\{\begin{array}{c}\hat{I}_u\\ \hat{J}_u\\ \hat{K}_u\end{array}\right\}$	translation by $(x,0,0)$	rotation by $(\theta_0,0,0)$
Deformed	$\left\{\begin{array}{c}\hat{I}_d\\ \hat{J}_d\\ \hat{K}_d\end{array}\right\}$	centered at x along blade	$=[T_{dc}]\left\{\begin{array}{c}\hat{I}_c\\ \hat{J}_c\\ \hat{K}_c\end{array}\right\}$	translation by (u,v_c,w_c)	rotation by (ϕ,w_c',v_c')

Note that the Body coordinate system as described above is also an inertial frame of reference. The transformation matrices as defined above are given as follows:

$$[T_\Lambda]=\begin{bmatrix}\cos\Lambda & \sin\Lambda & 0\\ -\sin\Lambda & \cos\Lambda & 0\\ 0 & 0 & 1\end{bmatrix}$$

$$[T_{wi}]=\begin{bmatrix}\cos\psi_s & \sin\psi_s & 0\\ -\sin\psi_s & \cos\psi_s & 0\\ 0 & 0 & 1\end{bmatrix}\begin{bmatrix}\cos\alpha_s & 0 & \sin\alpha_s\\ 0 & 1 & 0\\ -\sin\alpha_s & 0 & \cos\alpha_s\end{bmatrix}\begin{bmatrix}1 & 0 & 0\\ 0 & \cos\phi_s & -\sin\phi_s\\ 0 & \sin\phi_s & \cos\phi_s\end{bmatrix}$$

$$[T_{hw}]=\begin{bmatrix}\cos\alpha_p & 0 & -\sin\alpha_p\\ 0 & 1 & 0\\ \sin\alpha_p & 0 & \cos\alpha_p\end{bmatrix}$$

$$[T_{rh}]=\begin{bmatrix}\cos\psi & \sin\psi & 0\\ -\sin\psi & \cos\psi & 0\\ 0 & 0 & 1\end{bmatrix}$$

$$[T_{ur}] = \begin{bmatrix} \cos\beta_p & 0 & \sin\beta_p \\ 0 & 1 & 0 \\ -\sin\beta_p & 0 & \cos\beta_p \end{bmatrix}$$

$$[T_{cu}] = \begin{bmatrix} 1 & 0 & 0 \\ 0 & \cos\theta_0 & \sin\theta_0 \\ 0 & -\sin\theta_0 & \cos\theta_0 \end{bmatrix}$$

$$[T_{dc}] = \begin{bmatrix} 1 - \frac{1}{2}w_b'^2 - \frac{1}{2}v_b'^2 & w_b'\sin\theta_0 + v_b'\cos\theta_0 & -v_b'\sin\theta_0 + w_b'\cos\theta_0 \\ \begin{array}{l}(-w_b'\cos\phi + v_b'\sin\phi)\sin\theta_0 \\ -(v_b'\cos\phi + w_b'\sin\phi)\cos\theta_0\end{array} & \cos\phi & \sin\phi \\ \begin{array}{l}(v_b'\cos\phi + w_b'\sin\phi)\sin\theta_0 \\ +(-w_b'\cos\phi + v_b'\sin\phi)\cos\theta_0\end{array} & -\sin\phi & \cos\phi \end{bmatrix}$$

With the gimbal motion included, the matrix $[T_{ur}]$ as given above is modified to be

$$[T_{ur}] = \begin{bmatrix} \cos\beta_p + \sin\beta_p(\beta_{GC}\cos\psi + \beta_{GS}\sin\psi) & 0 & -\cos\beta_p(\beta_{GC}\cos\psi + \beta_{GS}\sin\psi) + \sin\beta_p \\ 0 & 1 & 0 \\ \cos\beta_p(\beta_{GC}\cos\psi + \beta_{GS}\sin\psi) - \sin\beta_p & 0 & \cos\beta_p + \sin\beta_p(\beta_{GC}\cos\psi + \beta_{GS}\sin\psi) \end{bmatrix}$$

With the couplings included, (i.e. $\theta = \theta - k_{p\beta}\beta - k_{p\zeta}\zeta + k_{p\beta G}(\beta_{GC}\cos\psi + \beta_{GS}\sin\psi)$)

these matrices change as shown below:

$$T_{cu} = \begin{bmatrix} 1 & 0 & 0 \\ 0 & (1 + T_{cu}^1)\cos\theta_0 + T_{cu}^2\sin\theta_0 & -T_{cu}^2\cos\theta_0 + (1 + T_{cu}^1)\sin\theta_0 \\ 0 & T_{cu}^2\cos\theta_0 - (1 + T_{cu}^1)\sin\theta_0 & (1 + T_{cu}^1)\cos\theta_0 + T_{cu}^2\sin\theta_0 \end{bmatrix}$$

where

$$\begin{aligned} T_{cu}^1 &= -k_{p\beta}\,\beta\,k_{p\zeta}\,\zeta + (k_{p\beta}\,\beta + k_{p\zeta}\,\zeta)(k_{p\beta G}\,\beta_{GC}\,\cos\psi + k_{p\beta G}\,\beta_{GS}\,\sin\psi) \\ T_{cu}^2 &= k_{p\beta}\,\beta + k_{p\zeta}\,\zeta - k_{p\beta G}\,\beta_{GC}\,\cos\psi - k_{p\beta G}\,\beta_{GS}\,\sin\psi \\ &\quad + k_{p\beta}\,\beta\,k_{p\zeta}\,\zeta\,(k_{p\beta G}\,\beta_{GC}\,\cos\psi + k_{p\beta G}\,\beta_{GS}\,\sin\psi) \end{aligned}$$

$$[T_{dc}] = \begin{bmatrix} 1 - \frac{1}{2}w_b'^2 - \frac{1}{2}v_b'^2 & \begin{array}{l} w_b'\sin\theta_0 \\ +v_b'\cos\theta_0 \\ +T_{dc}^{12}\end{array} & \begin{array}{l} -v_b'\sin\theta_0 \\ +w_b'\cos\theta_0 \\ +T_{dc}^{13}\end{array} \\ \begin{array}{l}(-w_b'\cos\phi + v_b'\sin\phi)\sin\theta_0 \\ -(v_b'\cos\phi + w_b'\sin\phi)\cos\theta_0 \\ +T_{dc}^{21}\end{array} & \cos\phi & \sin\phi \\ \begin{array}{l}(v_b'\cos\phi + w_b'\sin\phi)\sin\theta_0 \\ +(-w_b'\cos\phi + v_b'\sin\phi)\cos\theta_0 \\ +T_{dc}^{31}\end{array} & -\sin\phi & \cos\phi \end{bmatrix}$$

$$T_{dc}^{12} = \left[\begin{array}{c} (-k_{p\beta} + k_{p\beta G} - k_{p\beta}k_{p\zeta}k_{p\beta G} - k_{p\zeta})\,w_b' \\ +\begin{pmatrix} 3k_{p\zeta}k_{p\beta G} - k_{p\beta}^2 - k_{p\beta G}^2 - k_{p\zeta}^2 - 3k_{p\beta}k_{p\zeta} + 3k_{p\beta}k_{p\beta G} \\ -k_{p\beta}^2k_{p\zeta}^2k_{p\beta G}^2 + 2k_{p\beta}k_{p\zeta}k_{p\beta G}^2 - 2k_{p\beta}^2k_{p\zeta}k_{p\beta G} - 2k_{p\beta}k_{p\zeta}^2k_{p\beta G} \end{pmatrix} v_b' \end{array} \right] \cos\theta_0$$

$$
+\left[\begin{array}{c}
\left(k_{p\zeta}k_{p\beta G}+k_{p\beta}k_{p\beta G}-k_{p\beta}k_{p\zeta}\right)w_b' \\
+\left(\begin{array}{c}
-k_{p\beta G}+k_{p\beta}^2k_{p\zeta}k_{p\beta G}^2+k_{p\zeta}^2k_{p\beta G}+k_{p\zeta}-k_{p\beta}^2k_{p\zeta} \\
-k_{p\zeta}^2k_{p\beta}+k_{p\beta}+4k_{p\beta}k_{p\zeta}k_{p\beta G}-k_{p\zeta}k_{p\beta G}^2 \\
-k_{p\beta G}^2k_{p\beta}-k_{p\beta}^2k_{p\zeta}^2k_{p\beta G}+k_{p\beta}k_{p\zeta}^2k_{p\beta G}^2+k_{p\beta}^2k_{p\beta G}
\end{array}\right)v_b'
\end{array}\right]\sin\theta_0
$$

$$
\begin{aligned}
T_{dc}^{13} = {} & \left[\begin{array}{c}
\left(\begin{array}{c}
3k_{p\zeta}k_{p\beta G}-k_{p\beta}^2-k_{p\beta G}^2-k_{p\zeta}^2-3k_{p\beta}k_{p\zeta}+3k_{p\beta}k_{p\beta G} \\
-k_{p\beta}^2k_{p\zeta}^2k_{p\beta G}^2+2k_{p\beta}k_{p\zeta}k_{p\beta G}^2-2k_{p\beta}^2k_{p\zeta}k_{p\beta G}-2k_{p\beta}k_{p\zeta}^2k_{p\beta G}
\end{array}\right)w_b' \\
+\left(k_{p\zeta}+k_{p\beta}+k_{p\beta}k_{p\zeta}k_{p\beta G}-k_{p\beta G}\right)v_b'
\end{array}\right]\cos\theta_0 \\
& +\left[\begin{array}{c}
\left(\begin{array}{c}
-k_{p\beta G}+k_{p\beta}^2k_{p\zeta}k_{p\beta G}^2+k_{p\zeta}^2k_{p\beta G}+k_{p\zeta}-k_{p\beta}^2k_{p\zeta} \\
-k_{p\zeta}^2k_{p\beta}+k_{p\beta}+4k_{p\beta}k_{p\zeta}k_{p\beta G}-k_{p\zeta}k_{p\beta G}^2 \\
-k_{p\beta G}^2k_{p\beta}-k_{p\beta}^2k_{p\zeta}^2k_{p\beta G}+k_{p\beta}k_{p\zeta}^2k_{p\beta G}^2+k_{p\beta}^2k_{p\beta G}
\end{array}\right)w_b' \\
+\left(k_{p\beta}k_{p\zeta}-k_{p\beta}k_{p\beta G}-k_{p\zeta}k_{p\beta G}\right)v_b'
\end{array}\right]\sin\theta_0
\end{aligned}
$$

$$
\begin{aligned}
T_{dc}^{21} = {} & \left[\begin{array}{c}
\left(k_{p\zeta}-k_{p\beta G}+k_{p\beta}+k_{p\beta}k_{p\zeta}k_{p\beta G}\right)w_b' \\
+\left(\begin{array}{c}
k_{p\beta G}^2+k_{p\beta}^2+2k_{p\beta}k_{p\zeta}^2k_{p\beta G}+3k_{p\beta}k_{p\zeta}-3k_{p\zeta}k_{p\beta G}-2k_{p\beta}k_{p\zeta}k_{p\beta G}^2 \\
+2k_{p\beta}^2k_{p\zeta}k_{p\beta G}+k_{p\beta}^2k_{p\zeta}^2k_{p\beta G}^2-3k_{p\beta}k_{p\beta G}+k_{p\zeta}^2
\end{array}\right)v_b'
\end{array}\right]\cos\theta_0\cos\phi \\
& +\left[\begin{array}{c}
\left(k_{p\beta}k_{p\zeta}-k_{p\beta}k_{p\beta G}-k_{p\zeta}k_{p\beta G}\right)w_b' \\
+\left(\begin{array}{c}
-4k_{p\beta}k_{p\zeta}k_{p\beta G}+k_{p\beta G}^2k_{p\zeta}-k_{p\beta}k_{p\zeta}^2k_{p\beta G}^2+k_{p\beta}^2k_{p\zeta}^2k_{p\beta G} \\
+k_{p\beta G}^2k_{p\beta}-k_{p\beta}^2k_{p\zeta}k_{p\beta G}^2-k_{p\beta}^2k_{p\beta G}+k_{p\beta}^2k_{p\zeta}+k_{p\zeta}^2k_{p\beta} \\
-k_{p\zeta}^2k_{p\beta G}-k_{p\beta}+k_{p\beta G}-k_{p\zeta}
\end{array}\right)v_b'
\end{array}\right]\sin\theta_0\cos\phi \\
& +\left[\begin{array}{c}
\left(\begin{array}{c}
k_{p\beta G}^2+k_{p\beta}^2+2k_{p\beta}k_{p\zeta}^2k_{p\beta G}+3k_{p\beta}k_{p\zeta}-3k_{p\zeta}k_{p\beta G}-2k_{p\beta}k_{p\zeta}k_{p\beta G}^2 \\
+2k_{p\beta}^2k_{p\zeta}k_{p\beta G}+k_{p\beta}^2k_{p\zeta}^2k_{p\beta G}^2-3k_{p\beta}k_{p\beta G}+k_{p\zeta}^2
\end{array}\right)w_b' \\
+\left(-k_{p\beta}+k_{p\beta G}-k_{p\beta}k_{p\zeta}k_{p\beta G}-k_{p\zeta}\right)v_b'
\end{array}\right]\cos\theta_0\sin\phi \\
& +\left[\begin{array}{c}
\left(\begin{array}{c}
-4k_{p\beta}k_{p\zeta}k_{p\beta G}+k_{p\beta G}^2k_{p\zeta}-k_{p\beta}k_{p\zeta}^2k_{p\beta G}^2+k_{p\beta}^2k_{p\zeta}^2k_{p\beta G}+k_{p\beta G}^2k_{p\beta} \\
-k_{p\beta}^2k_{p\zeta}k_{p\beta G}^2-k_{p\beta}^2k_{p\beta G}+k_{p\beta}^2k_{p\zeta}+k_{p\zeta}^2k_{p\beta}-k_{p\zeta}^2k_{p\beta G} \\
-k_{p\beta}+k_{p\beta G}-k_{p\zeta}
\end{array}\right)w_b' \\
+\left(k_{p\zeta}k_{p\beta G}+k_{p\beta}k_{p\beta G}-k_{p\beta}k_{p\zeta}\right)v_b'
\end{array}\right]\sin\theta_0\sin\phi
\end{aligned}
$$

$$
\begin{aligned}
T_{dc}^{31} = {} & \left[\begin{array}{c}
\left(\begin{array}{c}
k_{p\beta G}^2+k_{p\beta}^2+2k_{p\beta}k_{p\zeta}^2k_{p\beta G}+3k_{p\beta}k_{p\zeta}-3k_{p\zeta}k_{p\beta G}-2k_{p\beta}k_{p\zeta}k_{p\beta G}^2 \\
+2k_{p\beta}^2k_{p\zeta}k_{p\beta G}+k_{p\beta}^2k_{p\zeta}^2k_{p\beta G}^2-3k_{p\beta}k_{p\beta G}+k_{p\zeta}^2
\end{array}\right)w_b' \\
+\left(-k_{p\beta}+k_{p\beta G}-k_{p\beta}k_{p\zeta}k_{p\beta G}-k_{p\zeta}\right)v_b'
\end{array}\right]\cos\theta_0\cos\phi \\
& +\left[\begin{array}{c}
\left(\begin{array}{c}
-4k_{p\beta}k_{p\zeta}k_{p\beta G}+k_{p\beta G}^2k_{p\zeta}-k_{p\beta}k_{p\zeta}^2k_{p\beta G}^2+k_{p\beta}^2k_{p\zeta}^2k_{p\beta G} \\
+k_{p\beta G}^2k_{p\beta}-k_{p\beta}^2k_{p\zeta}k_{p\beta G}^2-k_{p\beta}^2k_{p\beta G}+k_{p\beta}^2k_{p\zeta}+k_{p\zeta}^2k_{p\beta} \\
-k_{p\zeta}^2k_{p\beta G}-k_{p\beta}+k_{p\beta G}-k_{p\zeta}
\end{array}\right)w_b' \\
+\left(k_{p\zeta}k_{p\beta G}+k_{p\beta}k_{p\beta G}-k_{p\beta}k_{p\zeta}\right)v_b'
\end{array}\right]\sin\theta_0\cos\phi \\
& +\left[\begin{array}{c}
\left(-k_{p\beta}+k_{p\beta G}-k_{p\beta}k_{p\zeta}k_{p\beta G}-k_{p\zeta}\right)w_b' \\
+\left(\begin{array}{c}
-3k_{p\beta}k_{p\zeta}-k_{p\zeta}^2-k_{p\beta}^2k_{p\zeta}^2k_{p\beta G}^2-2k_{p\beta}k_{p\zeta}^2k_{p\beta G}-2k_{p\beta}^2k_{p\zeta}k_{p\beta G} \\
+2k_{p\beta}k_{p\zeta}k_{p\beta G}^2-k_{p\beta G}^2-k_{p\beta}^2+3k_{p\beta}k_{p\beta G}+3k_{p\zeta}k_{p\beta G}
\end{array}\right)v_b'
\end{array}\right]\cos\theta_0\sin\phi \\
& +\left[\begin{array}{c}
\left(k_{p\zeta}k_{p\beta G}+k_{p\beta}k_{p\beta G}-k_{p\beta}k_{p\zeta}\right)w_b' \\
+\left(\begin{array}{c}
k_{p\beta}-k_{p\beta}^2k_{p\zeta}+4k_{p\beta}k_{p\zeta}k_{p\beta G}+k_{p\zeta}+k_{p\zeta}^2k_{p\beta G} \\
-k_{p\beta G}^2k_{p\beta}+k_{p\beta}^2k_{p\zeta}k_{p\beta G}^2-k_{p\zeta}^2k_{p\beta}+k_{p\beta}^2k_{p\beta G}-k_{p\beta G}^2k_{p\zeta} \\
+k_{p\beta}k_{p\zeta}^2k_{p\beta G}^2-k_{p\beta}^2k_{p\zeta}^2k_{p\beta G}-k_{p\beta G}
\end{array}\right)v_b'
\end{array}\right]\sin\theta_0\sin\phi
\end{aligned}
$$

8.5 Rigid Blade Simplification

The following substitutions are made:

$$u_e = \phi = 0$$

$$v_b = -\sin\zeta\,(x-e_l)$$

$$w_b = \sin\beta\,(x-e_f)$$

Therefore, the following derivatives with respect to time and length out the blade are also zero:

$$\dot{u}_e \quad \ddot{u}_e \quad \dot{\phi} \quad \ddot{\phi} \quad \phi^{'} \quad \dot{\phi}^{'} \quad \ddot{\phi}^{'}$$

The non-zero derivatives are:

$$\dot{v}_b = -\dot{\zeta}\cos\zeta\,(x-e_l) \qquad \dot{w}_b = \dot{\beta}\,(x-e_f)\cos\beta$$

$$\ddot{v}_b = \dot{\zeta}^2\,(x-e_f)\sin\zeta - \ddot{\zeta}\,(x-e_l)\cos\zeta \qquad \ddot{w}_b = -\dot{\beta}^2\,(x-e_f)\sin\beta + \ddot{\beta}\,(x-e_f)\cos\beta$$

$$v_b^{'} = -\sin\zeta \qquad w_b^{'} = \sin\beta$$

$$\dot{v}_b^{'} = -\dot{\zeta}\cos\zeta \qquad \dot{w}_b^{'} = \dot{\beta}\cos\beta$$

$$\ddot{v}_b^{'} = \dot{\zeta}^2\sin\zeta - \ddot{\zeta}\cos\zeta \qquad \ddot{w}_b^{'} = -\dot{\beta}^2\sin\beta + \ddot{\beta}\cos\beta$$

The cross-sectional integrals arising from the foreshortening terms in the kinetic energy are simplified as follows:

$$\iint_A v_b^{'}v_b^{'}\,d\eta\,d\zeta = x\sin^2\zeta \qquad \iint_A w_b^{'}w_b^{'}\,d\eta\,d\zeta = x\sin^2\beta$$

$$\iint_A v_b^{'}\dot{v}_b^{'}\,d\eta\,d\zeta = x\dot{\zeta}\sin\zeta\cos\zeta \qquad \iint_A w_b^{'}\dot{w}_b^{'}\,d\eta\,d\zeta = x\dot{\beta}\sin\beta\cos\beta$$

$$\iint_A \dot{v}_b^{'}\dot{v}_b^{'}\,d\eta\,d\zeta = x\dot{\zeta}^2\cos^2\zeta \qquad \iint_A \dot{w}_b^{'}\dot{w}_b^{'}\,d\eta\,d\zeta = x\dot{\beta}^2\cos^2\beta$$

$$\iint_A v_b^{'}\ddot{v}_b^{'}\,d\eta\,d\zeta = \sin\zeta\left(\ddot{\zeta}\cos\zeta - \dot{\zeta}^2\sin\zeta\right) \qquad \iint_A w_b^{'}\ddot{w}_b^{'}\,d\eta\,d\zeta = \sin\beta\left(\ddot{\beta}\cos\beta - \dot{\beta}^2\sin\beta\right)$$

It is important to note that all differentiation is completed before any small angle assumptions are made. Once these substitutions are made, though, β and ζ are assumed to be small so that

$$
\begin{array}{ll}
v_b = -\zeta\,(x - e_l) & w_b = \beta\,(x - e_f) \\
\dot{v}_b = -\dot{\zeta}\,(x - e_l) & \dot{w}_b = \dot{\beta}\,(x - e_f) \\
\ddot{v}_b = \dot{\zeta}^2\,(x - e_f)\,\zeta - \ddot{\zeta}\,(x - e_l) & \ddot{w}_b = -\dot{\beta}^2\,(x - e_f)\,\beta + \ddot{\beta}\,(x - e_f) \\
v_b' = -\zeta & w_b' = \beta \\
\dot{v}_b' = -\dot{\zeta} & \dot{w}_b' = \dot{\beta} \\
\ddot{v}_b' = \dot{\zeta}^2\zeta - \ddot{\zeta} & \ddot{w}_b' = -\dot{\beta}^2\beta + \ddot{\beta} \\
\iint_A v_b' v_b'\, d\eta\, d\zeta = x\zeta^2 & \iint_A w_b' w_b'\, d\eta\, d\zeta = x\beta^2 \\
\iint_A v_b' \dot{v}_b'\, d\eta\, d\zeta = x\dot{\zeta}\zeta & \iint_A w_b' \dot{w}_b'\, d\eta\, d\zeta = x\dot{\beta}\beta \\
\iint_A \dot{v}_b' \dot{v}_b'\, d\eta\, d\zeta = x\dot{\zeta}^2 & \iint_A \dot{w}_b' \dot{w}_b'\, d\eta\, d\zeta = x\dot{\beta}^2 \\
\iint_A v_b' \ddot{v}_b'\, d\eta\, d\zeta = \zeta\left(\ddot{\zeta} - \dot{\zeta}^2\zeta\right) & \iint_A w_b' \ddot{w}_b'\, d\eta\, d\zeta = \beta\left(\ddot{\beta} - \dot{\beta}^2\beta\right)
\end{array}
$$

8.6 Wing Element Matrices

From the kinetic energy formulation for the wing, a structural mass matrix is calculated.

$$[M^S] = \begin{bmatrix} M^S_{11} & M^S_{12} \\ M^S_{21} & M^S_{22} \end{bmatrix}$$

$$[M^S_{11}] = \begin{bmatrix} \frac{\rho AL}{3} & 0 & 0 & 0 & 0 & 0 \\ 0 & \frac{13\rho AL}{35} & \frac{11\rho AL^2}{210} & 0 & 0 & 0 \\ 0 & \frac{11\rho AL^2}{210} & \frac{\rho AL^3}{105} & 0 & 0 & 0 \\ 0 & 0 & 0 & \frac{13\rho AL}{35} & \frac{11\rho AL^2}{210} & \frac{7\rho ALy_{CM}}{20} \\ 0 & 0 & 0 & \frac{11\rho AL^2}{210} & \frac{\rho AL^3}{105} & \frac{\rho AL^2y_{CM}}{20} \\ 0 & 0 & 0 & \frac{7\rho ALy_{CM}}{20} & \frac{\rho AL^2y_{CM}}{20} & \frac{\rho I_pL}{3} \end{bmatrix}$$

$$[M^S_{12}] = \begin{bmatrix} \frac{\rho AL}{6} & 0 & 0 & 0 & 0 & 0 \\ 0 & \frac{9\rho AL}{70} & -\frac{13\rho AL^2}{420} & 0 & 0 & 0 \\ 0 & \frac{13\rho AL^2}{420} & -\frac{\rho AL^3}{140} & 0 & 0 & 0 \\ 0 & 0 & 0 & \frac{9\rho AL}{70} & -\frac{13\rho AL^2}{420} & \frac{3\rho ALy_{CM}}{20} \\ 0 & 0 & 0 & \frac{13\rho AL^2}{420} & -\frac{\rho AL^3}{140} & \frac{\rho AL^2y_{CM}}{30} \\ 0 & 0 & 0 & \frac{3\rho ALy_{CM}}{20} & -\frac{\rho AL^2y_{CM}}{30} & \frac{\rho I_pL}{6} \end{bmatrix}$$

$$[M^S_{21}] = \begin{bmatrix} \frac{\rho AL}{6} & 0 & 0 & 0 & 0 & 0 \\ 0 & \frac{9\rho AL}{70} & \frac{13\rho AL^2}{420} & 0 & 0 & 0 \\ 0 & -\frac{13\rho AL^2}{420} & -\frac{\rho AL^3}{140} & 0 & 0 & 0 \\ 0 & 0 & 0 & \frac{9\rho AL}{70} & \frac{13\rho AL^2}{420} & \frac{3\rho ALy_{CM}}{20} \\ 0 & 0 & 0 & -\frac{13\rho AL^2}{420} & -\frac{\rho AL^3}{140} & -\frac{\rho AL^2y_{CM}}{30} \\ 0 & 0 & 0 & \frac{3\rho ALy_{CM}}{20} & \frac{\rho AL^2y_{CM}}{30} & \frac{\rho I_pL}{6} \end{bmatrix}$$

$$[M^S_{22}] = \begin{bmatrix} \frac{\rho AL}{3} & 0 & 0 & 0 & 0 & 0 \\ 0 & \frac{13\rho AL}{35} & -\frac{11\rho AL^2}{210} & 0 & 0 & 0 \\ 0 & -\frac{11\rho AL^2}{210} & \frac{\rho AL^3}{105} & 0 & 0 & 0 \\ 0 & 0 & 0 & \frac{13\rho AL}{35} & -\frac{11\rho AL^2}{210} & \frac{7\rho ALy_{CM}}{20} \\ 0 & 0 & 0 & -\frac{11\rho AL^2}{210} & \frac{\rho AL^3}{105} & -\frac{\rho AL^2y_{CM}}{20} \\ 0 & 0 & 0 & \frac{7\rho ALy_{CM}}{20} & -\frac{\rho AL^2y_{CM}}{20} & \frac{\rho I_pL}{3} \end{bmatrix}$$

The strain energy formulation gives the structural stiffness matrix.

$$[K^S] = \begin{bmatrix} K^S_{11} & K^S_{12} \\ K^S_{21} & K^S_{22} \end{bmatrix}$$

$$[K^S_{11}] = \begin{bmatrix} \frac{EA}{L} & 0 & 0 & 0 & 0 & 0 \\ 0 & 12\frac{EI_z}{L^3} & 6\frac{EI_z}{L^2} & 0 & 0 & 0 \\ 0 & 6\frac{EI_z}{L^2} & 4\frac{EI_z}{L} & 0 & 0 & 0 \\ 0 & 0 & 0 & 12\frac{EI_y}{L^3} & 6\frac{EI_y}{L^2} & 0 \\ 0 & 0 & 0 & 6\frac{EI_y}{L^2} & 4\frac{EI_y}{L} & 0 \\ 0 & 0 & 0 & 0 & 0 & \frac{GJ}{L} \end{bmatrix}$$

$$[K_{12}^S] = \begin{bmatrix} -\frac{EA}{L} & 0 & 0 & 0 & 0 & 0 \\ 0 & -12\frac{EI_z}{L^3} & 6\frac{EI_z}{L^2} & 0 & 0 & 0 \\ 0 & -6\frac{EI_z}{L^2} & 2\frac{EI_z}{L} & 0 & 0 & 0 \\ 0 & 0 & 0 & -12\frac{EI_y}{L^3} & 6\frac{EI_y}{L^2} & 0 \\ 0 & 0 & 0 & -6\frac{EI_y}{L^2} & 2\frac{EI_y}{L} & 0 \\ 0 & 0 & 0 & 0 & 0 & -\frac{GJ}{L} \end{bmatrix}$$

$$[K_{21}^S] = \begin{bmatrix} -\frac{EA}{L} & 0 & 0 & 0 & 0 & 0 \\ 0 & -12\frac{EI_z}{L^3} & -6\frac{EI_z}{L^2} & 0 & 0 & 0 \\ 0 & 6\frac{EI_z}{L^2} & 2\frac{EI_z}{L} & 0 & 0 & 0 \\ 0 & 0 & 0 & -12\frac{EI_y}{L^3} & -6\frac{EI_y}{L^2} & 0 \\ 0 & 0 & 0 & 6\frac{EI_y}{L^2} & 2\frac{EI_y}{L} & 0 \\ 0 & 0 & 0 & 0 & 0 & -\frac{GJ}{L} \end{bmatrix}$$

$$[K_{22}^S] = \begin{bmatrix} \frac{EA}{L} & 0 & 0 & 0 & 0 & 0 \\ 0 & 12\frac{EI_z}{L^3} & -6\frac{EI_z}{L^2} & 0 & 0 & 0 \\ 0 & -6\frac{EI_z}{L^2} & 4\frac{EI_z}{L} & 0 & 0 & 0 \\ 0 & 0 & 0 & 12\frac{EI_y}{L^3} & -6\frac{EI_y}{L^2} & 0 \\ 0 & 0 & 0 & -6\frac{EI_y}{L^2} & 4\frac{EI_y}{L} & 0 \\ 0 & 0 & 0 & 0 & 0 & \frac{GJ}{L} \end{bmatrix}$$

The couplings in the wing are added into the stiffness matrix.

$$[K^C] = \begin{bmatrix} 0 & 0 & 0 & 0 & 0 & 0 & 0 & 0 & 0 & 0 & 0 & 0 \\ 0 & 0 & 0 & 0 & 0 & 0 & 0 & 0 & 0 & 0 & 0 & 0 \\ 0 & 0 & 0 & 0 & 0 & K_{46}\frac{1}{L} & 0 & 0 & 0 & 0 & 0 & -K_{46}\frac{1}{L} \\ 0 & 0 & 0 & 0 & 0 & 0 & 0 & 0 & 0 & 0 & 0 & 0 \\ 0 & 0 & 0 & 0 & 0 & K_{45}\frac{1}{L} & 0 & 0 & 0 & 0 & 0 & -K_{45}\frac{1}{L} \\ 0 & 0 & K_{46}\frac{1}{L} & 0 & K_{45}\frac{1}{L} & 0 & 0 & 0 & -K_{46}\frac{1}{L} & 0 & -K_{45}\frac{1}{L} & 0 \\ 0 & 0 & 0 & 0 & 0 & 0 & 0 & 0 & 0 & 0 & 0 & 0 \\ 0 & 0 & 0 & 0 & 0 & 0 & 0 & 0 & 0 & 0 & 0 & 0 \\ 0 & 0 & 0 & 0 & 0 & -K_{46}\frac{1}{L} & 0 & 0 & 0 & 0 & 0 & K_{46}\frac{1}{L} \\ 0 & 0 & 0 & 0 & 0 & 0 & 0 & 0 & 0 & 0 & 0 & 0 \\ 0 & 0 & 0 & 0 & 0 & -K_{45}\frac{1}{L} & 0 & 0 & 0 & 0 & 0 & K_{45}\frac{1}{L} \\ 0 & 0 & -K_{46}\frac{1}{L} & 0 & -K_{45}\frac{1}{L} & 0 & 0 & 0 & K_{46}\frac{1}{L} & 0 & K_{45}\frac{1}{L} & 0 \end{bmatrix}$$

The work energy from the aerodynamics gives the motion-independent forcing vector and the motion-dependent stiffness and damping matrices.

$$\{F^A\} = \frac{1}{2}\rho V^2 c c_{l_\alpha} \left\{ \begin{array}{c} 0 \\ 0 \\ 0 \\ \frac{1}{2}\alpha_0 L \\ \frac{1}{12}\alpha_0 L^2 \\ \frac{1}{2}e\alpha_0 L \\ 0 \\ 0 \\ 0 \\ \frac{1}{2}\alpha_0 L \\ -\frac{1}{12}\alpha_0 L^2 \\ \frac{1}{2}e\alpha_0 L \end{array} \right\}$$

$$[K^A] = \frac{1}{2}\rho V^2 c c_{l_\alpha} \left[\begin{array}{cc} K_{11}^A & K_{12}^A \\ K_{21}^A & K_{22}^A \end{array} \right]$$

$$[K_{11}^A] = \left[\begin{array}{cccccc} 0 & 0 & 0 & 0 & 0 & 0 \\ 0 & 0 & 0 & 0 & 0 & 0 \\ 0 & 0 & 0 & 0 & 0 & 0 \\ 0 & 0 & 0 & \frac{1}{2}\sin\Lambda & -\frac{1}{10}\sin\Lambda L & \frac{7}{20}\cos\Lambda L \\ 0 & 0 & 0 & \frac{1}{10}\sin\Lambda L & 0 & \frac{1}{20}\cos\Lambda L^2 \\ 0 & 0 & 0 & \frac{1}{2}\sin\Lambda e & -\frac{1}{12}\sin\Lambda L e & \frac{1}{3}e\cos\Lambda L \end{array} \right]$$

$$[K_{12}^A] = \left[\begin{array}{cccccc} 0 & 0 & 0 & 0 & 0 & 0 \\ 0 & 0 & 0 & 0 & 0 & 0 \\ 0 & 0 & 0 & 0 & 0 & 0 \\ 0 & 0 & 0 & -\frac{1}{2}\sin\Lambda & \frac{1}{10}\sin\Lambda L & \frac{3}{20}\cos\Lambda L \\ 0 & 0 & 0 & -\frac{1}{10}\sin\Lambda L & \frac{1}{60}\sin\Lambda L^2 & \frac{1}{30}\cos\Lambda L^2 \\ 0 & 0 & 0 & -\frac{1}{2}\sin\Lambda e & \frac{1}{12}\sin\Lambda L e & \frac{1}{6}e\cos\Lambda L \end{array} \right]$$

$$[K_{21}^A] = \left[\begin{array}{cccccc} 0 & 0 & 0 & 0 & 0 & 0 \\ 0 & 0 & 0 & 0 & 0 & 0 \\ 0 & 0 & 0 & 0 & 0 & 0 \\ 0 & 0 & 0 & \frac{1}{2}\sin\Lambda & \frac{1}{10}\sin\Lambda L & \frac{3}{20}\cos\Lambda L \\ 0 & 0 & 0 & -\frac{1}{10}\sin\Lambda L & -\frac{1}{60}\sin\Lambda L^2 & -\frac{1}{30}\cos\Lambda L^2 \\ 0 & 0 & 0 & \frac{1}{2}\sin\Lambda e & \frac{1}{12}\sin\Lambda L e & \frac{1}{6}e\cos\Lambda L \end{array} \right]$$

$$[K_{22}^A] = \left[\begin{array}{cccccc} 0 & 0 & 0 & 0 & 0 & 0 \\ 0 & 0 & 0 & 0 & 0 & 0 \\ 0 & 0 & 0 & 0 & 0 & 0 \\ 0 & 0 & 0 & -\frac{1}{2}\sin\Lambda & -\frac{1}{10}\sin\Lambda L & \frac{7}{20}\cos\Lambda L \\ 0 & 0 & 0 & \frac{1}{10}\sin\Lambda L & 0 & -\frac{1}{20}\cos\Lambda L^2 \\ 0 & 0 & 0 & -\frac{1}{2}\sin\Lambda e & -\frac{1}{12}\sin\Lambda L e & \frac{1}{3}e\cos\Lambda L \end{array} \right]$$

$$[C^A] = \frac{1}{2}\rho V^2 c c_{l_\alpha} \begin{bmatrix} 0 & 0 & 0 & 0 & 0 & 0 & 0 & 0 & 0 & 0 & 0 & 0 \\ 0 & 0 & 0 & 0 & 0 & 0 & 0 & 0 & 0 & 0 & 0 & 0 \\ 0 & 0 & 0 & 0 & 0 & 0 & 0 & 0 & 0 & 0 & 0 & 0 \\ 0 & 0 & 0 & -\frac{13}{35}\frac{L}{V} & -\frac{11}{210}\frac{L^2}{V} & 0 & 0 & 0 & 0 & -\frac{9}{70}\frac{L}{V} & \frac{13}{420}\frac{L^2}{V} & 0 \\ 0 & 0 & 0 & -\frac{11}{210}\frac{L^2}{V} & -\frac{1}{105}\frac{L^3}{V} & 0 & 0 & 0 & 0 & -\frac{13}{420}\frac{L^2}{V} & \frac{1}{140}\frac{L^3}{V} & 0 \\ 0 & 0 & 0 & -\frac{7}{20}\frac{eL}{V} & -\frac{1}{20}\frac{eL^2}{V} & 0 & 0 & 0 & 0 & -\frac{3}{20}\frac{eL}{V} & \frac{1}{30}\frac{eL^2}{V} & 0 \\ 0 & 0 & 0 & 0 & 0 & 0 & 0 & 0 & 0 & 0 & 0 & 0 \\ 0 & 0 & 0 & 0 & 0 & 0 & 0 & 0 & 0 & 0 & 0 & 0 \\ 0 & 0 & 0 & 0 & 0 & 0 & 0 & 0 & 0 & 0 & 0 & 0 \\ 0 & 0 & 0 & -\frac{9}{70}\frac{L}{V} & -\frac{13}{420}\frac{L^2}{V} & 0 & 0 & 0 & 0 & -\frac{13}{35}\frac{L}{V} & \frac{11}{210}\frac{L^2}{V} & 0 \\ 0 & 0 & 0 & \frac{13}{420}\frac{L^2}{V} & \frac{1}{140}\frac{L^3}{V} & 0 & 0 & 0 & 0 & \frac{11}{210}\frac{L^2}{V} & -\frac{1}{105}\frac{L^3}{V} & 0 \\ 0 & 0 & 0 & -\frac{3}{20}\frac{eL}{V} & -\frac{1}{30}\frac{eL^2}{V} & 0 & 0 & 0 & 0 & -\frac{7}{20}\frac{eL}{V} & \frac{1}{20}\frac{eL^2}{V} & 0 \end{bmatrix}$$

8.7 Assembly of Wing and Pylon

The $[M]$, $[C]$, and $[K]$ from the coupled rotor hub equations of motion are transformed into the fixed frame using a Fourier Coordinate Transformation. Tis transformation takes the degree of freedom vector

$$\lfloor \; \beta_0 \;\; \beta_{1c} \;\; \beta_{1s} \;\; \cdots \;\; \zeta_0 \;\; \zeta_{1c} \;\; \zeta_{1s} \;\; \cdots \;\; x_F \;\; y_F \;\; z_F \;\; \alpha_s \;\; \phi_s \;\; \psi_s \;\; \beta_{GC} \;\; \beta_{GS} \; \rfloor$$

and returns a new degree of freedom vector of

$$\lfloor \; \beta_0 \;\; \beta_{1c} \;\; \beta_{1s} \;\; \cdots \;\; \zeta_0 \;\; \zeta_{1c} \;\; \zeta_{1s} \;\; \cdots \;\; u \;\; v_{N+1} \;\; v'_{N+1} \;\; w_{N+1} \;\; w'_{N+1} \;\; \phi_{N+2} \;\; \beta_{GC} \;\; \beta_{GS} \; \rfloor$$

Then these matrices are constrained to remove the u degree of freedom. Note that this is only true when modeling a wing rigid in extension. This constraint will also be removed when fuselage motion is included. After this constraint, these matrices can be added into the wing tip degrees of freedom.

$$\lfloor \; \beta_0 \;\; \beta_{1c} \;\; \beta_{1s} \;\; \cdots \;\; \zeta_0 \;\; \zeta_{1c} \;\; \zeta_{1s} \;\; \cdots \;\; v_{N+1} \;\; v'_{N+1} \;\; w_{N+1} \;\; w'_{N+1} \;\; \phi_{N+2} \;\; \beta_{GC} \;\; \beta_{GS} \; \rfloor$$

Note that the ϕ degree of freedom used here is ϕ_{N+2} or the twist on the pylon side of the downstop spring. The wing tip will be ϕ, the twist on the wing side of the downstop spring.

$$[M_{wing}] = [T_{pre}]\,[M_{FCT}]\,[T_{post}]$$

$$[T_{pre}] = \begin{bmatrix} \begin{bmatrix} 1 & 0 & \dots & 0 \\ 0 & 1 & \dots & 0 \\ \vdots & \vdots & \ddots & \vdots \\ 0 & 0 & \dots & 1 \end{bmatrix}_{2N_b \times 2N_b} & \begin{bmatrix} 0 & 0 & \dots & 0 \\ 0 & 0 & \dots & 0 \\ \vdots & \vdots & \ddots & \vdots \\ 0 & 0 & \dots & 0 \end{bmatrix}_{2N_b \times 6} & \begin{bmatrix} 0 & 0 \\ 0 & 0 \\ \vdots & \vdots \\ 0 & 0 \end{bmatrix}_{2N_b \times 2} \\ \begin{bmatrix} 0 & 0 & \dots & 0 \\ 0 & 0 & \dots & 0 \\ \vdots & \vdots & \ddots & \vdots \\ 0 & 0 & \dots & 0 \end{bmatrix}_{6 \times 2N_b} & \begin{bmatrix} 0 & 1 & 0 & 0 & 0 & 0 \\ 1 & 0 & 0 & 0 & 0 & 0 \\ 0 & 0 & 0 & 0 & 0 & -1 \\ 0 & 0 & 1 & 0 & 0 & 0 \\ 0 & 0 & 0 & 0 & -1 & 0 \\ 0 & 0 & 0 & -1 & 0 & 0 \end{bmatrix} & \begin{bmatrix} 0 & 0 \\ 0 & 0 \\ \vdots & \vdots \\ 0 & 0 \end{bmatrix}_{6 \times 2} \\ \begin{bmatrix} 0 & 0 & \dots & 0 \\ 0 & 0 & \dots & 0 \end{bmatrix}_{2 \times 2N_b} & \begin{bmatrix} 0 & 0 & \dots & 0 \\ 0 & 0 & \dots & 0 \end{bmatrix}_{2 \times 6} & \begin{bmatrix} 1 & 0 \\ 0 & 1 \end{bmatrix} \end{bmatrix}$$

$$[T_{post}] = \begin{bmatrix} \begin{bmatrix} 1 & 0 & \dots & 0 \\ 0 & 1 & \dots & 0 \\ \vdots & \vdots & \ddots & \vdots \\ 0 & 0 & \dots & 1 \end{bmatrix}_{2N_b \times 2N_b} & \begin{bmatrix} 0 & 0 & \dots & 0 \\ 0 & 0 & \dots & 0 \\ \vdots & \vdots & \ddots & \vdots \\ 0 & 0 & \dots & 0 \end{bmatrix}_{2N_b \times 6} & \begin{bmatrix} 0 & 0 \\ 0 & 0 \\ \vdots & \vdots \\ 0 & 0 \end{bmatrix}_{2N_b \times 2} \\ \begin{bmatrix} 0 & 0 & \dots & 0 \\ 0 & 0 & \dots & 0 \\ \vdots & \vdots & \ddots & \vdots \\ 0 & 0 & \dots & 0 \end{bmatrix}_{6 \times 2N_b} & T5 & \begin{bmatrix} 0 & 0 \\ 0 & 0 \\ \vdots & \vdots \\ 0 & 0 \end{bmatrix}_{6 \times 2} \\ \begin{bmatrix} 0 & 0 & \dots & 0 \\ 0 & 0 & \dots & 0 \end{bmatrix}_{2 \times 2N_b} & \begin{bmatrix} 0 & 0 & \dots & 0 \\ 0 & 0 & \dots & 0 \end{bmatrix}_{2 \times 6} & \begin{bmatrix} 1 & 0 \\ 0 & 1 \end{bmatrix} \end{bmatrix}$$

$$T5 = \begin{bmatrix} 1 & 0 & 0 & 0 & 0 & 0 \\ 0 & 1 & 0 & 0 & 0 & 0 \\ 0 & 0 & 1 & 0 & 0 & 0 \\ 0 & 0 & 0 & 0 & -1 & 0 \\ 0 & 0 & 0 & -1 & 0 & 0 \\ 0 & 0 & 0 & 0 & 0 & 1 \end{bmatrix} \begin{bmatrix} 1 & 0 & 0 & 0 & 0 & 0 \\ 0 & 1 & 0 & 0 & 0 & 0 \\ 0 & 0 & 1 & 0 & 0 & 0 \\ 0 & 0 & 0 & 0 & z_{OFF} & -y_{OFF} \\ 0 & 0 & 0 & -z_{OFF} & 0 & x_{OFF} \\ 0 & 0 & 0 & y_{OFF} & -x_{OFF} & 0 \end{bmatrix}$$

$$\cdot \begin{bmatrix} \cos\Lambda & \sin\Lambda & 0 & 0 & 0 & 0 \\ -\sin\Lambda & \cos\Lambda & 0 & 0 & 0 & 0 \\ 0 & 0 & 1 & 0 & 0 & 0 \\ 0 & 0 & 0 & \cos\Lambda & \sin\Lambda & 0 \\ 0 & 0 & 0 & -\sin\Lambda & \cos\Lambda & 0 \\ 0 & 0 & 0 & 0 & 0 & 1 \end{bmatrix} \begin{bmatrix} 0 & 1 & 0 & 0 & 0 & 0 \\ 1 & 0 & 0 & 0 & 0 & 0 \\ 0 & 0 & 0 & 1 & 0 & 0 \\ 0 & 0 & 0 & 0 & 1 & 0 \\ 0 & 0 & 0 & 0 & 0 & 1 \\ 0 & 0 & -1 & 0 & 0 & 0 \end{bmatrix}$$

$$z_{OFF} = (h + z_{pcg})\cos\alpha_p - (x_{CG} + x_{pcg})\sin\alpha_p$$

$$y_{OFF} = y_{CG} + y_{pcg}$$

$$x_{OFF} = (h + z_{pcg})\sin\alpha_p + (x_{CG} + x_{pcg})\cos\alpha_p$$

The degrees of freedom from the rotor / hub equations of motion include hub motion already written in the inertial frame, i.e. after the shaft tilt due to pylon rotation. However, the pylon rotation must also be taken into account for the pylon masses and inertias. Beyond this difference, the pylon inertias are also centered at the pylon center of gravity rather than at the hub. This gives different values for the offsets as shown below.

$$[M_{pylon}] = [T_{pre}] \begin{bmatrix} m_{Fx} & 0 & 0 & 0 & 0 & 0 \\ 0 & m_{Fy} & 0 & 0 & 0 & 0 \\ 0 & 0 & m_{Fz} & 0 & 0 & 0 \\ 0 & 0 & 0 & I_{\phi_s} & 0 & 0 \\ 0 & 0 & 0 & 0 & I_{\alpha_s} & 0 \\ 0 & 0 & 0 & 0 & 0 & I_{\psi_s} \end{bmatrix} [T_{post}]$$

$$
[T_{pre}] = \begin{bmatrix} 0 & 1 & 0 & 0 & 0 & 0 \\ 1 & 0 & 0 & 0 & 0 & 0 \\ 0 & 0 & 0 & 0 & 0 & -1 \\ 0 & 0 & 1 & 0 & 0 & 0 \\ 0 & 0 & 0 & 1 & 0 & 0 \\ 0 & 0 & 0 & 0 & 1 & 0 \end{bmatrix} \begin{bmatrix} \cos\alpha_p & 0 & \sin\alpha_p & 0 & 0 & 0 \\ 0 & 1 & 0 & 0 & 0 & 0 \\ -\sin\alpha_p & 0 & \cos\alpha_p & 0 & 0 & 0 \\ 0 & 0 & 0 & \cos\alpha_p & 0 & \sin\alpha_p \\ 0 & 0 & 0 & 0 & 1 & 0 \\ 0 & 0 & 0 & -\sin\alpha_p & 0 & \cos\alpha_p \end{bmatrix}
$$

$$
[T_{post}] = \begin{bmatrix} \cos\alpha_p & 0 & -\sin\alpha_p & 0 & 0 & 0 \\ 0 & 1 & 0 & 0 & 0 & 0 \\ \sin\alpha_p & 0 & \cos\alpha_p & 0 & 0 & 0 \\ 0 & 0 & 0 & \cos\alpha_p & 0 & -\sin\alpha_p \\ 0 & 0 & 0 & 0 & 1 & 0 \\ 0 & 0 & 0 & \sin\alpha_p & 0 & \cos\alpha_p \end{bmatrix} \begin{bmatrix} 1 & 0 & 0 & 0 & 0 & 0 \\ 0 & 1 & 0 & 0 & 0 & 0 \\ 0 & 0 & 1 & 0 & 0 & 0 \\ 0 & 0 & 0 & 0 & z_{OFF} & -y_{OFF} \\ 0 & 0 & 0 & -z_{OFF} & 0 & x_{OFF} \\ 0 & 0 & 0 & y_{OFF} & -x_{OFF} & 0 \end{bmatrix}
$$

$$
\cdot \begin{bmatrix} \cos\Lambda & \sin\Lambda & 0 & 0 & 0 & 0 \\ -\sin\Lambda & \cos\Lambda & 0 & 0 & 0 & 0 \\ 0 & 0 & 1 & 0 & 0 & 0 \\ 0 & 0 & 0 & \cos\Lambda & \sin\Lambda & 0 \\ 0 & 0 & 0 & -\sin\Lambda & \cos\Lambda & 0 \\ 0 & 0 & 0 & 0 & 0 & 1 \end{bmatrix} \begin{bmatrix} 0 & 1 & 0 & 0 & 0 & 0 \\ 1 & 0 & 0 & 0 & 0 & 0 \\ 0 & 0 & 0 & 1 & 0 & 0 \\ 0 & 0 & 0 & 0 & 1 & 0 \\ 0 & 0 & 0 & 0 & 0 & 1 \\ 0 & 0 & -1 & 0 & 0 & 0 \end{bmatrix}
$$

$$
z_{OFF} = z_{pcg}\cos\alpha_p - x_{pcg}\sin\alpha_p
$$

$$
y_{OFF} = y_{pcg}
$$

$$
x_{OFF} = z_{pcg}\sin\alpha_p + x_{pcg}\cos\alpha_p
$$

NASA Graduate Student Researchers Program (GSRP)

FINAL ADMINISTRATIVE REPORT

(1) Name: Anna K.T. Howard (Grant Number: **NGT**-1-52109)

(2) Proposal Start Date: July 1, 1995
Degree to be awarded: Ph.D., Aerospace Engineering
Estimated Date of Graduation: December, 2000

(3) Title of Research Project: Aeromechanical Analysis for Tiltrotors with Elastically Tailored Soft-Inplane Composite Rotor Systems

(4) NASA Research Advisor's Name: Mark W. Nixon

(5) List Professional/Programmatic Travel During Fellowship

Event	Location	Date
NASA GSRP Orientation	NASA Langley	August, 1995
NASA Wind Tunnel Test	NASA Langley	December, 1995
AHS Annual Forum	Washington, DC	May, 1996
AHS Annual Forum	Virginia Beach, VA	May, 1997
ARO Workshop	St. Louis, MO	October, 1997
NASA Wind Tunnel Test	NASA Langley	August, 1998

(6) Seminars or Lectures Delivered at Universities and/or Institutes:
AHS Lichten Competition, Philadelphia, PA

(7) Meetings Attended by Specific Invitation: N/A

(8) Teaching Experience During GSRP Fellowship: N/A

(9) Summary of Research: see attached

(10) Publications and Papers Resulting from Research as a GSRP Fellow: N/A

(11) Patents Applied for as a Result of Research as a GSRP Fellow: N/A

(12) Current Forwarding Address: 825 Ashworth Lane, Boalsburg, PA 16827

(13) Appraisal of the GSRP: The GSRP is a wonderful program for graduate students. The personal contact with a NASA researcher is quite invaluable. The experiences I have had at NASA have greatly inclined me to seek employment at one of the centers. I know of no other fellowship program which offers more opportunities to its participants.

Student Signature: Anna K. T. Howard Date: 6/30/99

Faculty Advisor Signature: Edward C. Smith Date: 7/28/99